



Thèse présentée pour obtenir le grade de

DOCTEUR DE L'ÉCOLE POLYTECHNIQUE

Spécialité : Mécanique

par

María Luisa CORDERO

Contrôle optique de gouttes microfluidiques

Thèse soutenue le 15 décembre 2009 devant le jury composé de :

M. Charles BAROUD	Directeur de thèse
M. Axel BUGUIN	Rapporteur
Mme. Annie COLIN	Rapporteuse
Mme. Elise LORENCEAU	Examinatrice
M. Patrick TABELING	Président du jury

Laboratoire d'Hydrodynamique
Ecole Polytechnique, 91128 Palaiseau, France

Remerciements

Je commence par exprimer ma plus profonde gratitude envers mon directeur de thèse, Charles, qui m'a guidé pendant ces trois années. J'ai beaucoup apprécié sa créativité, son enthousiasme et son énergie. Je le remercie spécialement pour la confiance qu'il a eu en moi pour chaque projet, ce qui m'a fait sentir capable de réaliser cette thèse. En plus, j'admire et apprécie sa qualité humaine et pour cela je l'ai en grand estime. Merci beaucoup Charles ! J'espère sincèrement qu'on se retrouvera dans le monde scientifique et aussi dans un cadre personnel.

Mes remerciements vont aussi vers les gens que j'ai rencontrés au LadHyX (c'est une longue liste ici). Merci, d'abord, mes "frères" et "soeurs" thésards : Elena qui a été une loyale camarade, Claire ma bonne amie, Cristobal qui m'a fait sentir comme chez nous. Merci aussi à Rémi V., Jon, Gianluca, Alexandre, Matthieu, Rémi D., Miguel, Fred, Diego, Shehryar, Yu, Grégory, Yong Yun et Christoph. L'expérience de rencontrer des gens aussi variés m'a énormément enrichie. Je vous souhaite la meilleure chance pour le futur. Je remercie aussi Eletta pour sa son amitié, sa gaieté, ses conseils et sa compagnie, et Sabine pour sa générosité de partager avec moi son expérience de vie en tant que femme chercheuse. François pour sa capacité de transformer tout sujet de recherche en une aventure passionnante, avec la bonne humeur qui le caractérise. Michaël en qui j'ai trouvé un très belle personne. Emilie, pour m'avoir tant aidé pendant la première année. Finalement merci aux autres intégrants permanents du LadHyX pour faire de ce laboratoire un endroit où les bonnes idées se développent dans une atmosphère accueillante.

Pendant ma thèse je me suis rendue plusieurs fois en Ecosse, et je voudrais remercier pour cela les gens qui m'y ont accueilli et qui ont travaillé avec moi : I thank David, Daniel and Hans for their hospitality, help and patience. It has been an excellent experience to work with them. Je remercie également les gens qui m'ont aidé à développer certaines manips de ma thèse, notamment Jean-Luc Reverchon et Cédric Bouzigues.

Je voudrais aussi remercier les membres du jury, Patrick Tabeling, Axel Buguin, Annie Collin, Elise Lorenceau et Christophe Josserand pour avoir accepté d'évaluer cette thèse et pour avoir, avec leur propre travail, inspiré plusieurs fois mon imagination scientifique. Je remercie spécialement Elise de m'avoir gentiment aidé à développer la manip des jets.

Mon séjour en France a été possible grâce au financement apporté par la Fondation EADS et plus modestement par le gouvernement du Chili. Je tiens à les remercier pour cela, et tout spécialement Mme Certiat, qui a été ma parraine de la Fondation EADS.

Je voudrais remercier mes amis chiliens qui ont vécu au même temps que moi cette expérience et qui m'ont apporté leur aide, compagnie et amitié.

Finalement, ma plus grande reconnaissance est dirigée aux membres de ma famille, qui ont

toujours encouragé ma liberté et partagé mon sens de l'aventure. Ils ont participé à ma joie et à mon émerveillement et m'ont soutenu dans les moments les plus sombres. Parmi eux, je remercie spécialement mon Guillermo, qui, même à plus de dix mille kilomètres de distance, sait toujours être mon plus grand soutien. Gracias Guillermito por tu paciencia y cariño, por tu apoyo incondicional y tu confianza, en fin...gracias por todo.

Contents

1	Introduction	1
1.1	An introduction to microfluidics	1
1.1.1	Microchannels	3
1.1.2	The challenges of microfluidics	5
1.1.3	Droplet-based microfluidics	7
1.2	Flows at the micron scale	15
1.2.1	Reynolds number	16
1.2.2	Peclet number	18
1.2.3	Capillary number	19
1.3	The objective of this thesis	25
1.3.1	State of the art in microfluidic manipulation	25
1.3.2	Outline of the thesis	27
2	Temperature rise due to laser absorption	29
2.1	Introduction	29
2.2	Experimental setup	30
2.2.1	Fluorophore solutions	32
2.2.2	Thermophoresis correction	33
2.3	Theory	34
2.4	Results	37
2.4.1	Dynamics of the temperature increase	37
2.4.2	Steady state	39
2.4.3	Numerical simulations	41
2.5	Discussion	42

3	Origin and magnitude of the Marangoni force	45
3.1	Introduction	45
3.2	Experimental setup	46
3.3	Role of the surfactant	50
3.3.1	Surface tension at equilibrium	50
3.3.2	Spatial surfactant redistribution	52
3.4	Hydrodynamics and force balance	54
3.4.1	Steady state force	54
3.4.2	Transients before coming to a complete halt	56
3.5	Discussion	58
3.5.1	Two limitations	58
3.5.2	Role of the confinement	59
3.5.3	Marangoni stresses and interface velocity	60
3.6	Summary	61
4	Manipulation with holographic techniques	63
4.1	Introduction	63
4.2	Experimental setup	64
4.3	Results	65
4.3.1	Spatial laser patterns	65
4.3.2	Applications	67
4.4	Conclusions	69
5	Mixing via thermocapillary flow	71
5.1	Introduction	71
5.2	Experimental Setups	73
5.3	Temporal and spatial characteristic dimensions	75
5.3.1	Spatial scales	75
5.3.2	Time scales	76
5.4	Flow Fields	77
5.5	Mixing	79
5.5.1	Mixing measurements	79
5.5.2	Mixing efficiency extracted from PIV measurements	81
5.5.3	Mixing of dye	82
5.6	Discussion	85

5.6.1	Heating of the drop contents	86
6	Formation of drops by laser forcing	89
6.1	Introduction	89
6.2	Spatiotemporal stability theory of a fluid jet	90
6.3	Experimental setup	93
6.4	Laser forcing	94
6.5	Experimental results	96
6.5.1	Unperturbed state	96
6.5.2	Perturbed state	98
6.6	Discussion	101
7	Conclusions	105

Chapter 1

Introduction

1.1 An introduction to microfluidics

Since always, nature has been able to exploit the features of fluid flow through structures whose size ranges on the scale of microns to achieve transport of material. Carriage of nutrients, cells and oxygen within blood capillaries and air breathing through the lung airflows, are only few examples. The presence of micron sized structures in nature which contain and conduct fluid flow has major consequences for life. For example, feeding mechanisms for tall trees against gravity are possible thanks to the flow created inside their long narrow cells. These cells, filled with a liquid medium called cytosol that carries nutrients, may reach several centimeters in length but are only few microns in thickness. Their inner surface is covered by thin filaments and microtubules which move to induce fluid flow in their vicinity. Thanks to the nature of the flows at small scales, this fluid flow near the cell surface drags the whole bulk of cytosol thus creating a recirculation flow that allows for the transport of nutrients [Pickard, 2003; van de Meent *et al.*, 2008].

In science, fluid at the micron scale has been object of an increasing attention since the late 1980s. From this moment, inspired in the development of the semiconductor technology which allowed the creation of integrated circuits, microfluidics was born holding the promise of miniaturizing and automating the work in biological and chemical laboratories. One aim of microfluidics is to implement all the stages of a chemical or biological test inside a single, small, portable, reproducible and cheap device. Such a device would resemble very much a sensor from the point of view of the user, but it would be in fact an ensemble of channels of microscopic dimensions where reagents and catalyzers are mixed, incubated and products are separated and detected. Such a device, integrating all the steps of a laboratory test in a single chip is usually

referred as Lab-On-a-Chip (LOC), or micro-Total-Analysis-System (μ TAS).

Imagine for example that one wants to study the chemical reaction



where A and B are chemical reagents and C is the product of their reaction. Traditionally, to study such reaction one would make solutions containing A and B in fixed concentrations, bring them together in a beaker, mix them by means of a magnetic agitator and a rotatory magnet and analyze the products in some way or another. Making a rough estimation one would need at least a few milliliters of each solution to perform the reaction.

In the LOC approach, instead, one would study the same reaction in a device similar to the one schematically represented in Fig. 1.1. This device consists of a manifold of small channels with sections specially designed to carry out the reaction (1.1) and detect the product C . The overall dimensions of the device would be small enough as to be lifted with your fingers and it would be able to contain a volume of fluid of the order of a fraction of a microliter.

The working mechanism of the LOC device would be essentially the following: Solutions of A and B would be injected through inlet_A and inlet_B respectively and flow down the channels. After meeting, both solutions would be allowed to mix in the mixing chamber for a given time and then the mixed fluid would be sent to the section of the channel where the presence of C is detected.

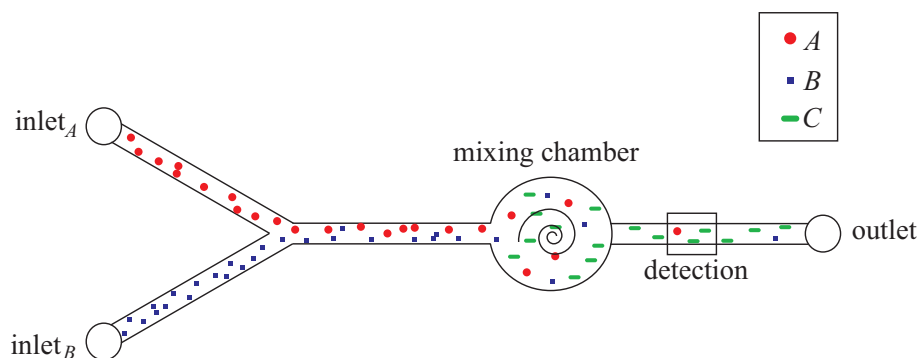


Figure 1.1: Schematic of a LOC device.

The traditional method can be improved by the used of micropipettes and microarrays, which allow the reduction of the used material, but anyway the LOC approach uses much less material and equipment. Now, if we require to study a large number of variations of the reaction (1.1), for example the effect of varying the relative concentrations of A and B , the temperature or pH, in the traditional method one would have to repeat the process the necessary number of times,

with the associated consumption of material and time. The LOC approach instead would use a modified device, for example the one shown in Fig. 1.2, which replicates the mixing chamber to inject a catalyst in different concentrations. In this way, using a single chip, one would be able to perform a large set of experiments, using essentially the same amount of time a single experiment would require and with little material waste.

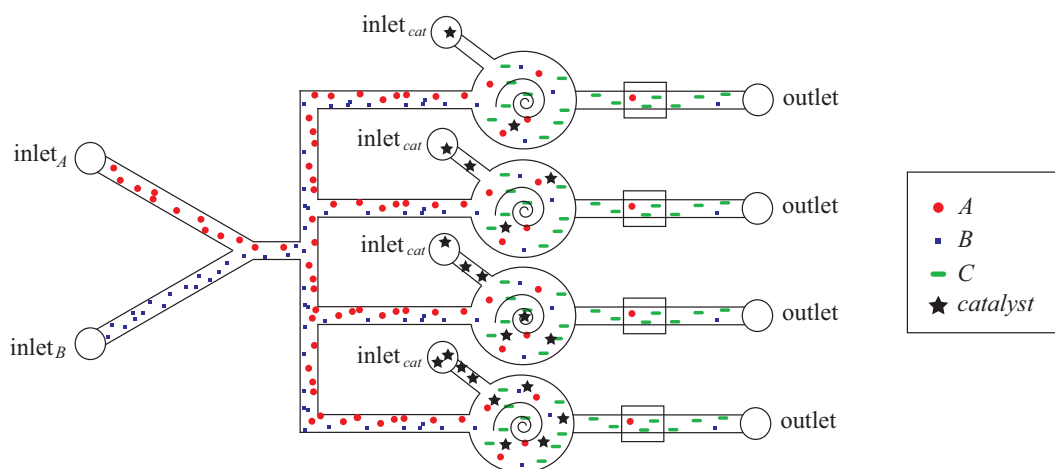


Figure 1.2: Schematic of a LOC device.

Reduction of material and time is what makes microfluidics so interesting for fields such as chemistry and biology. To have an idea of the large number of experiments that are involved in the research of these fields, consider genetics. The human genome contains about 20 thousand genes. Each gene has specific functions, usually related to synthesis of proteins, and most of them remain unknown. The study of such a huge library of genes requires a lot of work and it is not likely to advance rapidly if the analytical process is not automated and parallelized. The development of microfluidics offers the required automation and parallelization for this kind of process. In fact, genetics and protein analysis are very active fields that have boosted the research in microfluidics.

1.1.1 Microchannels

One of the first LOC prototypes reported in the literature was developed by Harrison in 1992 [Harrison *et al.*, 1992]. This device consisted of a network of channels micromachined in a glass substrate which was covered by another glass plate that sealed the channels. A mixture of fluorophores was injected through holes drilled on one of the glass plates and driven by means of electric fields through a long straight channel. Because of the different electric properties of the

fluorescent molecules, they flowed through the channel at different speeds and therefore they separated into two distinctive plugs. The goal of the device was to detect the fluorescence peaks associated with both fluorophores as they flowed through the channel.

The device measured $14.8 \text{ cm} \times 3.9 \text{ cm} \times 1 \text{ cm}$. Its fabrication was expensive and complicated because it required special and time consuming methods for carving the channels in the glass and bonding the glass surfaces. In fact, it was constructed using the methods already available from microelectronics which were based on the glass and silicon technology. Since then, the materials for fabricating microchannels have evolved, leaving glass and silicon aside to embrace polymeric materials. Relative to glass and silicon, polymers have several advantages: they are cheaper, flexible and moldable and they can be sealed easily, both reversibly through Van der Waals forces and irreversibly through chemical bonds.

In the late 1990s decade, a number of papers from the group of Whitesides [for a review see Xia & Whitesides, 1998; McDonald *et al.*, 2000] revolutionized the field of microfluidics by introducing a new method for microfabrication called soft lithography. This method, based on the patterning of polymeric materials allows the construction and replication of microstructures in a cheap and fast way, without the need of a white room. The basic steps of soft lithography are:

1. **Creation of a mask.** In this step the geometry of the microchannel is conceived with the aid of a computer software and printed with high resolution on a transparency to obtain a photomask.
2. **Construction of a mold.** A resistant mold is created by lithography. The lithographic procedure is schematically shown in Fig. 1.3: First a thin layer of a photosensitive material (a “photoresist”) is deposited onto the substrate. Then, the layer is patterned by selectively exposing it to a radiation source with the aid of the photomask. Finally, the surface is etched, that is, corroded by chemicals or ions to dissolve the unexposed portions of the photoresist and expose the pattern. The resulting structures are strong, durable and precise and are to be used as a mold for the microchannels.
3. **Replication.** The mold obtained in the previous step, which contains the microchannel geometry in relief, is used to cast a polymer called poly(dimethylsiloxane) (PDMS) which is deposited onto the mold in a liquid state and allowed to cure for some time. Once cured, the PDMS is peeled off the mold and sealed against a substrate to form in this way the channels between the substrate and the polymer block. Access into the channels to inject

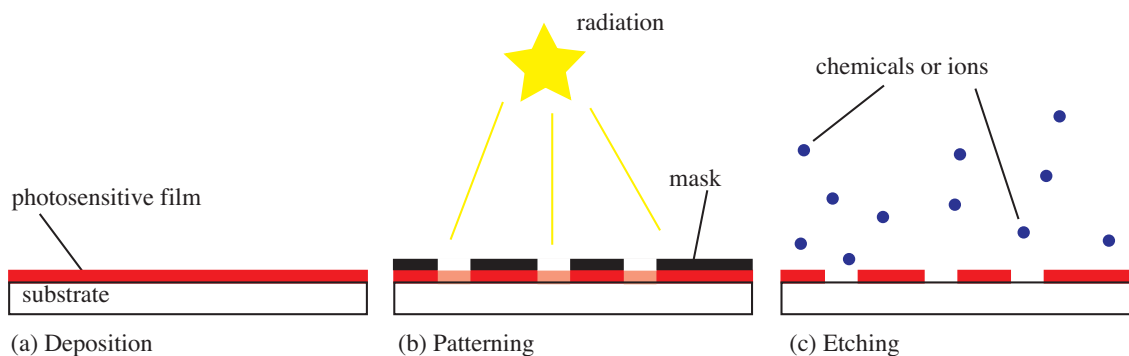


Figure 1.3: Sketch of the lithographic process: (a) Deposition of the photosensitive layer. (b) Exposition of the photosensitive layer to radiation to pattern the layer. (c) Etching of the layer to expose the pattern.

and recover the fluids is provided by holes punched in the PDMS before sealing it to the substrate.

This method is particularly suited for LOC applications, since, once the mold has been created, it allows for the rapid fabrication of a large number of identical microchannels. The idea of having reproducible devices is therefore accomplished at this stage. Moreover, soft lithography has proven to be useful for a wide range of applications, including the patterning of surfaces for manipulating their hydrophobicity and achieving superhydrophobic surfaces [Bartolo *et al.*, 2006; Cortese *et al.*, 2008] and the creation of culture chambers for the study of cell behaviour [Poujade *et al.*, 2007].

A top view of a particular microchannel fabricated with soft lithography is shown in Fig. 1.4(a). The block of PDMS has the channels carved in its surface and it is sealed against a glass substrate. Channels are $50\ \mu\text{m}$ in depth, between 250 and $500\ \mu\text{m}$ in width and some millimeters long. Holes have been punched in the PDMS block to allow fluid to enter and leave the channels; the fluid is injected through tubes connecting the fluid reservoirs and the channel inlets and recovered in the outlet through another tube. An image of the same channel is shown in Fig. 1.4(b), where the glass substrate and the tubes can be observed.

1.1.2 The challenges of microfluidics

Miniaturization of the laboratory processes aims to reducing waste, costs and time. Microfluidics responds to the need of miniaturizing the work in laboratories by the construction of devices that correspond to the reduced equivalent of a laboratory set of equipment to carry out analyses. To do that, microfluidics needs to deal with two fundamental tasks: the shrinking of the laboratory

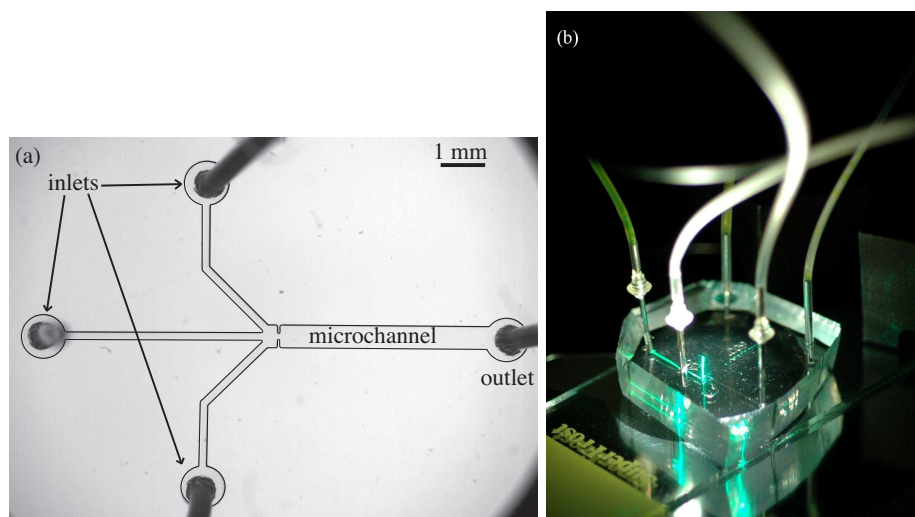


Figure 1.4: (a) Image of a microchannel in PDMS. Tubes are plunged in the inlets and in the outlet, allowing for the fluid to be injected and recovered. (b) Image of a microchannel. The glass substrate and the tubes for fluid injection and collection can be observed.

processes and their integration in a single chip. The correct implementation of these points is fundamental for the success of LOC, but miniaturization and integration are not necessarily straightforward.

Concerning miniaturization, challenges rapidly arrive because the physical mechanisms involved in the analytical processes do not necessarily scale down favorably. For example, the hydrodynamics of small volumes of fluids is ruled by viscosity, which imposes problems for mixing the species of an analysis. Another example is the problem of detection. When decreasing the volume of fluid the number of molecules available is also reduced, so detection becomes a highly challenging problem. As a third problem, fluids easily penetrate all spaces of the microchannels, both due to capillarity and fluid flow. This, along with diffusion, complicates the correct manipulation of material dissolved in the fluids: Microchannels, although constituting a convenient platform for microfluidics, lack the necessary compartmentalization to avoid the dispersion of the species.

Integration is not less problematic, mainly because feedback mechanisms are inherently present in the channel networks, so special care must be taken in the design of the LOC devices for each component to function properly. For example, pressure drops in one portion of a microchannel affect the behaviour of the entire device. Again, dispersion must be reduced to avoid contamination between different stages of an analysis.

Dealing with these and other problems requires a deep understanding of the physical pro-

cesses present in microfluidics. In this sense, microfluidics constitutes a platform to perform fundamental research, since it brings out physical phenomena that do not usually appear at macroscopic scales. For microfluidics applications, fundamental research has focused on understanding and predicting the behaviour of microfluidic systems. This is specially necessary for extracting scaling laws that are valid in a high number of cases. One example is the study of the non linear dynamics of fluid interfaces present when immiscible fluids are injected in the microchannels, which is of particular interest to describe the transport of drops and bubbles in microchannels.

Together with this fundamental research, microfluidics efforts are often directed to the development of new approaches to face the different steps of an analysis. In this sense, a large number of microfluidic components have been developed to carry out specific laboratory functions in a manner completely different from the way they are done in bench-top experiments. These components must be able to properly work in the miniaturized environment, that is, overcoming the limitations imposed by the physics at the microscopic scale. For example, microfluidic components that mix the reagents of a reaction must be able to deal with viscosity dominated flows, detection methods must be optimized to detect low quantities of molecules and fluids must be manipulated properly to avoid their dispersion.

A particular approach to deal with the microfluidics problems is the introduction of drops. Though in principle microchannels constitute a reasonably good chamber to perform chemical and biological analyses, further encapsulation is often desirable. The integration of drops as a microfluidic component has given rise to droplet-based microfluidics (also called “digital” microfluidics), which constitutes the basic ground for this thesis work and that we discuss in the next section.

1.1.3 Droplet-based microfluidics

Drops are attractive components in microfluidics because they can encapsulate, transport and isolate reagents, cells or genes (or virtually any particle), keeping their contents uncontaminated. One of their most important characteristic is that they allow for accurate manipulation of discrete volumes of fluid through the manipulation of the drop as a whole. In fact, drops can be fused and their contents can be mixed to trigger a reaction and they can concentrate the products of a given reaction to facilitate detection. Figure 1.5 shows examples of these uses of drops: encapsulation [Fig. 1.5(a), [Luo *et al.*, 2007]], fusion [Fig. 1.5(b), [Tan *et al.*, 2004]], mixing [Fig. 1.5(c), [Song *et al.*, 2003]], and detection [Fig. 1.5(d), [Huebner *et al.*, 2007]]. In that sense, digital microfluidics bases the implementation of all the steps of an analysis on the manipulation of drops.

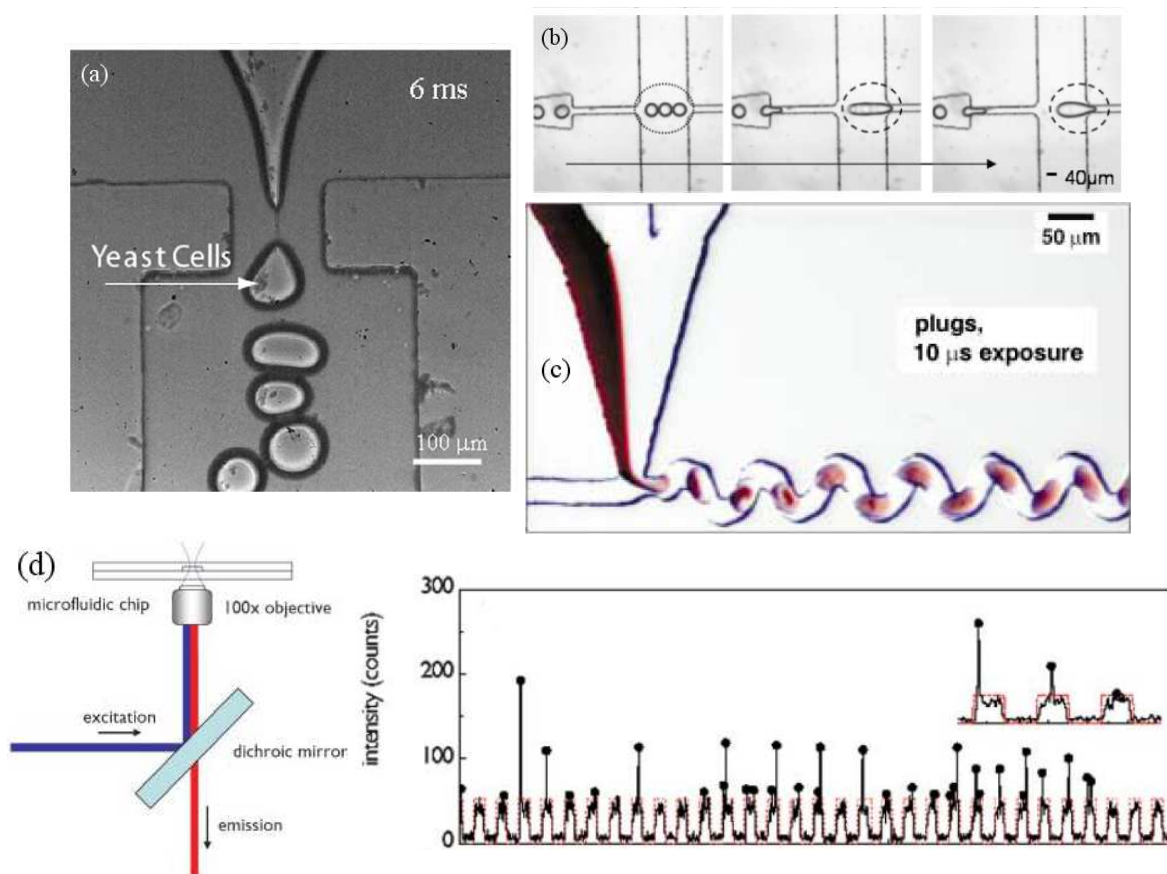


Figure 1.5: (a) Encapsulation of yeast cells in drops of agarose flowing in mineral oil inside a microchannel. Taken from [Luo *et al.*, 2007]. (b) Fusion of three drops inside a microchannel. The arrow indicates the direction of the flow. Taken from [Tan *et al.*, 2004]. (c) Mixing inside drops in a serpentine channel. Taken from [Song *et al.*, 2003]. (d) Detection of drops. When observed from a fluorescence microscope, each drop appears as a weak fluorescent peak. Larger fluorescent peaks are observed when a cell is contained in the drop. From [Huebner *et al.*, 2007].

Drops have another interesting feature that makes them particularly suited for parallel LOC applications and it is their character as isolated microchambers. In fact, each drop may be considered as an individual analysis chamber to contain a separate reaction and in this way they can be used to parallelize the work avoiding to increase the size and volume of the microchannel.

The success of digital microfluidics depends on the implementation of efficient drop operations for each analytical step. For this, the development of strategies for controlling drops is fundamental at each stage, from the drop formation, passing through the drop transport, to the final detection process. Now, we will briefly review three fundamental drop operations which are relevant for this thesis: drop formation, routing of drops and mixing.

Formation of drops

Drop formation is a process characterized by the fractioning of a stream of fluid (the “dispersed phase”) in an immiscible carrier fluid (the “continuous phase”). During the drop formation process the components of an analysis, dissolved in the dispersed phase, are encapsulated. Within drops, isolation is ensured by the utilization of a carrier fluid that completely wets the walls of the microchannel, thus creating a thin film between the walls and the drops and therefore completely surrounding the drops.

The success of droplet-based microfluidics depends on the ability to precisely produce highly monodisperse emulsions of controlled size. Although until now the mechanisms involved in the process of drop formation are obscure, it is known that it involves shear stresses, inertial drag, hydrostatic pressure and surface tension. The dominance of one or other of these forces defines different regimes of drop formation. Regimes dominated by viscous forces are characterized by unsteady and even chaotic drop formation [Garstecki *et al.*, 2005a]. On the contrary, when surface tension or inertia dominate, periodic and stable drop formation cycles are obtained. In these cases, the production of highly monodisperse emulsions has been proven in microfluidic devices, the dispersion in the drop radius ranging around 1% [Garstecki *et al.*, 2004] at frequencies varying from a few Hertz [Funfschilling *et al.*, 2009] to some kilo Hertz [Gañán-Calvo & Gordillo, 2001] and with controllable drop sizes [Garstecki *et al.*, 2006; Castro-Hernández *et al.*, 2009].

The most common microfluidic devices to produce drops, shown in Fig. 1.6, are the T-junction, flow focusing and co-flowing devices. Generally speaking, these devices are based on the separate injection of the dispersed and the continuous phase into a region of the microchannel where the dispersed phase breaks up due to the hydrodynamic forcing exerted by the carrier fluid.

In a T-junction, shown in Fig. 1.6(a), the carrier fluid flows through the main channel and the dispersed phase is injected perpendicularly, forming a T. Drop formation occurs by segmentation of the dispersed phase in the continuous phase. In flow focusing devices [Fig. 1.6(b)], instead, the continuous phase and the dispersed phase converge to a constriction zone where the flows are focused and where drop pinch-off occurs.

Drop formation in these two devices, when capillary forces largely dominate over inertial and viscous forces, is driven by a sequence of hydrodynamic mechanisms, namely (i) an increase of pressure due to the blockage of the continuous phase by the advancing column of dispersed phase, (ii) the subsequent squeezing and thinning of this column by the continuous phase and (iii) the final destabilization and breakup of the column when it becomes too thin [Garstecki *et al.*, 2005c]. In this regime, the reproducibility of the drop formation cycle, and therefore the

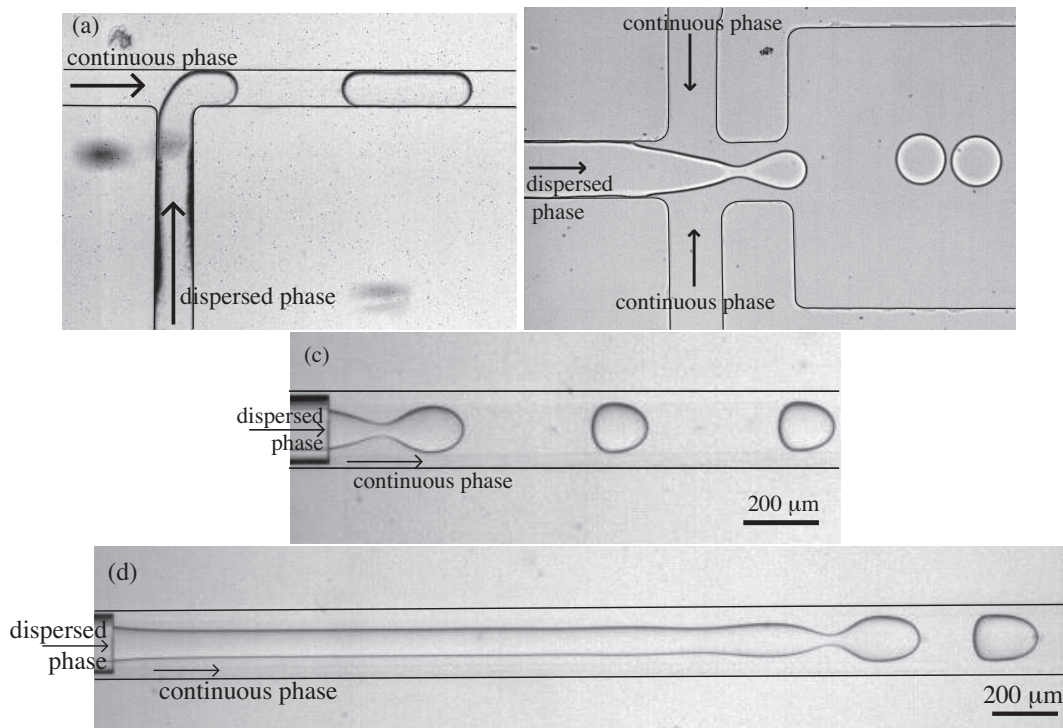


Figure 1.6: Different geometries used for drop formation: (a) T-junction, (b) flow focusing and (c, d) co-flowing. In coflowing devices, two regimes may exist: dripping (c) and jetting (d).

monodispersity of the drops, is ensured by the slow, quasistatic nature of most part of the process, from the blockage of the continuous phase until just before the column breakup. Instead, the pinch-off event is a singular, unstable and extremely fast process [Eggers, 1993]. Polydisperse emulsion, however, may be produced if capillarity no longer dominates over viscosity or inertia [Garstecki *et al.*, 2005a]

The mechanism of drop formation in co-flowing devices differs from the other two cases. In the co-flowing device, shown in Figs. 1.6(c) and (d), the dispersed fluid is injected inside the carrier fluid, both fluids flowing in the same direction. Here, depending on the surface tension, the densities, viscosities and velocities of both fluids, drop formation may occur right at the entrance of the dispersed phase, a regime called dripping [Fig. 1.6(c)], or further downstream, a phenomenon named jetting [Fig. 1.6(d)]. It is largely accepted that a Rayleigh-Plateau-like instability rules the mechanisms of drop formation in both cases and that the different regimes observed correspond to different hydrodynamic instabilities: while the dripping regime would correspond to an absolute instability of the column of dispersed phase, characterized by a steady, reproducible drop formation frequency and size, the jetting regime would be a result of a convective instability associated with an unsteady drop formation frequency and a higher dispersion in

the drop size [Huerre & Monkewitz, 1990; Guillot *et al.*, 2007; Gañán-Calvo, 2007; Utada *et al.*, 2007; Herrada *et al.*, 2008].

Routing of drops

In a complex channel network, where bifurcations, turns and intersections of channel branches occur, the trajectory of drops is a key point to be considered for the success of a droplet-based microfluidic device. Although the most obvious router existing in microfluidics are microchannels themselves, the trajectory of drops within the microchannels is not always obvious, due to the presence of bifurcations and interaction between drops and also due to the deformability and breakability of the drops.

Indeed, the flow of drops immersed in another fluid inside a channel is not a trivial problem and their trajectory is a complex function of the fluids viscosities, the surface tension, the presence of surfactant molecules, the drop size and the channel geometry. In the description of the transport of drops inside a microchannel, two regimes can be distinguished:

1. When the concentration of drops is low enough, a simple strategy to accurately predict the trajectory of drops inside a microchannel is to consider the flow of the carrier fluid in the absence of drops. This flow typically consists in a Poiseuille flow [Tabeling, 2003], characterized by a linear dependence of the flow rate Q in the pressure difference between the ends of the channel Δp :

$$\Delta p = QR_{\text{hyd}}, \quad (1.2)$$

where R_{hyd} represents the hydrodynamic resistance of the channel and describes its opposition to fluid flow. R_{hyd} is a function of the channel geometry and the fluid viscosity. In particular, the longer and narrower the channel and the more viscous the fluid, the harder it is for it to flow.

Considering the shear stress on the drop due to this flow, the movement of a drop in a bifurcation can be predicted, as explained by Tan *et al.* [Tan *et al.*, 2004]. As a general rule, the drop will move in the direction where the flow velocity is higher, as long as shear stresses are low enough to prevent the drop breakup.

2. When the number of drops in a microchannel is high, the effect of the drops in the flow drives interactions between them and therefore must be considered. At first order, the perturbation of the flow by the presence of a drop is accounted for by an extra hydrodynamic

resistance associated with the drop. In this sense, a drop is considered as a constriction when calculating the streamlines of the carrier fluid flow. The moving drop interface, therefore, is a source of nonlinearity which can lead to complex drop traffic due to interactions between drops, as shown experimentally by several authors [Engl *et al.*, 2005; Jousse *et al.*, 2006; Fuerstman *et al.*, 2007a; Prakash & Gershenfeld, 2007]. Despite the complexity of this problem, accurate predictions can be made for the drop trajectory in this work frame, given that drops remain unbroken and their position in the microchannel is a known initial condition [Schindler & Adjari, 2008].

The resistance associated with a drop is a complicated function of the fluids viscosities, the drop velocity and size, the channel geometry and the presence of surfactant. Besides the several phenomenological expressions that have been derived for the hydrodynamic resistance of drops and bubbles in different conditions [Fuerstman *et al.*, 2007b; Adzima & Velankar, 2006; Vanapalli *et al.*, 2009], the drop resistance can be measured, whether directly using pressure sensors [Adzima & Velankar, 2006] or by indirect methods that extract the hydrodynamic resistance of single drops from their interactions [Labrot *et al.*, 2009; Vanapalli *et al.*, 2009].

Careful considerations on the microchannel geometry and the features of the drops allow for a precise control of the drop trajectory using the descriptions mentioned above. This passive framework, that is when the trajectory of drops is controlled only by the flow of the external fluid and the hydrodynamic interactions between drops, allows for the implementation of the most important routing functions, for example the sorting of drops based on their size, as shown in Fig. 1.7(a) [Chabert & Viovy, 2008] or more complex functions such as the implementation of the basic logic operations AND, OR and NOT, as shown in Fig. 1.7(b) [Prakash & Gershenfeld, 2007].

Sometimes, however, it is useful to have an active control over the transport of drops, that is to apply external fields to modify the trajectory of drops. Although the utilization of an external field introduces complexity to the problem, it provides a way to enhance the control in microfluidics and to create extra functionality that cannot be achieved, or at least not easily, in the passive framework, for example the development of sampling protocols or the sorting based on the drop contents rather than the drop size.

Several strategies of drop routing have been developed based on the application of external fields. Examples are the utilization of electric fields [Fig. 1.8(a), [Ahn *et al.*, 2006b]], light [Fig. 1.8(d), [de Saint Vincent *et al.*, 2008]], or acoustic waves [Fig. 1.8(c), [Franke *et al.*, 2009]].

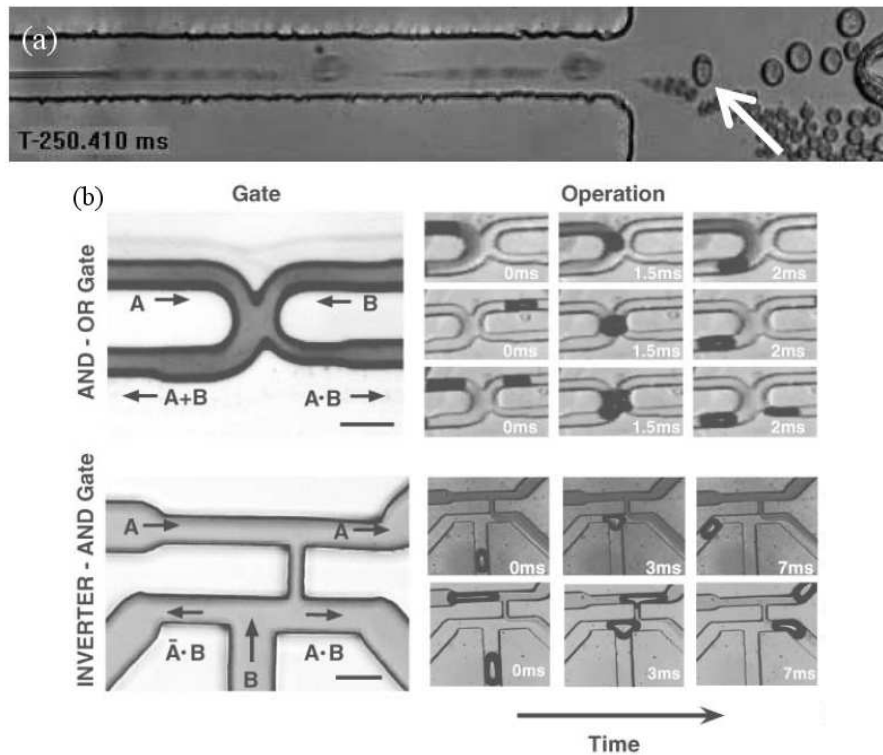


Figure 1.7: (a) Passive sorter. Drops containing a cell (as the one indicated by the arrow) are larger and are recovered in upper channel. From [Chabert & Viovy, 2008]. (b) Implementation of the logical operations AND (\cdot), OR ($+$) and NOT ($\bar{\cdot}$). From [Prakash & Gershenfeld, 2007].

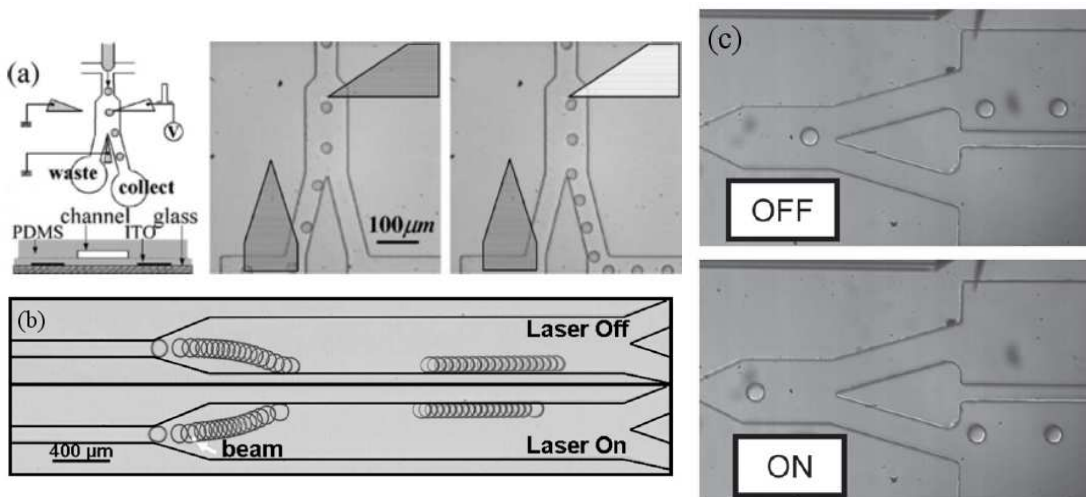


Figure 1.8: (a) Routing of drops using an electric field, generated with electrodes (represented by triangles). From [Ahn *et al.*, 2006b]. (b) Routing of drops using a laser beam. From [de Saint Vincent *et al.*, 2008]. (c) Routing of drops using a traveling acoustic wave in the direction perpendicular to the flow direction. From [Franke *et al.*, 2009].

Mixing

Mixing constitutes a fundamental function to be implemented in microfluidics, since many types of analysis require mixing of different components. However, the flows in microfluidics are dominated by viscosity and therefore turbulence, which rapidly and efficiently mixes the fluids at macroscopic scales, are absent in microfluidics. In fact, without the implementation of efficient stirring mechanisms, mixing in microfluidics is ruled by diffusion which is a process too slow for efficient LOC.

In viscosity dominated flows, efficient mixing relies in the creation of chaotic streamlines which, in complement with diffusion, homogenize thoroughly the fluid [Aref, 1984]. The principle of mixing through chaotic streamlines consists in the generation of thin stripes of the unmixed fluids, across which diffusion may take place to homogenize the sample. The repetitive thinning of these stripes enhances the homogenization of the fluid by reducing exponentially the distance, and therefore the time, for diffusion to take place. This principle is shown in Fig. 1.9, where the patterning of one of the channel walls induces a transversal flow that mixes two streams of fluid [Stroock *et al.*, 2002].

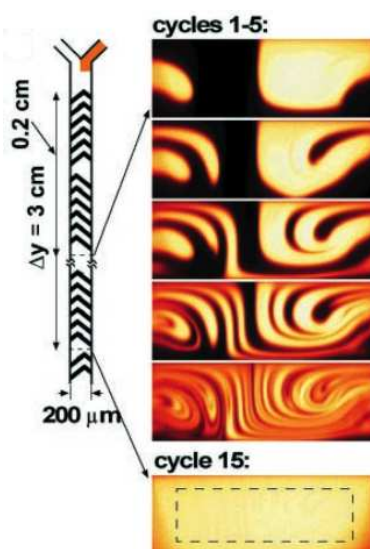


Figure 1.9: Generation of chaotic flows inside a channel allows for the homogenization of the fluid inside a microchannel. At the entrance, two streams are injected, one containing a fluorescent dye. The fluid almost completely homogenizes 3 cm after the entrance. Taken from [Stroock *et al.*, 2002].

These mixing principles have been successfully applied to droplet-based microfluidics. In fact, drops are very attractive mixing chambers. On one hand mixing inside drops can be ef-

ficiently implemented without inducing dispersion. Also, drops can be manipulated to induce chaotic flows inside them and this way achieve fast mixing in their small volumes.

Chaotic flows inside drops may be created in two ways. First through the circulatory flow that naturally occurs in drops while they translate inside a microchannel which may be controlled by manipulation of their trajectory. This is exemplified in the Fig. 1.5(c), where drops are forced to flow through a serpentine channel [Song *et al.*, 2003]. During their path, an alternating circulatory flow is created inside the drops, which allows the mixing of their contents [Stone & Stone, 2005].

A second method to induce chaotic flows inside drops is by the application of external fields that drive fluid flow inside the drops. In fact, external fields (eg. acoustic [Sritharan *et al.*, 2006], electric [Glasgow *et al.*, 2004; El Moctar *et al.*, 2003] and magnetic [Bau *et al.*, 2001] fields) have been used for mixing parallel streams of miscible fluids. However, although mixing inside drops using external fields has been both theoretically [Ward & Homsy, 2001; Grigoriev, 2005; Vainchtein *et al.*, 2007] and experimentally [Frommelt *et al.*, 2008; Grigoriev *et al.*, 2006] proven, few examples exist in the literature of digital microfluidics.

1.2 Flows at the micron scale

Before entering into the bulk of the thesis, we will briefly analyze the physical features of micron scale flows that are relevant for microfluidics. In particular, we will discuss the characteristics of viscous flows, which rule the hydrodynamics of microfluidics, we will compare the importance of diffusion versus the transport due to fluid flow, which sets the difficulty of mixing, and we will introduce the basic capillary phenomena present in digital microfluidics.

Fluid flow at the micron scale often behaves differently than what we are used to in the macroscopic world [Purcell, 1997]. Though not small enough as to make the molecular size to become important, fluid at the micron scale is governed by viscosity and surface forces, contrary to flows at macroscopic scales such as the oceanic streams, atmospheric movements and pipe flows where inertia is relevant and body forces like gravity are important.

To give an idea, imagine a microscopic organism living in a pond. Such an organism cannot simply swim by moving back and forth their flaps (supposing it had any flaps) because this way it would only succeed to sway. Flows at this scale is reversible and therefore small organisms such as bacteria needed to develop swimming strategies that break the temporal symmetry in order to move from one place to another. Another feature of fluids at the micron scale is that force is proportional to velocity, not acceleration. Therefore, while swimming in one direction, a

microscopic organism can stop or turn with no deceleration times. The nature of the flows makes it also very hard for these organisms to reach for food, if they are not fast enough, since their own movement towards the food drags the food itself away. Instead, they can quietly wait for the arrival of food by brownian motion. Finally, for a microscopic organism the surface of the water pond seems like an impenetrable, elastic wall.

These features are consequences of miniaturization and can be explained by considering the relative importance of inertia, viscosity, diffusion and capillarity.

1.2.1 Reynolds number

The flow of an incompressible fluid of viscosity η and density ρ under the influence of a body force per unit volume \mathbf{f} is governed by the Navier-Stokes equation:

$$\rho \left(\frac{\partial \mathbf{v}}{\partial t} + \mathbf{v} \cdot \nabla \mathbf{v} \right) = -\nabla p + \eta \nabla^2 \mathbf{v} + \mathbf{f}, \quad (1.3)$$

where \mathbf{v} is the velocity of a fluid element, p is the hydrostatic pressure and t the time. The Navier-Stokes equation is simply Newton's second principle applied to a fluid particle. The left hand side of Eq. (1.3) is the inertia of the fluid per unit volume, composed by the temporal change of the velocity and the advection of fluid velocity. The right hand side of Eq. (1.3) are the forces per unit volume acting of the fluid element, which account for the hydrostatic pressure gradients ∇p , the viscous dissipation $\eta \nabla^2 \mathbf{v}$ and the body forces per unit volume \mathbf{f} , such as gravity.

To compare the importance of inertial and viscous forces, we write U as the typical value of the velocity magnitude and L for the characteristic length scale over which the velocity vector changes. Typically, the temporal scale of flow can be written as $\tau_{\text{flow}} = L/U$. This allows us to rewrite the inertial forces on a fluid particles as

$$f_{\text{inertial}} = \rho \frac{U^2}{L}, \quad (1.4)$$

and the viscous forces as:

$$f_{\text{viscous}} = \eta \frac{U}{L^2}. \quad (1.5)$$

The relative importance of inertia to viscous dissipation is given by the ratio $f_{\text{inertia}}/f_{\text{viscous}}$. This ratio is known as the Reynolds number $\text{Re} = \rho U L / \eta$ and is widely used in hydrodynamics since it plays a major role in the characterization of flows. Large values of Re ($\text{Re} \gtrsim 10^3 - 10^4$) are typically associated with turbulent flows, since the nonlinear terms of Eq. (1.3) are dominant in

that case. On the contrary, when Re is small the inertial terms of Eq. (1.3) can be neglected, obtaining this way the linear Stokes equation:

$$\nabla p - \mathbf{f} = \eta \nabla^2 \mathbf{v}. \quad (1.6)$$

We can estimate the value of Re in microfluidics by taking the typical values values of L , which are between a few microns and some hundred microns and U which ranges between a few microns to some millimeters per second. Taking the viscosity and density of water as typical fluid properties ($\rho = 1000 \text{ kg/m}^3$ and $\eta = 1 \text{ mPas}$ respectively) we obtain Re values that range between 10^{-6} and 0.1. Therefore, inertial terms are negligible in microfluidics and fluid flow is governed by the Stokes equation. Moreover, body forces can be usually neglected in most cases, since gravitational forces are irrelevant in microfluidics.

Stokes equation, together with the appropriate boundary conditions, fully determine the state of the flow inside a microchannel. In microfluidics, boundary conditions must account for the solid walls of the microchannel, which impose a zero velocity. Boundary conditions must also reflect the way the fluid is injected to the microchannel, usually by imposing a constant flow rate or a constant pressure difference across the channel.

Solutions to Eq. (1.6) are known as Stokes flows (or sometimes creeping flow). Stokes flows are responsible for several features present in microfluidics and in micron scale flows in general. In the first place, the absence of the non linear inertial terms in Stokes equation implies the total absence of turbulence. Indeed, Stokes flows are completely laminar, which means that fluid flows in parallel layers, without intercommunication between layers except for molecular diffusion.

Second, note that time does not interfere in Eq. (1.6), revealing both the instantaneity and the reversibility of Stokes flows. Instantaneity refers to the fact that the state of the flow in one moment does not depend on the initial conditions of the flow. Instead, the whole state of the flow can be deduced from the boundary conditions. Instantaneity also indicates that any change of the pressure gradient reflects immediately in a change of the velocity field, without relaxation times. Reversibility, on the other hand, means that a time reversed Stokes flow also solves Eq. (1.6). In particular, this forces the fluid to go back to its original conditions if the boundary conditions are reversed.

It is important to note, however, that the presence of drops introduces non linearity to the problem. Indeed, drops represent a moving boundary condition that at the same time responds to the flow. Although the presence of drops never implies the apparition of turbulence, it does affect the instantaneity and reversibility of the flow by inducing time dependent boundary conditions and energy dissipation by viscous stresses.

1.2.2 Peclet number

Diffusion is a process in which the thermally agitated molecules of the fluid collision the particles or molecules suspended on it, driving them into movement. The diffusive movement of a single particle consists of a random set of steps in all directions. The random nature of the diffusive process makes it impossible to predict the trajectory of a single particle. However, the mean distance travelled by the particle due to diffusion follows the statistical law

$$\langle \delta x^2 \rangle \longrightarrow Dt, \quad (1.7)$$

where δx is the displacement, D is the diffusive coefficient and t is time. In Eq. (1.7), $\langle \cdot \rangle$ stands for statistical average and \longrightarrow indicates a limit for large times. Note, therefore, that Eq. (1.7) does not describe a particle trajectory, but moreover predicts the average behaviour of a large number of particles. Suppose that we have a container of size L full of water and separated in two halves by means of a membrane; one half of the container has ink dissolved in the water. Equation (1.7) gives an estimate of the time required, once the membrane is taken off, to homogenize the concentration of ink in the water: $\tau_{\text{diff}} \sim L^2/D$. This diffusion time scales as the square of the typical length and therefore it becomes smaller if the size of the chamber is reduced. For example, taking the value of D for a small molecule in water $D \sim 10^{-9} \text{ m}^2/\text{s}$ and for L a typical microchannel width $L \sim 100 \text{ }\mu\text{m}$, we obtain $\tau_{\text{diff}} \sim 10 \text{ s}$.

The relevance of the diffusion time in microfluidics must be related to the flow characteristics. For example, suppose that two streams of water converge to flow along in a straight microchannel, forming a T. One of the streams contains a dye dissolved on it, as shown in Fig. 1.10, and we expect it to diffuse across the width of the channel while the fluid travels downstream. We have seen that small molecules, such as dye, diffuse over a $100 \text{ }\mu\text{m}$ -width channel in $\tau_{\text{diff}} = 10 \text{ s}$ and we wonder: During this time, how far have the molecules moved downstream the microchannel? Two situations can occur, represented in Fig. 1.10. Whether the flow is slow and the fluid is homogenized a short distance after the entrance, or the fluid is fast and both streams travel aside without much interchange.

We can quantify these behaviours by comparing the diffusion time τ_{diff} calculated above to the characteristic time scale associated to the flow $\tau_{\text{flow}} = L/U$, which gives the time required for the fluid flowing at speed U to travel the same distance L . Their ratio $\tau_{\text{diff}}/\tau_{\text{flow}}$ is known as the Peclet number $\text{Pe} = UL/D$ and quantifies the relative importance of advection due to fluid flow to transport due to diffusion. If Pe is small, diffusion dominates; we have the situation shown in Fig. 1.10(a). Conversely, for high Pe advection is dominant and the situation corresponds to the

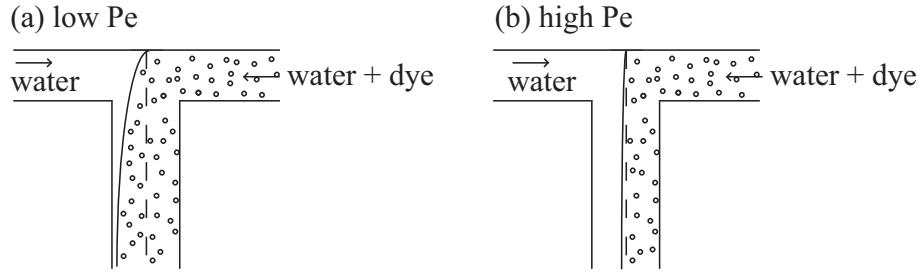


Figure 1.10: Schematic representation of situations where diffusion dominates over fluid advection (a) and viceversa (b).

one shown in Fig. 1.10(b)

The diffusion coefficient depends strongly on the size of the particles. Intuitively, larger particles diffuse slower, because, since diffusion lies in the momentum transfer from molecules of the fluid into the intruder particles, diffusion is less effective in displacing particles of larger mass. This can be quantified using Einstein's law which describes the diffusion coefficient of spherical particles of radius a in a fluid of viscosity η :

$$D = \frac{k_B T}{6\pi\eta a}, \quad (1.8)$$

where k_B is the Boltzmann's constant and T is the temperature of the carrier fluid. Equation (1.8) gives only a general estimate of D for most molecules and particles since it does not take into account the shape or electrical charge of the molecule.

From small molecules dissolved in the fluids to suspensions of large proteins and colloidal particles, D can range roughly from 10^{-9} m²/s down to 10^{-14} m²/s. Consequently, the Peclet number can have a large range of values in microfluidics. Depending of the nature of the fluid and the diffusing particles, there can exist situations where diffusion rapidly homogenize the fluids as in Fig. 1.10(a), favoring the mixing of fluids, or situations where advection completely overcomes diffusion and species travel without noticeably dispersion as in Fig. 1.10(b). The droplet approach of microfluidics favors mixing of the components by decreasing the length L over which diffusion must act without inducing dispersion since all the components remain in the drop.

1.2.3 Capillary number

It is important to note that, as the size is reduced, the surface to volume ratio becomes large. In fact, volume scales as L^3 , while area does as L^2 , so the surface to volume ratio scales as $1/L$.

This means that, as size becomes smaller, surface phenomena such as capillarity or evaporation are important while bulk effects, such as gravity forces, are not. While evaporation is controlled in microfluidics thanks to the confinement imposed by the microchannels and the high impermeability of the walls materials, capillary phenomena are inevitably present in droplet-based microfluidics.

Surface tension

Capillarity refers to the description of an interface between two immiscible fluids. An interface is a transition zone between both fluids whose size is of a few molecular sizes. From a mesoscopic point of view, that is from the point of view of hydrodynamics, an interface corresponds to a geometrical surface between two fluids. However, a microscopic description of an interface is important to understand its properties.

Consider the molecules adjacent to an interface between two fluids. While a molecule in the bulk interacts isotropically with the surrounding molecules through Van der Waals forces, that is not the case for molecules near the interface which are placed in an energetically less convenient position [Fig. 1.11(a)]. An excess of free energy is therefore associated with the presence of an interface. In order to minimize the free energy of the system, the interface tries to use the smallest area possible. Any increase in the area of the interface is energetically inconvenient and can only occur at the expense of mechanical work:

$$dW = -\gamma dA, \quad (1.9)$$

where the coefficient γ that relates linearly the mechanical work dW and the increase of area dA is called the surface tension and is a physicochemical property of both fluids.

Surface tension is responsible for many phenomena observed in daily life. Surface tension makes small bubbles immersed in water to have a spherical shape, allows thin films of soap to form soap bubbles, breaks a thread of water into drops at the outlet of a faucet and sustains objects in the surface of a liquid even if they are denser than the liquid, like some insects that “walk on the water” [Fig. 1.11(b)], for naming a few examples.

Note that the surface tension may also be defined for fluid/solid interfaces. In this case surface tension is a relevant parameter to express the wettability of the surface, this is, the behaviour of a volume of fluid deposited on the solid surface. In fact, three interfaces are involved in this case: Between the fluid deposited on the surface and the solid, between the surrounding fluid and the solid and between both fluids. A comparison between the surface tension associated to each interface defines the wettability of the solid substrate. It could happen that the surface tension

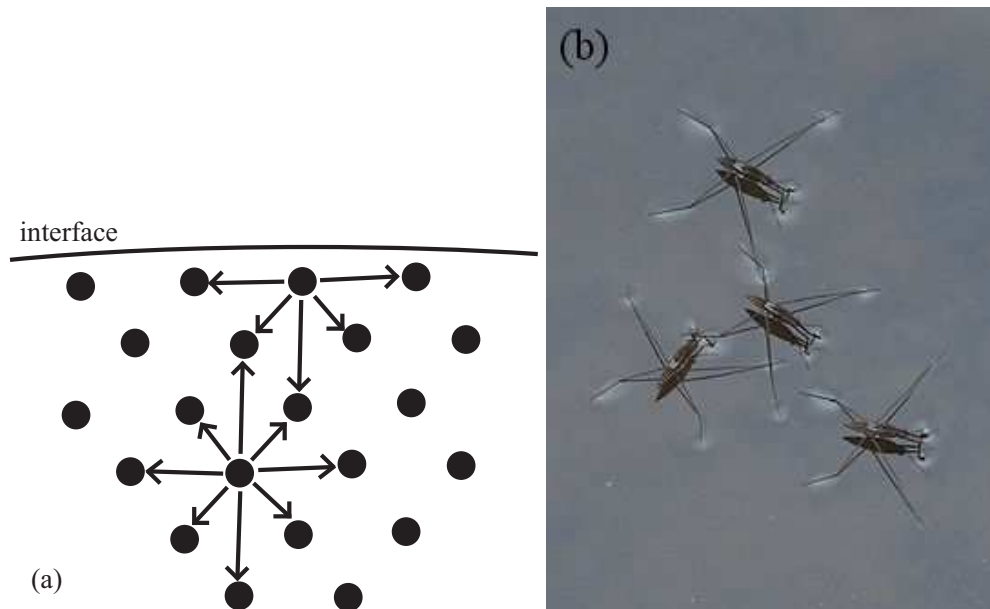


Figure 1.11: (a) Schematic representation of molecular forces. (b) “Water striders”, insects that walk on water.

between the deposited fluid and the solid is very low and it is energetically favorable to form a film of that fluid on the solid, isolating the surrounding fluid from the solid. In such a case we say that the fluid completely wets the surface. On the contrary, it could happen that the competition between the surface tensions makes it energetically preferable to form a “bump” of the deposited fluid on the solid surface. This is called partial wetting. In the case of droplet-based microfluidics the carrier fluid must completely wet the microchannel walls in order to form the drops of the dispersed phase. In most cases, the hydrophobic properties of PDMS favor the use of aqueous drops in organic carrier fluids.

Surface tension is often manipulated by the addition of surfactants, which are molecules that adsorb at the interface between both fluids. Surfactants are amphiphilic molecules, meaning that they are formed by two distinct parts, a hydrophilic head and a hydrophobic tail, as shown in Fig. 1.12(a). In a water/oil interface the head of the surfactants molecules remains in the water phase and the tail in the oil, which is favorable from an energetic point of view, thus lowering the surface tension. Note that we refer to oil and water for simplicity, the same principle acts for different mixtures of immiscible fluids such as water and gas, oil and gas or even different oils, with the appropriate surfactants.

The lowering of surface tension due to the addition of surfactants is highly dependent on the concentration of surfactant dissolved in the fluids [Fig. 1.12(b)]. At low concentrations there is

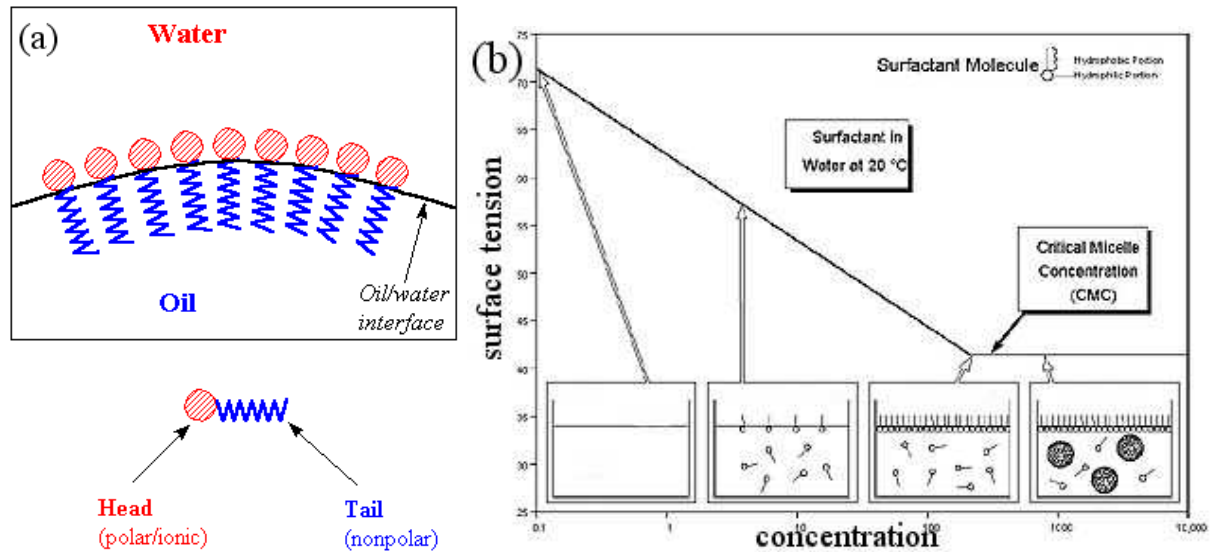


Figure 1.12: (a) Schematic representation of surfactant molecules. (b) Dependence of surface tension with the concentration of surfactant.

plenty of space at the interface for molecules of surfactant to adhere and therefore the surface tension decreases linearly as the concentration of surfactant increases. But there is a point, called the critical micelle concentration or CMC where the interface becomes saturated. From this point, as the concentration of surfactant increases, it is energetically more convenient for the surfactant molecules to form micelles, which are aggregates of surfactant molecules, than to look for an empty spot in the interface to adhere. Therefore, for concentrations of surfactant above the CMC the surface tension only decreases slightly with the concentration of surfactant while the concentration of micelles increases.

Surfactants are widely used in the industry for various uses: foaming agents, stabilization of emulsions or solubilization (detergents). In droplet-based microfluidics, surfactants are usually present to avoid the fusion between drops, stabilizing their surface. Moreover, the use of surfactants is useful to avoid wetting of the channel walls by the dispersed phase.

Marangoni flows

From a hydrodynamic point of view, fluid/fluid interfaces represent a boundary condition that defines the solution of the Stokes equation. Contrary to the solid walls of a microchannel which impose a non-slip condition for the fluid particles adjacent to the wall, interfaces are movable and deformable. Fluid/fluid interfaces, therefore, transmit the movement imposing the continuity of the velocity at the interface. Note that no fluid crosses the interface, so velocity normal to the

interface can only exist if the interface moves in that direction. At the same time, an interface transmits the forces acting on the fluid volumes, imposing the continuity of the stress tensor. In the direction normal to the interface, this condition must take into account the pressure difference that a curved interface may sustain, as defined by the Young-Laplace equation:

$$p_n = 2\gamma H, \quad (1.10)$$

where p_n is the pressure difference between both fluids or Laplace pressure, H is the mean curvature of the surface and γ is the surface tension of the interface. To illustrate the meaning of the Laplace pressure, consider a drop of radius a flowing in a carrier fluid of viscosity η and the normal stress σ_n exerted by the external flow on the drop surface

$$\sigma_n = \eta \left(\frac{\partial v_n}{\partial n} \right)_{r=a}, \quad (1.11)$$

where v_n is the component of the velocity field normal to the drop interface and $\partial/\partial n$ denotes the derivative along the direction normal to the interface. In equilibrium, this viscous stress is compensated by the Laplace pressure $p_n \sim \gamma/a$, but if the viscous stress is too high, the drop can deform or even break. If we take U as the typical velocity of the flow and a as the relevant length scale over which the normal velocity changes, we obtain that $\sigma_n \sim \eta U/a$. The ratio between the viscous stress and the capillary pressure σ_n/p_n is known as the capillary number which is defined as $Ca = \eta U/\gamma$. For high Ca , therefore, the interface is deformed because viscous stresses overcome the capillary pressure, while conversely, for low Ca the Laplace pressure is high and the drop remains spherical.

Besides the normal pressure that an interface may sustain, a tangential force per unit area appears along the interface if the surface tension is not constant. This force is given by:

$$p_t = \nabla_t \gamma, \quad (1.12)$$

where ∇_t indicates the tangential derivative along the surface plane. This tangential force tends to move the interface from low to high surface tension zones.

In the presence of a surface tension gradient, therefore, the interface is set into motion and with it the bulk fluid, which is dragged by the interface. The flow induced by the surface tension gradient is known as Marangoni convection [Schatz & Neitzel, 2001] and it is characterized by a recirculation flow that goes, near the surface, from the low surface tension to the high surface tension region and in the opposite direction far from the interface, in order to ensure mass conservation.

Surface tension gradients may appear due to gradients of surfactant concentration, but also from temperature gradients or the presence of electric fields. In fact, surface tension is a function of temperature, since molecular agitation alters the strength of molecular interactions. For most systems the surface tension decreases with temperature. Moreover, the presence of electric fields induce the formation of electric dipoles in the fluids molecules and therefore a gradient of surface tension appears when an external electric field tangent to the interface is imposed [Levich & Krylov, 1969]. The Marangoni flows due to gradients of surfactant concentration, temperature or electric potential are known as solutocapillarity, thermocapillarity and electrocapillarity respectively.

Drops suspended on a fluid can be set to motion by the imposition of a gradient of surface tension. In this case, circulatory flows inside and outside the drops are created which make the drops to “swim” in the external fluid. Although creating a gradient of surfactant concentration may be difficult, application of voltage differences and temperature gradients is usually simpler. The most commonly used Marangoni method to induce drop movement is the set of an inhomogeneous temperature field, as exemplified in Fig. 1.13 [Jiao *et al.*, 2008].

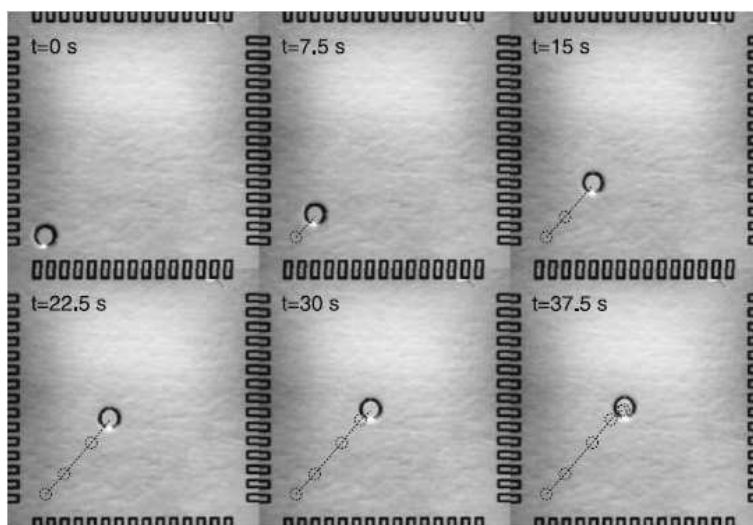


Figure 1.13: Displacement of a drop by means of a thermal gradient. Taken from [Jiao *et al.*, 2008].

Note that the presence of surfactants can reduce the gradients of surface tension that induces a temperature gradient or an electric field by inhomogeneously covering the interface [Chen & Stebe, 1997]. In this sense, the Marangoni flows are a result of complex competitions between hydrodynamics and physicochemical processes.

1.3 The objective of this thesis

1.3.1 State of the art in microfluidic manipulation

The appearance of digital microfluidics allows the creation of LOC devices that use drops as microreactors. Successful implementation of this LOC platform requires the precise and controllable handling of drops. The purely passive methods based on the geometrical control of the fluid streamlines of the fluid that carries the drops can be extremely precise, but lacks the necessary selectivity to act on individual drops and therefore cannot perform sorting of drops beyond separation based on the drop size. For applications requiring the sorting of drops based on their contents, or the selection of individual drops for sampling purposes, passive methods are not sufficient. In these cases, the routing of drops by the application of external fields is a convenient approach that allows the implementation of more sophisticated drop sorting.

The use of external fields can present further attractive since they can be used to perform tasks other than drop routing. In fact, external fields can be used to alter or trigger the process of drop formation [He *et al.*, 2005; Xu & Attinger, 2008], merge (eg. electrocoalescence [Chabert *et al.*, 2005; Ahn *et al.*, 2006a; Link *et al.*, 2006]), split [Link *et al.*, 2006] and detect drops [Niu *et al.*, 2007]. In particular, external fields allow the manipulation of the fluid inside the drop, which is convenient to implement basic functions, such as mixing, or even more complex functions, such as the production of particles [Dendukuri *et al.*, 2005; Carroll *et al.*, 2008].

Examples of external manipulation of drops include the application of different kinds of actuation, such as mechanical valves [Abate *et al.*, 2009], application of electric [Ahn *et al.*, 2006b] or acoustic [Franke *et al.*, 2009] fields and optical manipulation [de Saint Vincent *et al.*, 2008]. Most examples reach a sorting throughput on the order of a few kilo Hertz, which is convenient for LOC applications, usually involved in the analysis of huge libraries. However, only optical forcing is particularly suited for manipulation of individual drops. In fact, acoustic manipulation is based on the generation of acoustic streaming in the bulk fluid and therefore affects all the drops in the focus of the acoustic wave. Similarly, electric manipulation affects all the drops present within the potential gradient. Optical manipulation, instead, based on the utilization of laser beams focused to a spot smaller than a drop size, can achieve control over individual drops.

In fact, laser beams have proven their ability to manipulate small particles with optical forces in a technique known as optical tweezers [Ashkin *et al.*, 1986]. Optical tweezers are based on the difference of refractive index between the medium and the particle and act by injecting momentum into the particle from the deflection of light. In this way, a tightly focused laser beam,

which constitutes an inhomogeneous three-dimensional source of light, behaves as an attractive (or repulsive) potential. Attractive forces can hold particles of up to $10\ \mu\text{m}$ by the creation of forces of up to a few piconewton, thus being useful to manipulate molecules such as proteins and DNA fragments in steady conditions. However, in the presence of fluid flow like the case of microfluidics, optical tweezers do not have enough strength.

This thesis is inspired in three principles relevant for microfluidics: the controlled manipulation of drops by the application of an external field, the manipulation of drops as a whole, including the manipulation of the fluid inside them and the high selectivity of laser actuation. Specifically, this thesis is devoted to the development and characterization of an optical technology for droplet-based microfluidics, able to exert an active control over individual drops and their contents with the aid of a laser beam. In particular, this technology allows the user to:

- Control the trajectory of individual drops inside microchannels.
- Manipulate the flow inside the drops to induce mixing of its contents.
- Tune the size of drops by forcing during the process of drop formation.

The optical tool developed and characterized in this thesis relies on the establishment of a thermocapillary flow inside the drop, which is driven by a strong thermal gradient induced by laser heating of the drop surface. The thermocapillary flow exerts a hydrodynamic force on the drop through viscous shear stresses that push it away from the laser [Baroud *et al.*, 2007a]. This force is able to deviate the trajectory of a drop or even to stop it as it flows in a microchannel, as shown in Fig. 1.14.

Use of a laser beam to realize the heating has several advantages. As mentioned before, the utilization of a laser beam allows for the precise access to individual drops since it can be focused to a small spot. Also, contrary to heating based on microheaters, the application of laser heating does not require any particular fabrication process and therefore this technique is portable and easy to implement. In this sense, the use of a laser, contrary to the application of electric and acoustic fields, does not necessarily introduce complexity to the system. Lasers are widely spread and the laser power needed for the implementation of the thermocapillary force on one drop is on the order of 100 mW, that is, the power of a standard CD-RW burner, thus making this technique a cheap one. Finally, laser heating occurs thanks to absorption of the radiation and therefore can be optimized by the use of an appropriate wavelength or the addition of absorbing dyes.

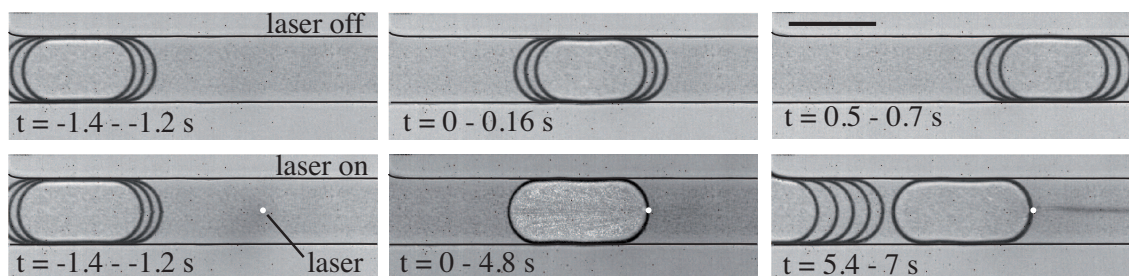


Figure 1.14: Images showing the stopping of a drop with the optical tool of this thesis. In the upper row, no laser forcing is exerted and the drop travels through the channel section at constant speed. In the lower row, the laser forcing is activated. As the drop hits the laser beam, Marangoni recirculation flows appear inside and outside the drop; the inner recirculation is observed with the aid of fluorescent beads. The drop remains stationary during more than seven seconds and is only released when pushed by a subsequent drop. The legends indicate the time with respect to the moment that the interface passes through the laser position. The scale bar corresponds to $200 \mu\text{m}$.

1.3.2 Outline of the thesis

The characterization of the optical tool starts with a study of the laser heating in Chapter 2. For that, the heating of a thin aqueous layer due to the absorption of the laser beam is characterized experimentally and numerically. Although the characterization of the heating is done in the absence of fluid flows and in a different geometry than the experiments performed inside microchannels, the results may be extended to more complex systems by taking into account the heat advection by the flow and the heat dissipation in the microchannel walls. The results of Chapter 2 allow us to estimate the heating by the laser beam in our experiments on a few tens of degrees Celsius, concentrated within a zone of radius of approximately $25 \mu\text{m}$.

Chapter 3 describes both the physical mechanisms involved on the laser-induced force on the drops and the transient and steady features of this force. The physicochemical mechanisms behind the creation of the force originate in an increase of surface tension in the region heated by the laser. This opposes the decreasing dependence of surface tension with the temperature and is explained by a redistribution of surfactant molecules. In particular, surfactant molecules are ejected from the heated zone, thus increasing locally the surface tension. The increase of surface tension drives a Marangoni flow along the drop interface which is directed towards the laser position. The shear stresses produced by the external fluid on the drop interface are responsible for the net force exerted on the drop. Moreover, we deduce that the confinement produced by the microchannel walls is fundamental for the development of the force, since most of the shear stress is produced in the thin films of the continuous phase fluid that exist between the

microchannel walls and the drop.

With respect to the features of the force, we show measurements of the maximum net force exerted on the drop, which is on the order of 100 nN and depends on the magnitude of the thermal gradient. From observations of the temporal evolution of the Marangoni flows as the drop reaches the laser, the development of the force is found to depend on the dynamics of heating. Specifically, we find that the time scale over which the force is developed corresponds to the time necessary to heat the surface. In this way, drops that travel too fast do not allow for the establishment of the necessary thermal gradient and cannot be stopped.

In Chapter 4 we explore the potential applications of the laser tool for controlling drops in microfluidics. In particular, we use holographic tools to dynamically change the laser beam into several spots or even into continuous line patterns of light, multiplying the positions and times where laser forcing is exerted. In this way we demonstrate that, while still performing individual manipulation of drops, this manipulation can be expanded independently to several drops simultaneously. To exemplify this, we perform two microfluidic functions: routing of drops and storage of drops. In the first function we alternatively send drops in one of the three ways of a trifurcation. This, together with some method of detection constitutes a sorter of drops and could be particularly useful in parallel LOC applications. The second function allows the observation of a single, or several drops that are kept stationary in the microchannel, while subsequent drops are deviated. Storage of drops allows the sampling of drops or the realization of analyses with long reaction times.

The possibility of manipulating the inner drop flow with the laser beam is demonstrated in Chapter 5. Here, the Marangoni flow induced inside the drop by solutocapillarity is used to achieve the mixing of the contents of the drop. For that, we impose a temporal modulation of the laser heating by switching the laser between two positions. This is enough to drive a chaotic flow inside the drop, which therefore mixes efficiently the drop contents.

Finally, Chapter 6 explores a different functionality of the laser beam beyond the Marangoni flows. Here, the laser heating, whose power is sinusoidally modulated, is used to locally vary both the surface tension and the viscosity of the dispersed phase, thus inducing a periodic perturbation in a co-flowing drop formation. We show that, in the jetting regime, the flow synchronizes to the frequency imposed by the laser perturbation, which therefore allows the tuning of the frequency of drop formation and of the drop size. In this way, the high dispersion in the drop size inherent to the jetting regime is reduced and the formation of monodisperse drops is achieved.

Chapter 2

Time-resolved temperature rise in a thin liquid film due to laser absorption

Article appeared in *Physical Review E*, **79**, 011201, (2009)

2.1 Introduction

Laser radiation offers a useful technique to heat an absorbing sample in a localized way. Indeed, since a laser beam can be focused to its diffraction limit, it can be used to inject energy at scales that are difficult to reach with other techniques, without requiring any specific micro-fabrication such as electrode deposition. Examples of applications where such heating has been applied include the evaporation of contaminants [Fushinobu *et al.*, 1996], the study of Marangoni flows [Da Costa, 1993], the measurement of media properties such as small absorbancies [Gordon *et al.*, 1965] and Soret coefficients [Rusconi *et al.*, 2004], the study of cell processes [Reinhardt *et al.*, 2007] and of material properties under high pressure and temperature conditions in diamond anvil cells [Ming & Bassett, 1974]. However, heating can also appear as an undesirable side effect in optical manipulation studies [Mao *et al.*, 2005].

Recently, laser-induced heating was used to provide active control over droplet evolution in microfluidic channels, through the local manipulation of surface tension between water and oil [Baroud *et al.*, 2007a]. In these studies, a laser was focused through a microscope objective onto the surface of a water drop in order to locally vary the interfacial tension and thus create a Marangoni flow. The net force due to this flow provides a way to control drop formation, routing, fusion, and division [Baroud *et al.*, 2007b].

The potential usefulness of the laser heating is limited in two ways. First, it is important

to quantify the dynamics of the temperature increase; even though miniaturization leads to a reduction of the thermal inertia and a shortening of the characteristic heating time, this time often needs to be compared with other short times, such as the time for the drop interface to pass the laser position in the example of microfluidic drop control.

Second, many applications, such as thermophoresis or thermocapillarity, depend on the temperature gradient rather than the temperature itself, making it important to know the size of the region that is heated by the laser. Indeed, although the heating is localized, the width of the hot region is expected to be larger than the size of the laser waist. Moreover, in practical applications of microfluidics or optical traps the temperature rise in the liquid can damage some biological samples or skew chemical measurements inside the microfluidic droplet.

In what follows, we concentrate on the heating of a thin liquid layer by a continuous wave laser that is focused to a small spot inside the sample. The presence of the top and bottom solid boundaries plays a fundamental role in the heat flux in our geometry, contrary to the assumptions in the existing work on the subject which addresses a localized heating in an infinite medium [Gordon *et al.*, 1965; Carslaw & Jaeger, 1959; Liu *et al.*, 1995; Peterman *et al.*, 2003; Mao *et al.*, 2005]. Fluorescence measurements of temperature provide spatially and temporally resolved temperature fields [Sakakibara *et al.*, 1997; Zondervan *et al.*, 2006; Ross *et al.*, 2001] and we correct for thermally induced migration by developing a method based on two different fluorophores. This allows us to explore higher temperature ranges than in previous work [Dühr & Braun, 2004]. Finally, the experimental results are augmented by numerical solutions of the heat equation, which provide a way to explore different wall materials and layer thicknesses.

Below, we begin with a description of the experimental setup and method, followed by a theoretical treatment of the problem in Section 2.3. The results of Section 2.4 are divided into three parts, first describing the dynamics of the temperature rise in the transient regime, followed by the steady state spatial distribution, and finally by the results of the numerical simulation. The discussion summarizes the results and comments on their utility for predicting the temperature field in specific cases.

2.2 Experimental setup

The experimental setup consists of an inverted microscope (Nikon ECLIPSE TE2000-U) with epi-fluorescent illumination from a metal halide lamp (Exfo X-Cite 120), as shown in Fig. 2.1(a). An infrared laser beam of wavelength $\lambda = 1480$ nm is collimated to a parallel Gaussian beam whose radius is measured at $\omega_1 = 2.2$ mm. The laser is focused inside the sample through the

Table 2.1: Thermal properties of the materials at room temperature. The material properties can vary with temperature.

	Diffusivity χ	Conductivity κ	Absorption coefficient α
Water	$1.3 \times 10^{-7} \text{ m}^2/\text{s}$	0.54 W/m K	2354 m^{-1}
Glass	$8.5 \times 10^{-7} \text{ m}^2/\text{s}$	1.38 W/m K	39.3 m^{-1}
PDMS	$1.4 \times 10^{-7} \text{ m}^2/\text{s}$	0.18 W/m K	14.3 m^{-1}

microscope objective (Nikon, Plan Fluor 10x/0.3) of focal length $f = 20 \text{ mm}$ to a Gaussian spot whose waist can be calculated, using Gaussian optics, to be $\omega_0 = \sqrt{n\omega_1^2/[1 + (Z_1/f)^2]}$. Here, $n = 1.5$ is the refractive index of glass and $Z_1 = \pi\omega_1^2/\lambda$, which yield $\omega_0 = 5.3 \mu\text{m}$. The laser power P_0 is measured at the sample position through a single glass slide and spans the range 10.5 to 132.8 mW.

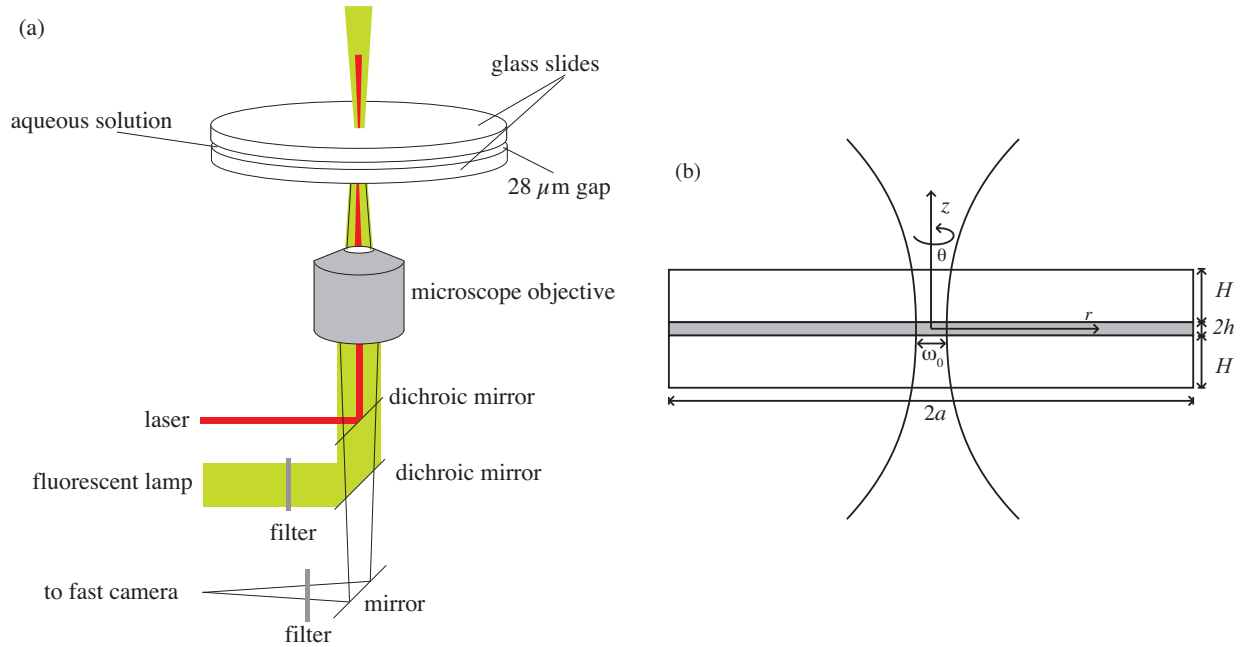


Figure 2.1: (a): Experimental setup. (b): Lateral view of the sample (not to scale).

At this wavelength, part of the optical power is absorbed by the water, while the solid walls absorb almost none, as shown by the absorption coefficient α of Table 2.1. This table also lists the thermal diffusivity χ and thermal conductivity κ for the three materials that will be discussed below.

Fluorescence images are recorded using a fast camera (Photron Fastcam 1024 PCI), triggered by the same external signal as the laser, taking images at 500 frames per second (fps). For each

measurement, 50 images are recorded before the laser is switched on and averaged to be used as a room temperature background. The fluorescence of the heated sample is then followed by recording 500 images after the trigger signal. The imaged region is a 1.74×1.74 mm square. The spatial resolution of our measurements ($1.7 \mu\text{m}/\text{pixel}$) is given by the microscope objective and the number of pixels on the camera sensor. The temporal resolution, on the other hand, is limited by the sensitivity of the camera sensor, which dictates the maximum frame rate that can still yield sufficient contrast between the hot and cold regions. For our conditions, this time is 2 ms.

The sample, sketched in Fig. 2.1(b), consists of $200 \mu\text{L}$ of a fluorescent aqueous solution confined between two glass slides of diameter $2a = 76.2$ mm and thickness $H = 1$ mm. A ring of photoresist (SU-8 2035, Microchem) of inner diameter 13 mm (not shown) is patterned on one of the glass slides by lithography and forms the chamber which contains the solution and prevents its evaporation. The height of the ring, $2h = 28 \mu\text{m}$, was measured using a contact profilometer. Finally, a 150 g weight is set on the upper glass slide to squeeze out the excess solution and seal the chamber. The resulting thickness of the liquid is small compared to the absorption length of the water ($425 \mu\text{m}$), so that the Beer-Lambert law for laser absorption can be approximated by its linearization. The thickness is also small compared to the Rayleigh zone, $L_R = \pi\omega_0^2/\lambda \approx 130 \mu\text{m}$, which defines the distance over which the beam can be considered focused. The laser can therefore be considered divergence-free over this length.

2.2.1 Fluorophore solutions

Two different solutions are used in this study: the first is a Rhodamine B (Rho B) aqueous solution (Reactifs RAL, MW = 479.02, 50 mg/L in 50 μM HEPES buffer, pH = 7), whose fluorescence quantum yield (emitted quanta per absorbed quanta) decreases with temperature [Karstens & Kobs, 1980; Casey & Quitevis, 1988], and whose fluorescence variation can be calibrated over a wide range of temperatures [Ross *et al.*, 2001]. The second is an aqueous solution of Rhodamine 101 (Rho 101) (Fluka, MW = 490.59, 30 mg/L in 50 μM HEPES buffer, pH = 7) whose fluorescence quantum yield is virtually independent of temperature [Karstens & Kobs, 1980; Sakakibara *et al.*, 1997; Marcano & Urdaneta, 2001]. The two molecules are similar and have a similar size, the main difference being the presence of diethylamino groups in the Rho B molecule, whose rotational freedom makes its quantum yield sensitive to temperature [Karstens & Kobs, 1980].

The calibration of the fluorescence dependence of the Rho B solution on temperature is done, in the absence of the laser beam, by placing a 150 mL beaker of hot water on top of the glass

slides. Thermal contact between the reservoir and the sample is provided by a layer of water, which allows us to consider that the sample temperature is the same as the beaker's. The temperature of the water reservoir is monitored as it cools down from 80°C to room temperature. For every 1°C step, thirty images of the sample are taken at a frame rate of 500 fps and normalized by an image taken at room temperature, to correct for inhomogeneous illumination. The fluorescence dependence on temperature is obtained as the spatial and temporal mean value over the thirty images, which is then fitted with a quadratic function, as shown in Fig. 2.2. Note that the sample temperature is shifted to lower values with respect to the monitored temperature due to heat transfer into the surrounding air at room temperature, the shift being higher at higher temperatures. This fact is estimated using a convection heat transfer model [Incropera & De Witt, 1985] due to natural convection in the air and produces the error bars shown in Fig. 2.2.

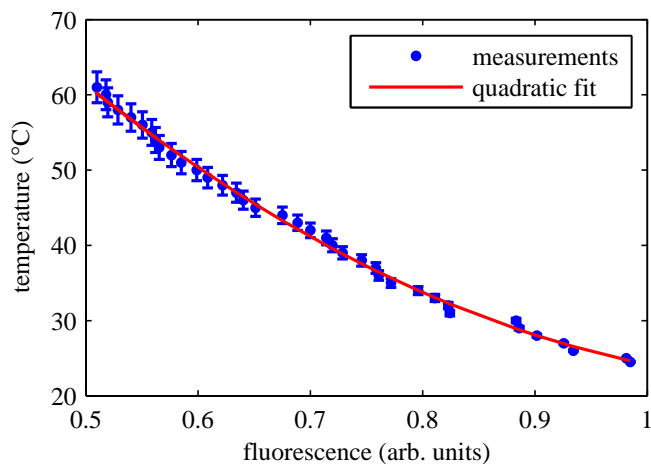


Figure 2.2: Temperature calibration of the Rho B solution fluorescence.

2.2.2 Thermophoresis correction

When the laser is turned on, a decrease in fluorescence intensity around the laser focus is observed for both solutions. The details of the decrease, however, differ for the two dyes: In the case of Rho 101, the dark central spot is surrounded by a bright ring at a radius $r \approx 50 \mu\text{m}$, as shown in Fig. 2.3(a). At later times, the dark spot continues to become darker even after one second of heating [Fig. 2.3(b)]. Simultaneously, the ring expands and becomes less bright, in such a way that the total intensity, defined as the intensity integrated over the whole image, remains constant as a function of time [Fig. 2.3(c)].

The azimuthal average of the Rho B solution, plotted in Fig. 2.3(d), displays a stronger decrease than in the former case and no evidence of a bright ring is present. Furthermore, the fluorescence at the laser location initially decreases much faster, followed by a slower evolution [Fig. 2.3(e)]. Finally, the total fluorescence intensity of Rho B is not conserved, as shown in Fig. 2.3(f), although the total fluorescence intensity returns to its initial value once the laser is switched off.

Since the Rho 101 fluorescence quantum yield is not sensitive to temperature, the dark spot is solely due to a decrease in the concentration of dye molecules. This migration of molecules is due to their diffusion down the thermal gradient, an effect known as thermophoresis, thermal diffusion or Soret effect [Duhr & Braun, 2004, 2006b]. This is further confirmed by the conservation of the total intensity, indicating that molecules have been redistributed through the sample, the bright ring corresponding to a radial accumulation of the molecules repelled from the high temperature region (“hot spot”). In the case of Rho B the fluorescence decrease is in part due to the temperature dependence of its quantum yield, with thermophoresis responsible for an additional decrease in fluorescence at a slower timescale.

Since thermophoresis cannot be avoided in the presence of inhomogeneous thermal fields, the method we employ takes advantage of the similarity in size between the two Rhodamine molecules to correct the temperature and concentration dependence in the Rho B images by the strictly concentration dependence for the Rho 101. To that end, the same heating experiment is repeated using the two solutions and images are recorded with the same frame rate. The concentration variation is obtained from the Rho 101 images, which is then used to normalize the Rho B image at each time step. In this way, temporally and spatially resolved temperature profiles are obtained.

2.3 Theory

The theoretical description of the heating of a medium by absorption of a laser beam has been addressed by several authors in the past. The first analytical description was developed by Carslaw and Jaeger in 1959 [Carslaw & Jaeger, 1959], who solved the heat equation for an infinitely extended opaque medium, heated by a Gaussian laser beam, using a Green’s function method. The result was later extended in 1965 by Gordon et al. [Gordon *et al.*, 1965] for an infinitely long cylinder. However, neither formulation takes into account the presence of top and bottom boundaries which play a major role in dissipating the heat. For this reason, the temperature increase predicted by both formulations highly exceeds our measurements.

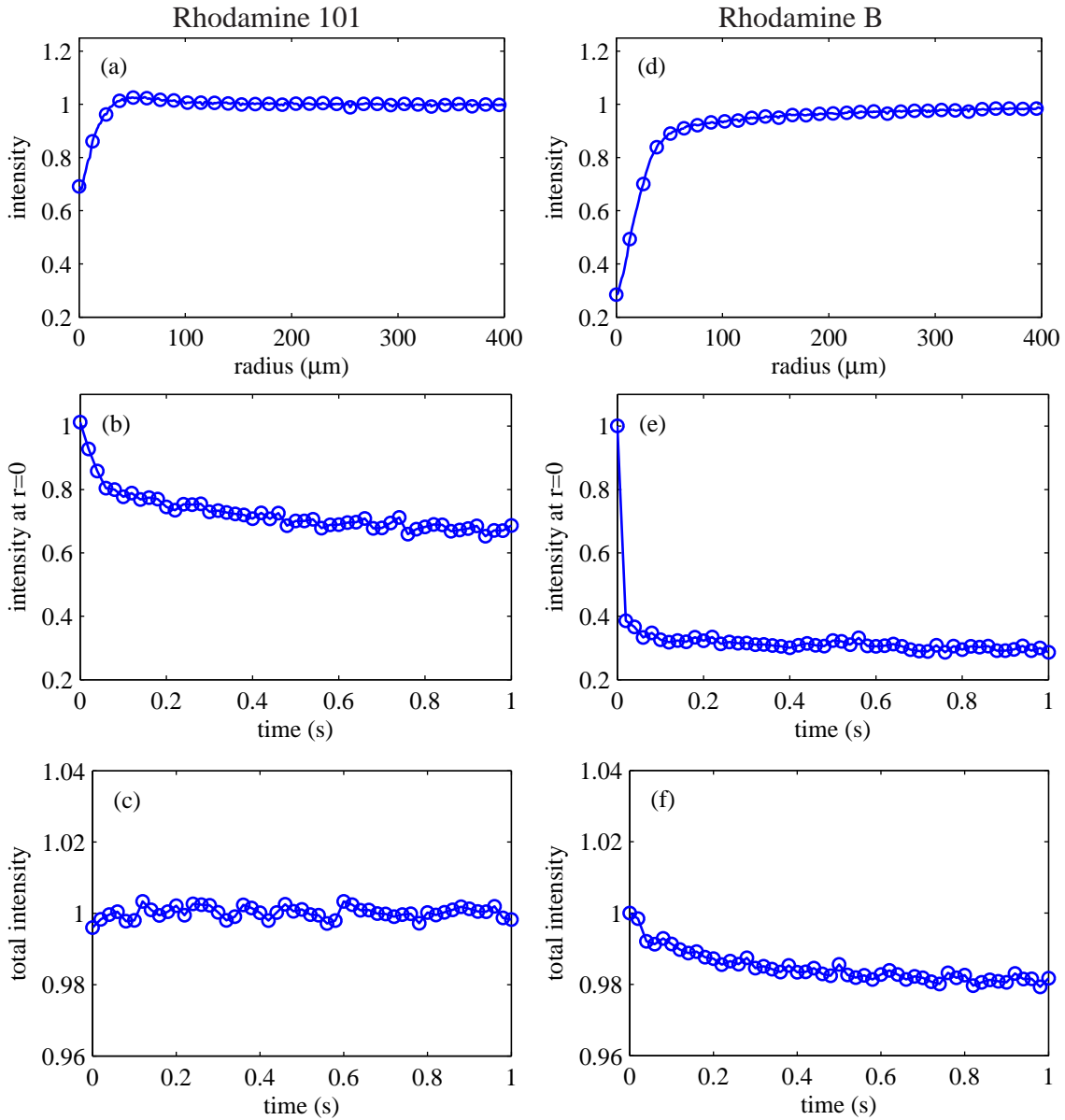


Figure 2.3: (a) and (d): Radial fluorescence profiles after 1 s of laser heating with $P_0 = 76.4$ mW for the Rho 101 and Rho B solutions, respectively. (b) and (e): Fluorescence intensity at $r = 0$ as a function of time for the Rho 101 and Rho B solutions, respectively. (c) and (f): Total fluorescence intensity as a function of time for the Rho 101 and Rho B solutions respectively. The fluorescence intensity is measured in arbitrary units.

More recent work describes the heating caused by the highly focused laser beams used in optical traps [Liu *et al.*, 1995; Peterman *et al.*, 2003; Mao *et al.*, 2005]. Again, the effects of the boundaries are neglected, this time based on the fact that the laser absorption is produced in a spherical region of the size of the laser focus. For the high numerical aperture optics of optical traps, this is typically of the order of $1 \mu\text{m}$, much smaller than the size of the chamber. In our system, however, the size of the heated volume is comparable to the chamber thickness and therefore a different model is necessary to describe the laser heating.

Consider a liquid layer, of thermal conductivity κ and thermal diffusivity χ , contained between two solid walls of thermal conductivity κ_S and diffusivity χ_S , as sketched in Fig. 2.1(b). The absorbing liquid is heated by a laser beam, focused at $r = 0$, whose intensity follows a Gaussian distribution $I(r) = 2P_0/\pi\omega_0^2 \exp(-2r^2/\omega_0^2)$. The total absorbed laser power is $P_{\text{in}} = 2\alpha hP_0$, where α is the absorption coefficient of the medium at the laser wavelength. The whole system is immersed in a thermal bath at room temperature. Since $a \gg \omega_0$ and $H \gg 2h$, the temperature rise is negligible at the lateral boundaries, $r = a$, and at the outer limits of the walls, $z = \pm(H + h)$.

The elevation of temperature in the fluid, T , is described by the heat equation with a heat term \dot{q} due to the laser absorption [Carslaw & Jaeger, 1959; Gordon *et al.*, 1965; Rusconi *et al.*, 2004]:

$$\frac{\partial T}{\partial t} = \chi \nabla^2 T + \frac{\chi}{\kappa} \dot{q}, \quad (2.1)$$

$$\dot{q} \approx \alpha I(r), \quad (2.2)$$

completed by the boundary conditions which account for the temperature and heat flux continuity at the fluid/solid boundary:

$$T(r, z = \pm h, t) = T_S(r, z = \pm h, t), \quad (2.3)$$

$$\kappa \left(\frac{\partial T}{\partial z} \right)_{(r, z = \pm h, t)} = \kappa_S \left(\frac{\partial T_S}{\partial z} \right)_{(r, z = \pm h, t)}, \quad (2.4)$$

where the subscript ‘‘s’’ indicates the values in the solid. The external temperature is assumed fixed. As Eqs. (2.3) and (2.4) suggest, the temperature fields in the liquid and solid are coupled and one cannot be solved without the other. This system is easiest solved using numerical simulations, as done below in Section 2.4.

2.4 Results

2.4.1 Dynamics of the temperature increase

Three experimental depth-averaged temperature profiles are shown in Fig. 2.4 for an absorbed laser power $P_{\text{in}} = 4.5$ mW and times corresponding to 2, 4 and 16 ms after the laser is turned on. The temperature in the fluid rises nearly 50°C in a few milliseconds while the hot spot becomes wider. However, the temperature increase remains less than 1.7°C at radii larger than $200\ \mu\text{m}$. The experimental data were accurately fit by a Lorentzian curve:

$$\bar{T}(r, t) = \frac{\Theta(t)}{1 + [r/\sigma(t)]^2}, \quad (2.5)$$

with two fitting parameters: $\Theta(t)$, which corresponds to the temperature increase at the laser location, and $\sigma(t)$, which is the half-width at mid-height of the profile. This form of the temperature field agrees with those published in [Duhr & Braun, 2006a], although the laser powers are much larger here.

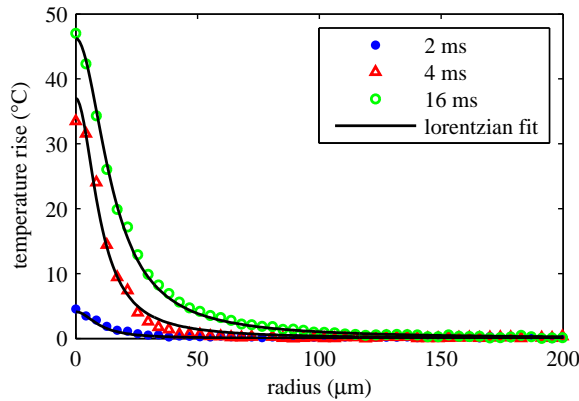


Figure 2.4: Evolution of the radial temperature profile. The laser power is $P_0 = 76.4$ mW, which corresponds to an absorbed power of $P_{\text{in}} = 4.5$ mW.

The evolution of $\Theta(t)$ and $\sigma(t)$ is shown in Figs. 2.5(a) and (b) respectively. $\Theta(t)$ increases rapidly, reaching its maximum value, Θ_∞ , within 10 ms. In contrast, $\sigma(t)$ exhibits a fast increase at small times followed by a slower evolution, still slowly increasing after 1 s of laser heating. This increase is small, however, $\sigma(t)$ remaining around a value of $20\ \mu\text{m}$. For practical purposes, we will consider the steady state to be reached after 0.5 s of laser heating. It should be noted here that a slight difference between the thermophoretic behaviors of the two dyes may induce an error in the temperature field measurement that would be reflected in an unsteady value of $\sigma(t)$.

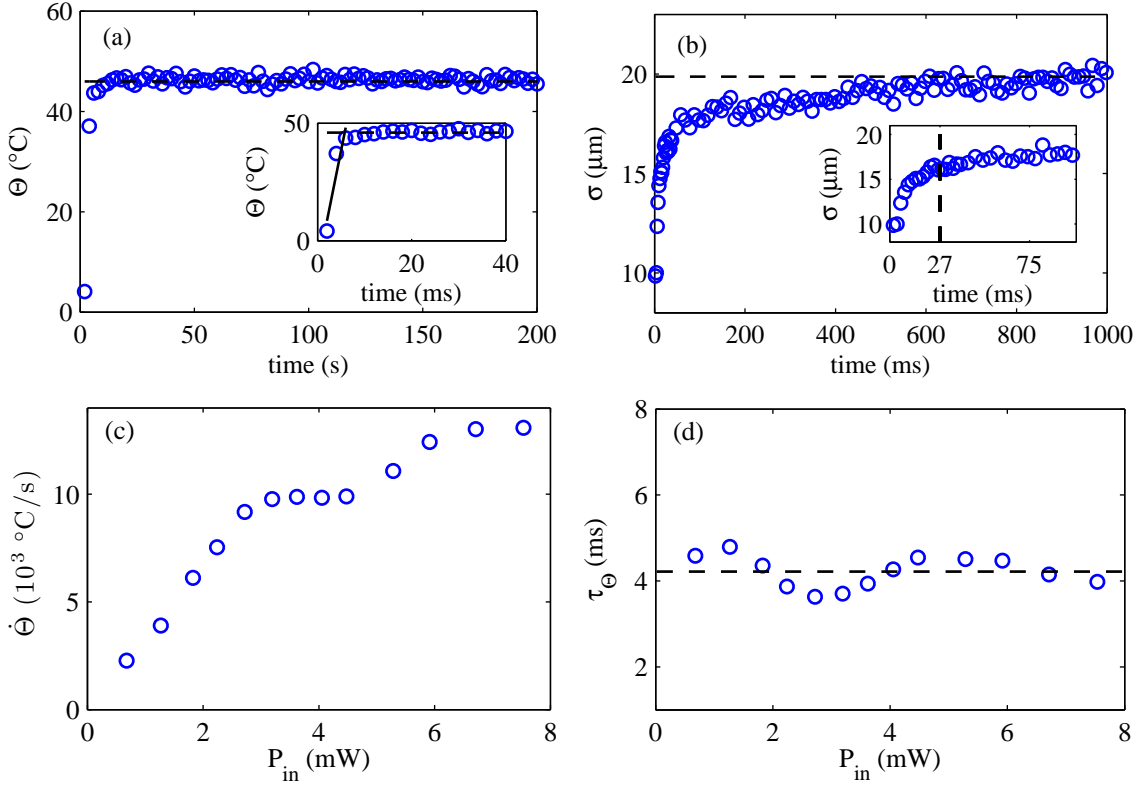


Figure 2.5: (a) $\Theta(t)$ for $P_{\text{in}} = 4.5$ mW. The dashed line indicates the maximum temperature increase Θ_{∞} . In the inset the firsts 40 ms are shown, and the solid line corresponds to a linear fit of the first points. (b) $\sigma(t)$ for the same data. The dashed line indicates the value of σ_{∞} . The inset shows the firsts 100 ms. (c) $\dot{\Theta}$ as a function of P_{in} . (d) τ_{Θ} as a function of P_{in} . The dashed line indicates its mean value.

The heating rate $\dot{\Theta}$ is arbitrarily defined as the slope of a linear fit of $\Theta(t)$ for $t \leq 6$ ms [see inset of Fig. 2.5(a)]. $\dot{\Theta}$ increases with laser power, as seen in Fig. 2.5(c), meaning that the rate of the temperature increase at the origin is larger for larger laser powers. Furthermore, a thermal time can be extracted from this heating rate as $\tau_{\Theta} = \Theta_{\infty}/\dot{\Theta}$. This time scale measures the time necessary to reach the maximum temperature at the laser position. It is independent of the laser power, with a mean value $\langle \tau_{\Theta} \rangle = 4.2$ ms, as shown in Fig. 2.5(d).

Note that it is the gradient of temperature that determines thermocapillary effects. It is interesting therefore to measure the evolution of the gradient as a function of time. From the Lorentzian fit, the maximum thermal gradient occurs at a radius $\sigma(t)/\sqrt{3}$ and its value $-3\sqrt{3}\Theta(t)/8\sigma(t)$ is plotted in Fig. 2.6. Indeed, the fast rise of the central temperature leads to a high value of the gradient at early times, which then asymptotes to its long term value as the hot spot spreads. The time to reach the maximum temperature gradient is well described by the

time τ_Θ for all laser powers. For $P_{\text{in}} = 4.5$ mW and $t = 4$ ms we find $\sigma = 10$ μm and $\Theta = 37^\circ\text{C}$, yielding a maximum thermal gradient of $-2.4^\circ\text{C}/\mu\text{m}$.

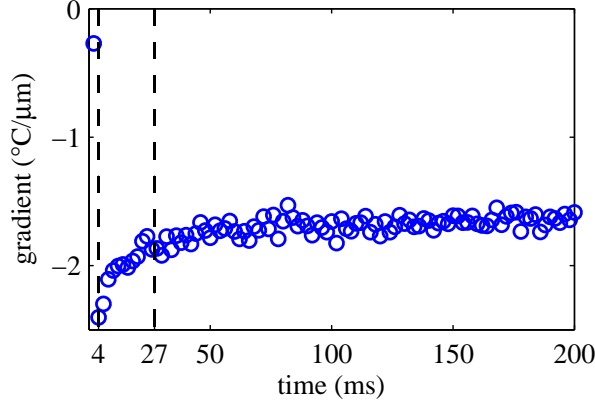


Figure 2.6: Evolution of the maximum thermal gradient after the laser is turned on, for an absorbed power $P_{\text{in}} = 4.5$ mW. The gradient reaches its maximum absolute value at $t = 4$ ms.

2.4.2 Steady state

Next, we consider the depth-averaged temperature field at late times, $\overline{T}_\infty(r)$, which was computed by averaging the temperature distributions between $0.5 < t < 1$ s. An example is shown in Fig. 2.7(a) for an absorbed laser power $P_{\text{in}} = 4.5$ mW. Again, the steady state radial profile is fitted by a Lorentzian curve that gives the temperature increase at the center Θ_∞ and width σ_∞ of the hot spot as a function of P_{in} . Figure 2.7(b) shows that the amplitude Θ_∞ ranges from 10°C for $P_{\text{in}} = 0.68$ mW to 55°C for $P_{\text{in}} = 5.9$ mW, before decreasing again at higher laser powers. This nonlinear behavior is accompanied by a non-monotonic increase of the steady state width of the hot spot σ_∞ as a function of P_{in} , as shown in Fig. 2.7(c).

Note that the temperatures that are measured near the laser location for $P_{\text{in}} > 4$ mW are outside the calibration range of Fig. 2.2. However, the values plotted in Fig. 2.7(b) are obtained from the fit over the whole temperature profile rather than actually observed at the spot center in the experiments. Since the profiles are well described by the Lorentzian curve, we assume that the values that are plotted correspond to the real physical temperatures.

Finally, the thermal energy ΔE stored by the sample, defined as

$$\Delta E = 2h \frac{\kappa}{\chi} \int_0^a \overline{T}_\infty(r) 2\pi r dr, \quad (2.6)$$

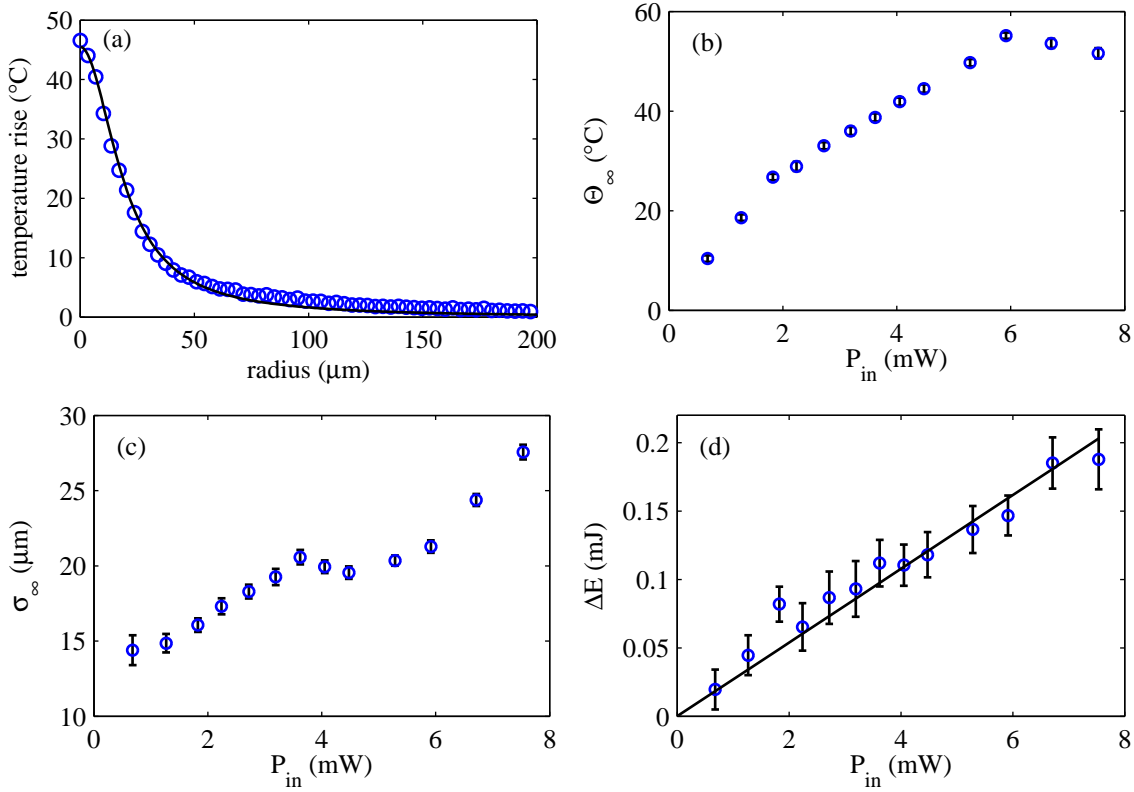


Figure 2.7: (a) Circles: Radial temperature profile after 0.5 s of laser heating at $P_{in} = 4.5$ mW. Solid line: Lorentzian fit. (b) Θ_∞ as a function of P_{in} . (c) σ_∞ as a function of P_{in} . (d) ΔE as a function of P_{in} (circles) and linear fit (solid line). For (b)–(d), the error bars here were calculated as the standard deviation of the data for all the time steps between $0.5 < t < 1$ s.

was calculated by integrating the experimental temperature profiles. ΔE was found to increase linearly with the absorbed laser power P_{in} [Fig. 2.7(d)], even in cases when the maximum temperature decreases. Indeed, the decrease in the value of the temperature near the laser focus is balanced by an increase in the size of the hot region in such a way that the total energy remains linear with the power. The slope of $\Delta E(P_{in})$ can be interpreted as a measure of the time required to reach a heat flux equilibrium between the injected energy and the heat dissipation into the solid walls, and therefore characterizes the time scale of establishment of the steady state. We measure this time as $\tau = 27$ ms, in good agreement with the time taken for the temperature gradient to reach its steady value (Fig. 2.6) and for the temperature profile to reach its final width, as shown in the inset of Fig. 2.5(b).

2.4.3 Numerical simulations

The system of Eqs. (2.1)–(2.4) was solved numerically using finite element commercial software (COMSOL Multiphysics). The values extracted from the simulations were compared with the experimental results, as shown in Fig. 2.8. Quantitative agreement is observed for low heating powers ($P_{\text{in}} < 2$ mW) for the maximum temperature increase [Fig. 2.8(a)], for the shape of the radial temperature profile [Fig. 2.8(b)], and for the evolution of the temperature increase at the laser position $\Theta(t)$ [Fig. 2.8(c)]. This agreement breaks down at higher powers, with the simulations producing higher temperatures. Moreover, the width of the calculated temperature profiles remains almost constant at about $10 \mu\text{m}$, therefore failing to account for the broadening of the profile that is observed in the experiments. However, the calculation of the total stored energy yields a good agreement between the experiments and simulations for all laser powers [Fig. 2.8(d)].

The good agreement between the measurements and the numerical simulations at low laser powers suggests that the numerical calculations can be used to describe the heating for different values of the parameters. The values of Θ_{∞} and of ΔE are shown as a function of the laser waist and the depth of the liquid film in Fig. 2.9(a)–(d). While the temperature increase is very sensitive to both ω_0 and h [Figs. 2.9(a), (b)], the thermal energy depends only weakly on ω_0 [Fig. 2.9(c)], but strongly on h [Fig. 2.9(d)].

These results may explain the discrepancy between the measured and simulated temperature profiles, which disagree in the value of Θ_{∞} while the total energy shows good agreement. This is coherent with a widening of the laser spot in the experiments, which may be due to the creation of a diverging thermal lens in the lower glass slide as its temperature rises [Gordon *et al.*, 1965]. Such a thermal lens would depend on temperature, which accounts for the increasing discrepancy at high laser powers. Evidence of the existence of this thermal lens can be seen when the sample is viewed with transmitted white light; the location of the laser appears darker than the rest, indicating that the material acts to diverge the light.

Finally, the numerical method is used to calculate the temperature increase in a layer of water enclosed between one glass slide and one PDMS wall, such as in the case of a microfluidic device [Baroud *et al.*, 2007a,b]. The value of the thermal conductivity for PDMS is significantly lower than the value for glass (see Table 2.1) implying that heat will be evacuated less efficiently in the PDMS wall. Consequently, the temperature increase is higher and more extended in this case, as shown in Fig. 2.9(e). However, the time scale for the increase of $\Theta(t)$, shown in Fig. 2.9(f), is not significantly modified by the different boundary conditions.

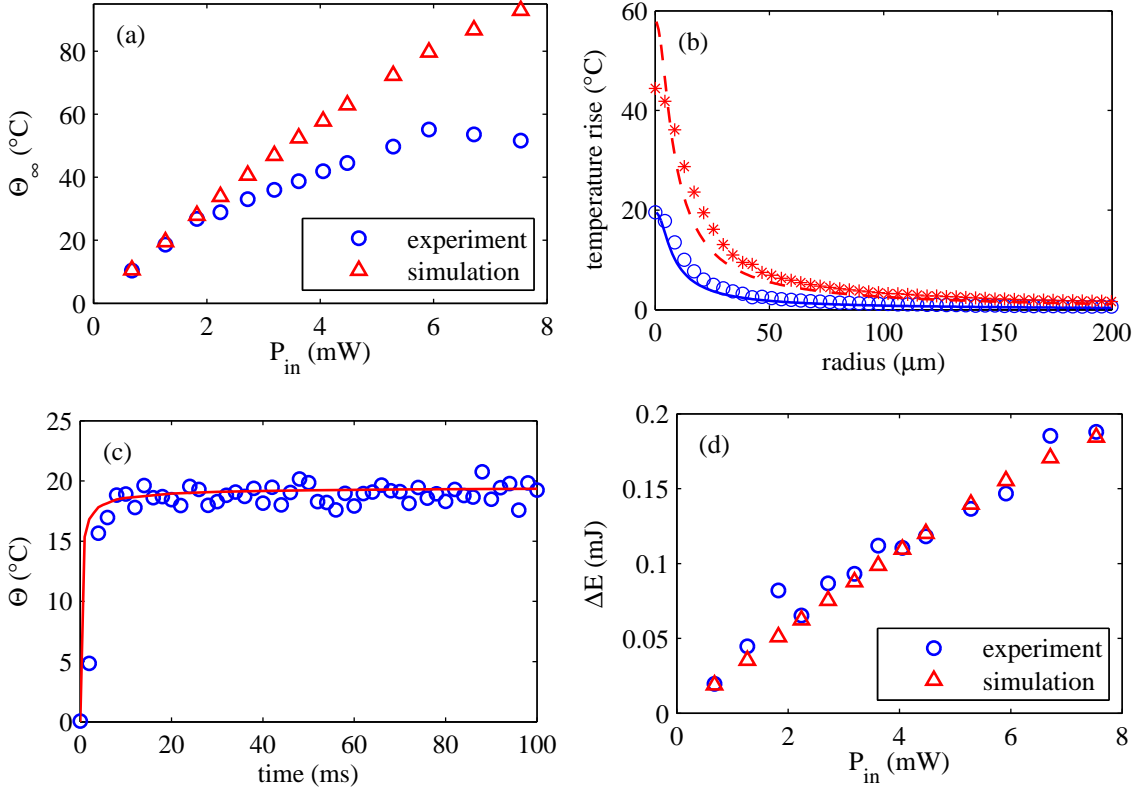


Figure 2.8: Comparison between the experimental and the numerical results. (a) Θ_∞ as a function of P_{in} . (b) Experimentally and numerically obtained radial temperature profiles $\bar{T}_\infty(r)$ for $P_{in} = 1.3$ mW (circles and solid line respectively) and $P_{in} = 4.1$ mW (stars and dashed line). (c) $\Theta(t)$ for $P_{in} = 1.3$ mW. The circles correspond to the experimental measurements and the solid line to the numerical simulation. (d) ΔE as a function of P_{in} obtained by the experiments and by the simulations.

2.5 Discussion

The establishment of a temperature profile by laser heating takes place over several time scales. The fastest one corresponds to the central laser region reaching its final temperature, which also sets the time required to reach the maximum temperature gradient. This time scale is independent of the laser power and is measured at $\tau_\Theta = 4.2$ ms in our experiments. Later, the establishment of the width of the Lorentzian profile occurs over a longer time which is associated with the diffusion of the heat into the solid walls; this time will vary with the material properties, although it is also independent of laser power. In our experiments, we measure $\tau = 27$ ms.

The profile is well described by a Lorentzian curve and the experiments display a non-trivial balance between the width of the hot spot and the height of the temperature peak. These results

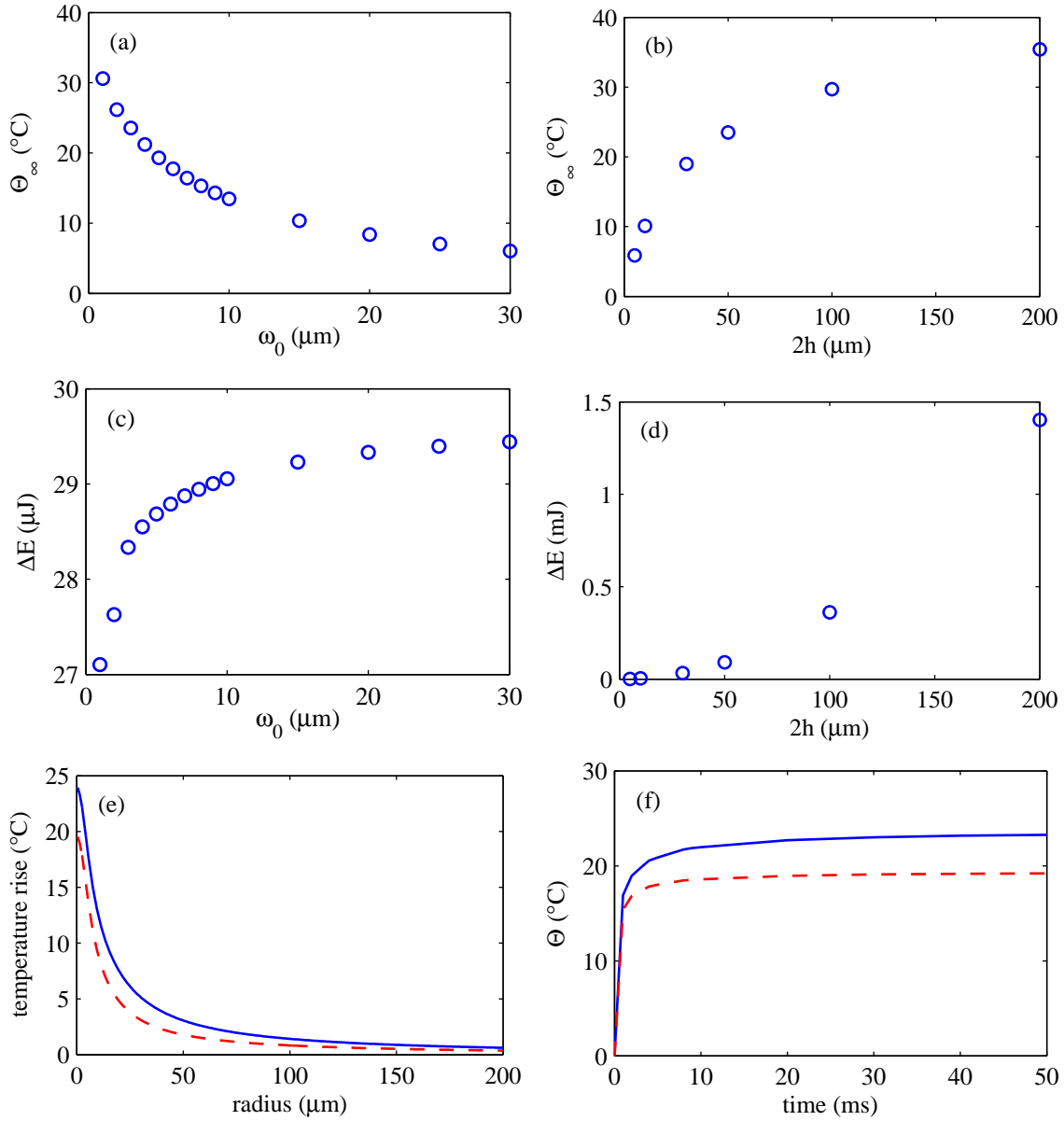


Figure 2.9: Simulated variations of the main parameters for a laser power $P_0 = 20$ mW. (a), (b): Θ_∞ as a function of ω_0 and $2h$ respectively. (c), (d): ΔE as a function of ω_0 and $2h$ respectively. (e), (f): Comparison between $\bar{T}_\infty(r)$ and $\Theta(t)$ for two glass walls (dashed lines) and a combination of one glass and one PDMS walls (solid lines), as in the case of a microchannel.

are not recovered in the numerical simulations, suggesting that the transmission of the laser through the different media is affected by the temperature variations.

Our measurements and simulations can be efficiently used to describe experiments involving laser heating by providing a useful basis for understanding its limitations. Indeed, the steady state profile measured here should still provide a good approximation of the profile expected in the presence of fluid flows, as long as heat diffusion remains faster than advection. This is quantified by the thermal Peclet number $Pe = UL/\chi$, where U is a characteristic velocity and L a characteristic length scale which can be taken as $L = \sigma_\infty$, the width of the hot spot. Therefore, by using the values for water and in the conditions discussed in this paper, we find that $Pe < 1$ for characteristic velocities $U < 1$ cm/s, which is the case in the previous studies on laser-induced droplet manipulation by thermocapillarity [Baroud *et al.*, 2007*a,b*; de Saint Vincent *et al.*, 2008].

Finally, note that our measurements do not take into account the vertical variation of temperature. The numerical solutions show a strong thermal gradient in the z -direction, which depends on the material properties of the walls, as was previously shown [Duhr & Braun, 2004]. These variations should be taken into account if a more precise model of the effect of the thermocapillary flow is needed.

Chapter 3

Marangoni force on a microfluidic drop: Origin and magnitude

Article appeared in *Langmuir*, **25**, 5127–5134, (2009).

3.1 Introduction

Surface tension gradients have recurrently been proposed as a way to apply a force on a drop or a bubble in order to manipulate it. The flows that are produced by these gradients (Marangoni flows) can be of thermal origin, in the case of thermocapillary flows [Young *et al.*, 1959; Brzoska *et al.*, 1993; Sammarco & Burns, 1999; Lajeunesse & Homsy, 2003; Garnier *et al.*, 2003], or of chemical origin through gradients of surfactant coverage of the interface, in the case of solutal Marangoni flows [Bush, 1997; Sumino *et al.*, 2005]. In both cases, the unequilibrated surface tension applies a stress along the interface which leads to the motion of the fluid. Recently these approaches have acquired increasing immediacy with the emergence of droplet-based microfluidics, for which there have been many proposals for fluid actuation based on the manipulation of surface stresses [Darhuber & Troian, 2005].

The generation of a net force by thermocapillary flow was first demonstrated by Young *et al.* on air bubbles located between the anvils of a machinist's micrometer [Young *et al.*, 1959]. The anvils were held at different temperatures, leading to a thermocapillary flow along the surface of the bubble which also induced a flow from the hot to the cold regions in the external fluid. In reaction to this external flow, the drop “swims” up the temperature gradient towards the hot side. The magnitude of the forces generated in those experiments can be calculated by balancing the buoyancy force acting on a bubble of diameter $200\ \mu\text{m}$, i.e. 40 nN, for a temperature gradient of

80°C/cm or equivalently 1.6°C across the bubble.

Recent studies have revisited bubble migration in a temperature gradient in a confined geometry [Mazouchi & Homsy, 2000; Lajeunesse & Homsy, 2003], where a similar mechanism drives the bubble towards the hot region at a velocity that increases linearly with the temperature gradient. However, obtaining a quantitative value of the force acting on the bubble in this case is difficult due to the effects of confinement which couple the bubble shape, the flow, and the net force. In practical situations, further complications appear when the thermocapillary effect is conjugated with the transport of surfactant molecules [Chen & Stebe, 1997; Gugliotti *et al.*, 2002]. Indeed, the interface motion advects the surfactant molecules and can lead to the accumulation of these molecules at the stagnation points on the drop, leading to solutal Marangoni stresses that must be added to the purely thermal effect. These combined phenomena were observed to slow the migration of a drop in a thermal gradient [Chen & Stebe, 1997] or to inhibit the onset of thermocapillary convection along a flat interface [Gugliotti *et al.*, 2002].

A recent series of articles has explored the use of laser heating to manipulate drops of water in oil travelling inside microfluidic channels [Baroud *et al.*, 2007*a,b*; de Saint Vincent *et al.*, 2008]. The laser in these experiments is chosen to heat only the water phase; it is focused to a waist of a few microns and remains stationary. When the leading edge of the drop reaches the position of a laser, the water is heated by absorption of the light and a repulsive force pushes the drop away from the hot spot, i.e. in the direction opposite to the pure thermocapillary case discussed above [Young *et al.*, 1959; Lajeunesse & Homsy, 2003]. This was explained in [Baroud *et al.*, 2007*a*] where observation of the fluid motion showed that the flow was directed towards the hot region along the interface, indicating an increase of the surface tension at the hot spot location.

These observations motivate the present study on the physical and physico-chemical mechanisms responsible for the forcing of microdrops subjected to local heating. Below, we address the two questions of the origin and magnitude of this repulsive force, relying on experimental measurements in a specifically designed microfluidic geometry as detailed in Section 3.2. Section 3.3 studies the spatial redistribution of surfactants by fluorescence microscopy, followed in Section 3.4 by a study of the force magnitude, the velocity fields, and their evolution in time. The results are discussed in Section 3.5.

3.2 Experimental setup

The experimental setup consists of a microfluidic channel in which water drops are formed and transported by an oil flow. A focused infrared laser is used to apply localized heating on the

water/oil interface and images are recorded using a fast camera. The experimental details are discussed below.

Microchannels and microfluidics

The fabrication of the microchannels is performed using standard soft lithography techniques [Xia & Whitesides, 1998]. Briefly, a mold of the channel is microfabricated in dry photoresist (Laminar E7800, Eternal Technology Corp.) by conventional photolithography. A replica of this master is then molded with a 5 mm layer of liquid PDMS (Sylgard 184, Dow Corning), which is then cured at 65°C for 4 h. After curing, the PDMS replica is peeled off and holes are punched at the channel inlets and outlets. The patterned PDMS block is then sealed against a bare glass slide, after an oxidizing plasma treatment that promotes strong adhesion between the parts.

The microchannel geometry is shown in Fig. 3.1. It has a total length of 15 mm, a width $w = 100 \mu\text{m}$ and a thickness $h = 50 \mu\text{m}$. It has three inputs which are connected to three syringe pumps that provide independent control of the different flow rates. The main channel and the second side-channel allow the flow of an organic solution at flow rates $Q_{\text{oil}}^{(1)}$ and $Q_{\text{oil}}^{(2)}$, respectively, while an aqueous suspension flows through the first side channel (flow rate Q_{water}). Drops of water in oil are formed at the first T-junction with a size L set by the two flow rates $Q_{\text{oil}}^{(1)}$ and Q_{water} . Adjusting $Q_{\text{oil}}^{(2)}$ then allows us to vary the total flow rate $Q = Q_{\text{water}} + Q_{\text{oil}}^{(1)} + Q_{\text{oil}}^{(2)}$ and the distance between the drops without affecting the drop formation. In the experiments described below $Q_{\text{oil}}^{(1)}$ and Q_{water} are kept constant at 0.83 nL/s and 0.42 nL/s respectively, so that the drop lengths considered are in the range $L = 330 \pm 20 \mu\text{m}$.

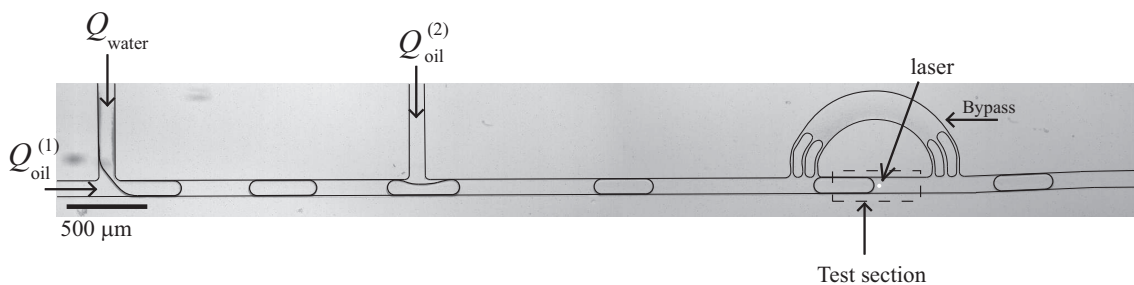


Figure 3.1: Microscope image of the microfluidic device. Drops of water are emitted in oil at the left T-junction. The total flow rate is adjusted downstream by a second oil entry. The drop is trapped by the infrared laser in the test section while oil can flow into the bypass.

The laser blocks the drops in a test section, shown on the downstream side of the figure, which is connected in parallel to a bypass through three 20 μm -wide channels. These structures

act as a filter, allowing the oil to flow through them while forcing the drops to continue in the test channel. The hydrodynamic resistance of the bypass is measured by flowing an aqueous suspension of tracer particles into the device and measuring the relative flow rates in the bypass and the test section, keeping in mind that the pressure gradient acting on the test section is the same as for the bypass. Since the resistance of the test section can be calculated with precision from the Poiseuille law for a rectangular channel [Stone *et al.*, 2004; Tabeling, 2003] (cross section hw and length $L_t = 750 \mu\text{m}$), the ratio of flow rates yields the resistance of the bypass to be $R^b = 7.2 \cdot 10^{12} \text{ Pas/m}^3$.

The organic solution consists of hexadecane (Sigma-Aldrich, viscosity $\eta_o = 3 \text{ mPas}$) as the solvent and an oil-soluble surfactant (Sorbitan monooleate or Span80, Sigma-Aldrich) at 2 wt %. The surfactant Span80 has a neutral polar head and an unsaturated linear tail of 17 carbons, making it quasi-insoluble in water, with a water/oil partition coefficient of $5.5 \cdot 10^{-4}$ [Peltonen & Yliruusi, 2000]. The aqueous solution is ultra pure water (viscosity $\eta_w = 1 \text{ mPas}$) which contains a suspension of green fluorescent latex beads of diameter $0.5 \mu\text{m}$ (Molecular Probes) at a concentration of about 2 beads per $10^3 \mu\text{m}^3$. The beads are used as flow tracers, allowing the velocity field inside the drop to be measured using a commercial Particle Image Velocimetry (PIV) software (Davis, LaVision).

Optics

The experiments are conducted using an inverted microscope (Nikon TE2000) equipped with an epi-fluorescence setup. Image sequences of the drop interface or of the fluorescent beads are acquired with a fast camera (Photron Fastcam 1024PCI) at a frame rate of 250 fps through a microscope objective (Nikon, 10x/0.3). In this way, the velocity field within the drop $\mathbf{u}(x, y, t)$ is computed by cross correlation between two successive images separated by a 4 ms delay, with a spatial resolution of 40×100 vectors. This corresponds to a vertically averaged velocity field since the objective's depth of field is larger than the channel depth.

The laser used in this study is an infrared (IR) fiber-coupled diode laser (Fitel Furukawa FOL1425) emitting a Gaussian beam with wavelength $\lambda = 1480 \text{ nm}$. The fiber is connected to a colimator (Oz-optics) which yields a parallel beam, 2.2 mm in waist. After going through a dichroic mirror, the beam is focused through the microscope objective onto the sample and care is taken to insure that the visible light is focused on the same image plane as for the IR beam. After going through the 10x objective and a glass slide, the beam waist is calculated to be $\omega_0 = 5.3 \mu\text{m}$. The total power P_0 that reaches the microchannel, through the objective and one glass slide, spans the range 55 to 165 mW. Finally, infrared absorption measurements show that

the energy of the laser beam is absorbed mainly by the water. Oil absorbs a hundred times less than water, PDMS a thousand times less, and glass even less than PDMS. The absorption length in water is measured to be $k^{-1} = 425 \mu\text{m}$, in good agreement with the literature [Duhr & Braun, 2004].

When specified, the beam width ω was varied by defocusing the objective by different distances z along the optical axis. ω is calculated as $\omega^2 = \omega_0^2[1 + (nz/z_0)^2]$ with $z_0 = \pi\omega_0^2/\lambda$ and $n = 1.5$ the glass refractive index. Note that z can be either positive or negative with reference to the focused position, depending on whether the microscope objective was raised or lowered.

Temperature field

In Chapter 2, the spatio-temporal evolution of the temperature field in a thin water layer heated by the laser beam was measured and compared with simulations. We summarize the results here: The profile of the temperature rise in a water layer confined between two glass slides takes a Lorentzian shape $T(r, t) = \Theta(t)/[1 + (r/\sigma(t))^2]$, where $\Theta(t)$ is the temperature at the laser position and $\sigma(t)$ the half-width at half-height of the Lorentzian, while r and t represent the radial distance and time, respectively. Two important time scales, both independent of the laser power, were observed: a fast time scale $\tau_\Theta = 4 \text{ ms}$, required to reach the steady value of Θ , and the maximum thermal gradient and a slow time scale $\tau \approx 30 \text{ ms}$ which is associated with the setup of the steady state temperature profile. With a laser power $P_0 = 100 \text{ mW}$ and in a $28 \mu\text{m}$ deep water layer, the steady state values of Θ and σ are 60°C and $20 \mu\text{m}$ respectively. Numerical simulations show the temperature increase is reduced if the laser is focused to a larger waist ω , and that replacing one of the glass slides with a PDMS wall has little influence on the thermal field.

In the present experiments where the laser is only absorbed in the water drops, the maximum temperature is affected in two ways: On one hand, the larger water depth increases the absorbed power thus leading to increased temperature rise. On the other hand, the laser only partially overlaps the drop and is not absorbed by the hexadecane, therefore tending to decrease the maximum temperature in a non trivial way. However, even though the temperature at the laser position cannot be accurately estimated, it is expected to increase with the laser power and decrease when the laser is defocused. Of the remaining parameters, we note that τ_Θ will vary with the depth of the heated layer and is expected to be larger in the present channels than in the thinner layer of Chapter 2.

Finally, the flows are weak enough to neglect heat transfer by convection. Indeed, the thermal Peclet number $\text{Pe} = UL/\chi$ can be estimated using the following values: $U = 1 \text{ mm/s}$ is the

velocity scale of the fluid, $L = \sigma \approx 20 \mu\text{m}$ is the length scale of the hot region and χ is the thermal diffusion coefficient ($\chi = 1.3 \cdot 10^{-7}$ and $8.8 \cdot 10^{-8} \text{ m}^2/\text{s}$ for water and hexadecane respectively). These values yield $\text{Pe} = 0.15$, implying that the heat transfer is dominated by diffusion.

3.3 Role of the surfactant

The crucial role of the surfactant is revealed by a series of experiments performed with pure water drops in pure hexadecane: Without surfactant, the laser is never seen to hold the water/oil interface even at the highest power. Furthermore, tracking some droplets that are atomized by the heating shows that the laser induces rapid flows at the interface, directed from the hot to the cold region. These observations agree with the classical thermocapillary effect but contrast with the observations made in the presence of surfactant as reported in [Baroud *et al.*, 2007a] and in the present study, where the flows are in the opposite direction. In the following, we explore the effects associated with the addition of surfactants to the water/oil system.

3.3.1 Surface tension at equilibrium

The evolution of the interfacial tension between a hexadecane/Span80 solution and pure water is first explored using the pendant drop technique. A pendant drop of $100 \mu\text{L}$ ultra pure water is emitted at the tip of a vertical cylindrical pipette which is immersed in a thermostated oil bath. After an equilibration delay of 3 minutes [Campanelli & Wang, 1999], the interfacial tension γ is obtained from the drop shape [Gast, 1997], taking into account the temperature dependence of the liquid densities [Espeau & Ceolin, 2006].

The temperature dependence of surface tension is measured by increasing the temperature of the oil bath from 23 to 60°C , for a bulk surfactant concentration equivalent to the microfluidics experiments $C = 36 \text{ mol}/\text{m}^3$ (2% w/w). Interfacial tension is found to linearly decrease with the temperature, as shown in Fig. 3.2, with a slope $\gamma_T = -55 \pm 8 \mu\text{N}/\text{mK}$. This measurement rules out the hypothesis of an anomalous thermal dependence of the surface tension that could reverse the sign of the interface velocity compared to the classical thermocapillary effect.

In a second series of experiments, the surfactant concentration C was varied from $52 \text{ mol}/\text{m}^3$ to $0.3 \text{ mol}/\text{m}^3$ at $T = 28^\circ\text{C}$. The value of the variation of $\gamma(C)$ is shown in the inset of Fig. 3.2, which also gives a measure of the critical micellar concentration ($\text{CMC} = 1 \text{ mol}/\text{m}^3$ or 0.054% w/w), the point where γ becomes independent of the surfactant concentration. These measurements are consistent with the values published in [Campanelli & Wang, 1999].

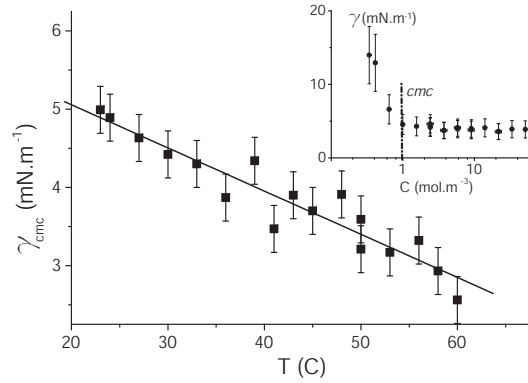


Figure 3.2: Surface tension of a water drop in hexadecane above CMC ($C = 36$ CMC) as a function of the bulk oil temperature, fitted with a linear law (solid line). Inset: Surface tension as a function of the concentration C of surfactant at $T = 28^\circ\text{C}$. The CMC is estimated at 1 mol/m^3 .

We use the Gibbs adsorption equation to describe the equilibrium behavior of Span 80 at the water/hexadecane interface for concentrations below the CMC,

$$d\gamma = -RT\Gamma d \ln C \quad (3.1)$$

and a Langmuir isotherm

$$\Gamma(C) = \Gamma_\infty \frac{K_L C}{1 + K_L C}, \quad (3.2)$$

which lead to

$$\gamma(C) = \gamma_0 - RT\Gamma_\infty \ln(1 + K_L C). \quad (3.3)$$

Here R is the ideal gas constant, T is the absolute temperature, K_L is the equilibrium adsorption constant, Γ_∞ is the maximum surface concentration of the surfactant and γ_0 is the interfacial tension of the water/hexadecane surface without surfactant. Equation (3.3) is found to fit the surface tension data collected by Campanelli and Wang [Campanelli & Wang, 1999] on the same system at $T = 18^\circ\text{C}$ and for a range of concentrations below the CMC. The fit (not shown) provides the following set of parameters: $\Gamma_\infty = 4 \cdot 10^{-6} \text{ mol/m}^2$, $K_L = 110 \text{ m}^3/\text{mol}$ and $\gamma_0 = 52.5 \text{ mN/m}$. This result has three major implications: First, the fact that a Langmuir isotherm applies indicates the existence of an adsorption energetic barrier at room temperature; only the molecules having a high enough energy can be adsorbed or desorbed [Campanelli & Wang, 1999]. Second, since $K_L \text{CMC} \gg 1$, Eq. (3.2) yields an equilibrium surface concentration

that is close to Γ_∞ at the CMC. Finally, the derivative of γ with respect to Γ is

$$\gamma_\Gamma = \frac{-RT\Gamma_\infty}{\Gamma_\infty - \Gamma}, \quad (3.4)$$

which states that the surface tension is sensitive to small variations of Γ when $\Gamma \simeq \Gamma_\infty$ and that γ_Γ has a highly negative value.

3.3.2 Spatial surfactant redistribution

Since the variations of surface tension with temperature do not account for the observed increase in interfacial tension at the hot spot, we now explore the dynamics of surfactant transport as a possible mechanism. Indeed, surfactant molecules can be transported by the hydrodynamic flow, diffusion, or thermophoresis. The effect of these transport mechanisms is to produce unbalanced surface coverage of the water/oil interface with surfactant molecules, which can lead to solutal Marangoni stresses on the interface [Levich, 1962]. Accordingly, we recall some fundamentals of the dynamic variation of surface tension. In a quiescent and isothermal fluid, the partition of surfactants between the bulk and an interface is commonly modeled by a two step process [Eastoe & Dalton, 2000]: First, the molecules diffuse from the bulk to the subsurface, which is a depleted transition layer located near the interface. The size of the subsurface is given by the ratio between the bulk and the interfacial concentration: $\xi = \Gamma/C \approx \Gamma_\infty/C$, which we calculate to be $\xi = 4 \mu\text{m}$ in the conditions of our experiments. The second step is the transfer of the molecules from this subsurface to the interface. The dynamics of this transport depends on the amount of coverage of the interface, with energetic barriers to adsorption appearing for crowded interfaces. The standard picture is that micelles also contribute to providing molecules to the interface in the case of non-ionic surfactants such as Span80 [Eastoe & Dalton, 2000]. They can leak monomers on the microsecond timescale and thus play a role in the dynamic variations of the surface coverage and the exchanges between the interface and the subsurface [Johner & Joanny, 1990]. The relevant concentration that determines the variations of the surface tension, when out of equilibrium, is therefore the subsurface concentration C_s taking into account both the monomers and the micelles. In the framework of the Langmuir isotherm of Eq. (3.2), the rate of adsorption is proportional to C_s and to the number of available interfacial sites ($\Gamma - \Gamma_\infty$). The desorption rate, on the other hand, is proportional to the surface coverage Γ and does not depend on C_s [Eastoe & Dalton, 2000].

The variations in the micelles concentration in the oil phase were measured by marking them with Rhodamine 101, a fluorescent dye (200 mM obtained by dilution in HEPES buffer 1mM,

pH = 7, from a 10g/L stock-solution in DMSO). Although Rhodamine is insoluble in pure hexadecane, it was found to dissolve in the organic phase at high concentration of Span 80 (36-fold the CMC). This is attributed to an aggregation of the Rhodamine molecules within the micelles, since Rhodamine can act as a co-surfactant, owing to its aromatic hydrophobic structure ending in a polar zwitterionic head. This allows the use of Rhodamine as a tracer for the micelles, especially that the fluorescence of Rhodamine 101 is insensitive to temperature variations [Karstens & Kobs, 1980].

The behaviour of the fluorescence field is shown in Fig. 3.3, which shows a drop beginning to interact with the laser. A dip in the fluorescence intensity is observed in the initial moments after the drop begins to be heated by the laser, as shown in Fig. 3.3(a). This local decrease is more visible in Fig. 3.3(c), where the fluorescence intensity is plotted along the solid line of Fig. 3.3(a). The spatial extent of the dip in fluorescence is about $10 \mu\text{m}$, consistent with the size of the heated region at early times. The fluorescent intensity is also shown in Figs. 3.3(b) and (d) for $t = 300 \text{ ms}$, long after the drop has come to a complete halt. The decrease in fluorescence intensity remains but is now spread over a distance of about $\pm 20 \mu\text{m}$, still consistent with the size of the hot region at those times. However, a bright “jet” now crosses the depleted region, indicating a major redistribution of the micelles in the flow and is advected by the mean flow away from the interface. Moreover, an increase in fluorescence is also observed upstream of the laser, corresponding to micelles being transported in the oil layer between the water drop and the PDMS wall, as shown by the intensity profiles measured along the dashed lines.

Finally, a fluorescent ring is observed at the location of the laser once the drop has detached and begun to move, as shown in Fig. 3.3(e). This ring is located on the surface of the PDMS and it can be washed away by flowing the oil for a few minutes. It should be noted that the jetting and the ring at the channel surface can be observed without the fluorescent marking, using diascope illumination. Fluorescence images with Rhodamine allow a sharper contrast and a more quantitative measure of the phenomena.

Taken together, these observations show that the initial surfactant concentration is redistributed in a non uniform way during the blocking of the drop by the laser, with the gradient occurring on a scale comparable with the scale of the temperature gradient at long times, $\sigma \simeq 20 \mu\text{m}$. These length scales are comparable to the depth of the subsurface calculated above, implying that the gradients created by the laser are likely to modify the subsurface concentration in a way to affect the surface tension locally. The hydrodynamic effects of this surface tension variation are studied next.

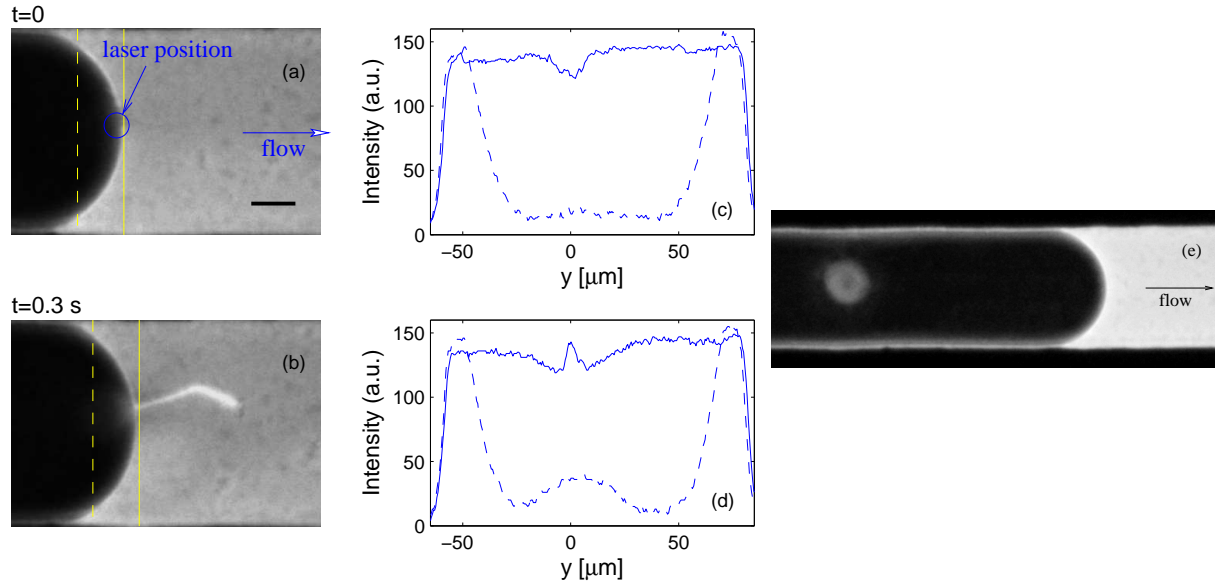


Figure 3.3: (a, b) Fluorescence images of a drop held by the laser in the test section at times $t = 0$ (a) and $t = 0.3$ s (b). The scale bar represents $30 \mu\text{m}$. (c, d) Intensity profiles taken along the solid and dashed lines of images (a, b); (e) Image taken after the drop detachment showing the ring of adsorption of surfactant on the PDMS.

3.4 Hydrodynamics and force balance

We now turn to evaluating the force that the laser heating is capable of producing on a microfluidic drop. A static force balance provides the magnitude of the laser-induced forcing while its dynamic evolution is discussed in light of the flow kinematics.

3.4.1 Steady state force

If the drop is held stationary, a force balance must exist between the hydrodynamic effects that push it to the right and the force of thermocapillary origin that resists its motion. The design of the microchannel with a bypass section of resistance R^b allows us to calculate the pressure difference between the left and right ends of the test section in the same way as for the voltage drop in an electrical circuit. Indeed, if the flux is all directed into the bypass section when the drop stops, then the pressure difference linearly increases with the flux $p = R^b Q$. Since the same pressure difference applies on both the test section and the bypass, the total force that acts on the drop is

$$F = R^b S Q, \quad (3.5)$$

where $S \simeq wh$ is the projected surface of the drop, nearly equal to the cross section of the channel. Using the calibrated value of R^b , this relation predicts the magnitude of the force pushing a stationary drop $F = 180$ nN for $Q = 5$ nL/s.

This evaluation of the force must be corrected by the fact that some fluid manages to flow in the corners between the interface and the walls [Wong *et al.*, 2006; Fuerstman *et al.*, 2007b]. This leakage flow can be taken into account by associating a resistance R^d to the drop of length L [Jousse *et al.*, 2005; Cristobal *et al.*, 2006] in series with the resistance $R^t = 1.7 \cdot 10^{12}$ Pas/m³ due to the shortened test channel of length $L_t - L$. Then, by analogy with an electrical circuit, the total flow rate Q and the test channel flow rate Q_t are related by balancing the pressure differences in the bypass and in the test channel: $Q/Q_t = (R^b + R^t + R^d)/R^b$. The final term that must be estimated is R^d , which is obtained from the measurements of the drop velocity in the test channel (U_0) before interacting with the laser at various Q . By assuming that the drop travels at the mean flow velocity, namely $Q_t = U_0 S$, the slope of the line $U_0(Q)$ yields $R^d = 12 \cdot 10^{12}$ Pas/m³. Finally, the pressure difference across the drop is derived as $R^d Q_t$ and the modified force F' can be estimated as this pressure difference times the channel cross section:

$$F' = \frac{R^b R^d}{R^t + R^b + R^d} S Q. \quad (3.6)$$

We calculate $F' = 100$ nN for a flow rate $Q = 5$ nL/s. F' can be taken as the lower limit for the force the laser has to exert to block the drop, while F , which can be recovered from Eq. (3.6) for an infinite value or the drop resistance, can be taken as an upper bound.

Systematic measurements of the minimum laser power P^{\min} required to stop a drop with a given flow rate were performed and the resulting diagram is shown in Fig. 3.4(a). An arbitrary criterion was chosen to distinguish the drops that were blocked from those that escaped by requiring a minimum blocking time of 200 ms. As expected, P^{\min} increases as the flow rate is increased and the corresponding values of the force, obtained from Eqs. (3.5) and (3.6), display a force in the range of a few hundred nanonewtons. Furthermore, a maximum flow rate $Q^{\max} = 7.9$ nL/s is observed above which drops cannot be held at any laser power. Finally, it is important to note that we observe that blocking longer drops requires a lower value of P^{\min} than for shorter drops (not shown).

In a separate series of experiments, the variations of P^{\min} with the laser spot size ω are explored by defocusing the laser, as described in Section 3.2, while keeping the flow rate constant

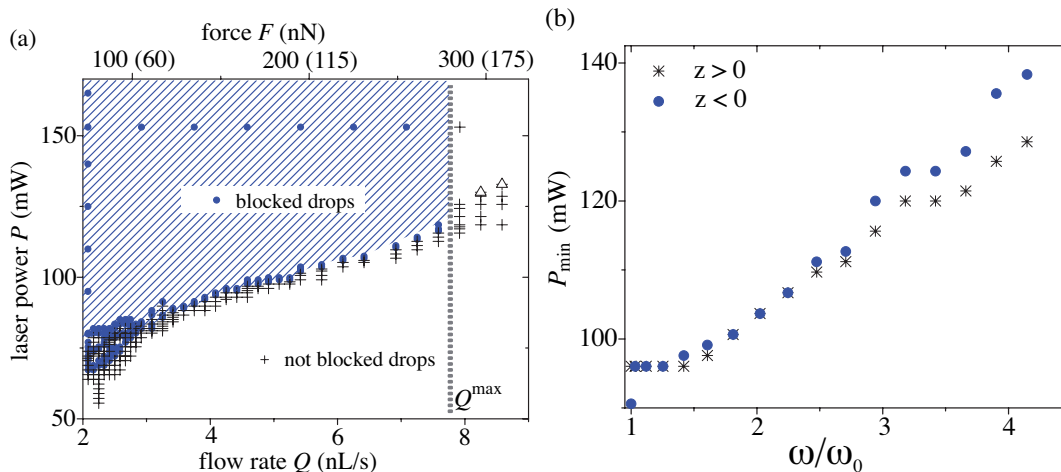


Figure 3.4: (a) Phase diagram showing the blocked drops for different laser powers as a function of the flow rate Q : full circles indicate drop that are blocked and crosses the non-blocked ones. Triangles correspond to cases where water boils. The secondary x-axis shows a conversion of Q into the total force F (F') applied by the laser, taken from Eqs. (3.5) and (3.6), respectively. (b) Minimum power required to block a drop, P^{\min} , as a function of the laser width ω normalized by the waist ω_0 . ω was varied either by increasing the sample to objective distance along the optical axis ($z > 0$) or by decreasing it ($z < 0$). The flow rate is $Q = 3.75$ nL/s.

at $Q = 3.75$ nL/s. The effect of an increase in the laser width is known from our previous study to decrease the temperature at the hot spot while keeping the typical heating time constant. We observe here that the minimum power required to block a drop increases as the beam size is increased, as shown in figure 3.4(b).

3.4.2 Transients before coming to a complete halt

The steady state force computed above [Eq. (3.5)] gives only a partial view of the thermocapillary blocking process. In the following, we turn to the transients that precede the blocking by analyzing the evolution of the fluid velocities measured by the PIV. Figure 3.5(a) displays a superposition of thirty successive images (120 ms) of the tracer particles, showing the presence of recirculation rolls inside the stationary drop. The corresponding velocity field is shown in Fig. 3.5(b), where the calculated field is averaged over 1035 images. The PIV gives an accurate measure of the velocities away from the hot region but the values near the laser position are poorly computed due to the very high velocities near the hot spot. Nonetheless, we observe that the interface of the drop is set into a motion directed towards the laser position as the drop comes to a halt, and the structure of the rolls is clearly recovered. We find that the positions of the roll

centers do not depend on time nor on the total flow rate. They are located at a distance from the drop interface $d = 17 \pm 3 \mu\text{m}$ and at a distance of $25 \mu\text{m}$ from the channel lateral walls, suggesting that the roll position is set by the channel geometry.

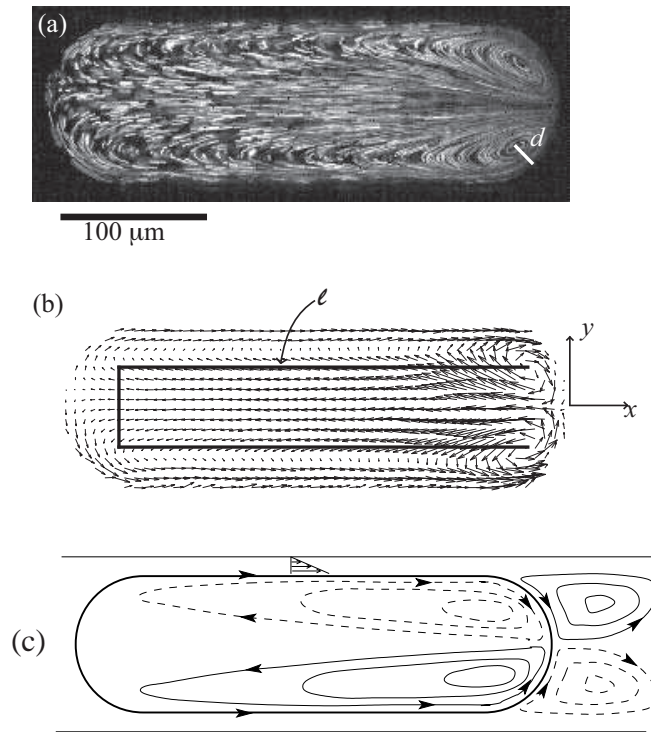


Figure 3.5: (a) Superposition of fluorescence images of a drop held by the laser, showing a pair of stationary rolls. (b) Time-averaged velocity field inside the drop in the steady state. The line ℓ is used for the calculation of the flux which must return through the line d . (c) Schematic of the flow and leakage flow in the thin films between walls and interface, drawn artificially larger.

The drop velocity was determined by averaging the computed velocity fields and is shown in Fig. 3.6 for four values of the flow rate. As expected, the velocity prior to interaction with the laser increases with Q . Upon arriving at the laser position, drops slow to a halt over a few milliseconds and remain stationary for long times. The drop corresponding to $Q^{\text{max}} = 7.9 \text{ nL/s}$, however, escapes after it has been stopped for 80 ms at the laser position.

We focus our attention on the setup time for the flow field inside the drop: A characteristic velocity near the tip is obtained by equating the flux $\varphi(t)$ that flows between the roll centers away from the hot region with the flux through a line that joins the centers of the rolls and the interface. In this way, the accuracy of the velocity data away from the hot region is used to obtain the time evolution of the velocity near the tip, since no flux crosses the interface itself. In practice, $\varphi(t)$ is calculated along the line ℓ in Fig. 3.5(b), as the sum of the normal velocities in the reference

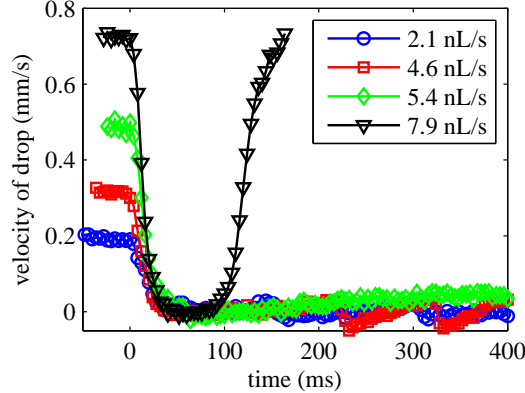


Figure 3.6: Time evolution of the drop velocities U as they reach the laser at four different flow rates $2.1 < Q < 7.9$ nL/s. The laser power is $P_0 = 153$ mW.

frame of the drop. The velocity near the tip v is estimated by equating $\varphi = 2vd$, which yields $v(t) = \varphi(t)/(2d)$.

As the drop reaches the laser position, $v(t)$ displays a rapid increase before reaching a saturation value, as shown in Fig. 3.7(a). Here, the time $t = 0$ is the same as for the drop velocity data $U(t)$ in Fig. 3.6, indicating that the onset of the roll motion occurs simultaneously with the drop deceleration. The data for $v(t)$ were fit with an exponential function, $v_{\text{fit}} = v_{\infty}(1 - e^{-t/\tau_v})$, yielding two important physical parameters: the saturation velocity, $v_{\infty} = 1.3 \pm 0.2$ mm/s, which does not display any dependence on P_0 or Q within the accuracy of our measurements, and the characteristic time τ_v which is also independent of P_0 but decreases with Q from 20 to 6 ms, as shown in Fig. 3.7(b). This time correlates very well with the time required for the drop to travel a distance equal to the laser waist, $\tau_U = \omega_0/U_0$. Several links can be drawn between the above measurements in order to shed light on the underlying physics, as discussed in the next section.

3.5 Discussion

3.5.1 Two limitations

The first conclusion that can be reached from the above measurements is a confirmation of the hydrodynamic origin of the force that is applied on the drop. Indeed, the simultaneity of the onset of the rolls with the drop deceleration is a good indication that the two phenomena are linked.

These results indicate two independent mechanisms that limit the blocking of the drops: The first is associated with rapidly advancing drops which could not be blocked regardless of the laser

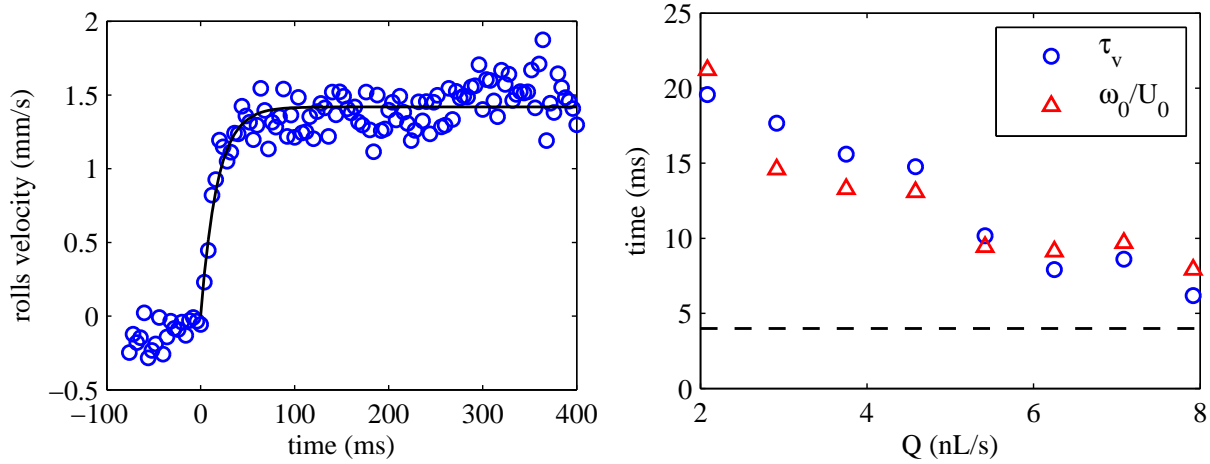


Figure 3.7: (a) Time-evolution of the rolls velocity $v(t)$, in the drop reference frame, as the drop reaches the laser position. Solid line shows an exponential fit to the data. $P_0 = 153$ mW and $Q = 2.1$ nL/s. (b) Characteristic time τ_v , obtained from the exponential fits of $v(t)$, as a function of flow rate Q and time to cross the laser spot, ω_0/U_0 . Dashed line: typical heating time τ_Θ .

power. In this case, the interface passes the laser spot in a time shorter than the time necessary to produce the thermal gradient, indicated by the dashed line in Fig. 3.7(b). The heating is therefore too slow to fully generate the recirculation rolls and block the drop, which slows down at the laser before accelerating back to its initial velocity.

The second limitation applies for slowly moving drops and is set by the magnitude of the force that can be generated for a given laser power, as indicated by the increasing $P^{\min}(Q)$. This interpretation is further confirmed by the results of Fig. 3.4(b), since the time to cross the laser when it is defocused is increased but the temperature gradient is smaller than in the focused case. The increase of P^{\min} with beam size therefore indicates that the limiting factor originates from the force magnitude rather than the setup time, as long as $Q < Q^{\max}$.

3.5.2 Role of the confinement

It was shown in [Baroud *et al.*, 2007a] that the velocity field associated with the capillary driven stress consists of two counter rotating rolls in the outer fluid, in complement to the two inner rolls visualized in Fig. 3.5(a). In a confined geometry such as ours, the resulting stress field can be decomposed into two contributions: one associated with the recirculations near the tip of the drop and the other arising from the strong shear in the thin films between the moving interface and the lateral walls [see Fig. 3.5(c)].

Near the laser position, the force can be estimated by extracting the interface velocity $v_\infty =$

1.3 mm/s from the PIV measurements and using the model of an unconfined circular drop [Baroud *et al.*, 2007a]. The resulting force is $F_{\text{tip}} \simeq 2\eta_o v r \sin^2 \theta = 200$ pN, where $r = w/2 = 50$ μm is the radius of curvature and $\theta = \pi/4$ is the angular position of the roll centers, taken from Fig. 3.5(a). This force is far too small to account for the experimentally measured value of 180 nN.

In the present geometry where the drop almost fills the channel width, the viscous shear stress in the lateral films should also be taken into account. Indeed, since the interface is driven by the Marangoni flow towards the laser position, it exerts a reciprocal stress on the lateral sides away from the laser [see Fig. 3.5(c)]. The magnitude of this force may be written as $F_{\text{films}} = 2\eta_o h L v_s / e$ based on dimensional analysis. Here, $v_s = 0.15$ mm/s is the mean value of the tangential velocity along the length of the drop, measured from the PIV, h the channel depth, L the length of the drop, and e is the unknown film thickness. This film thickness can be estimated from the asymptotic analysis of Wong *et al.* [Wong *et al.*, 2006], for our aspect ratio ($w/h = 2$), as $e/h = 0.45(3\text{Ca})^{2/3}$, where the capillary number is $\text{Ca} = \eta_o v_s / \gamma = 9 \cdot 10^{-5}$ and yields a thickness $e = 0.1$ μm .

The force can now be calculated for a 330 μm -long drop and we obtain $F_{\text{films}} = 160$ nN, in remarkable agreement with the measured force. This contribution to the total force is orders of magnitude larger than the value for F_{tip} which can be neglected when the lateral walls induce strong shear along the body of the drop. Moreover, this analysis also accounts for the effect of the drop length: it explains why longer drops were easier to block than short ones.

3.5.3 Marangoni stresses and interface velocity

The velocity of the interface measured in Section 3.4 can be related to the surfactant and temperature distributions by considering a portion of interface, near the tip of the drop, of local radius of curvature $w/2$. The Marangoni condition can be written from the continuity of the shear stresses at the interface, providing a relation between the normal velocity gradients and the tangential surface tension gradient:

$$\eta_o \left(\frac{\partial v_\theta^o}{\partial r} \right)_{\text{interface}} - \eta_w \left(\frac{\partial v_\theta^w}{\partial r} \right)_{\text{interface}} = \frac{2}{w} \frac{\partial \gamma}{\partial \theta}, \quad (3.7)$$

where v_θ^w and v_θ^o are the tangential velocities in the water and oil, respectively, and r and θ the radial and azimuthal directions.

The typical length scale for the radial variation of the velocity, in both phases, is imposed by the distance d between the interface and the roll centers [Baroud *et al.*, 2007a]. A dimensional

analysis can therefore be used to write the interface velocity v as

$$(\eta_o + \eta_w) \frac{v}{d} \sim \frac{2}{w} \frac{\Delta\gamma}{\Delta\theta}, \quad (3.8)$$

where the \sim symbol indicates order of magnitude scaling and the Δ indicates a variation in a given variable. As discussed in Section 3.3, the change of the surface tension is due to both temperature and surfactant concentration variations. One can write as a first approximation

$$(\eta_w + \eta_o) \frac{v}{d} \sim \frac{2}{w} \left(\gamma_T \frac{\Delta T}{\Delta\theta} + \gamma_\Gamma \frac{\Delta\Gamma}{\Delta\theta} \right), \quad (3.9)$$

where the thermal and solutal contributions can be distinguished.

In the vicinity of the laser, the two mechanisms act in opposition since the increase in temperature decreases the surface tension ($\gamma_T \Delta T / \Delta\theta < 0$), while a depletion of surfactants increases the surface tension ($\gamma_\Gamma \Delta\Gamma / \Delta\theta > 0$). Our visualization of the direction of the interface velocity indicates that the surface tension increases near the laser, implying that the solutal Marangoni effect dominates over the purely thermocapillary effect.

However, a purely thermal Marangoni effect would produce a velocity

$$v_{\text{th}} = \frac{2d\gamma_T}{w(\eta_w + \eta_o)} \frac{\Delta T}{\Delta\theta} = 93 \text{ mm/s} \quad (3.10)$$

for a temperature variation $\Delta T / \Delta\theta = 20^\circ\text{C}/\text{rad}$. When compared with the measurements of $v_\infty = 1.3 \text{ mm/s}$, this suggests that the two antagonistic effects almost compensate, with a slight imbalance in favor of the solutal contribution. This is consistent with other examples of thermo-solutal competition where the thermal and solutal Marangoni mechanisms are almost in exact balance [Chen & Stebe, 1997; Gugliotti *et al.*, 2002].

3.6 Summary

The pushing of microfluidic drops by laser heating is a surprising phenomenon that can potentially play a major role in the lab-on-a-chip technologies if the technique can be applied in practical situations. This study provides the first detailed measurements concerning the physical processes at play, namely the physicochemical aspects related to the force generation and the force magnitude.

Two practical limitations are found for achieving total blocking of moving drops. The first concerns slowly moving drops for which the heating is sufficiently fast to produce the thermo-

capillary rolls. In this case the magnitude of the force increases with laser power reaching 300 nN for our geometry and drop size. The second limitation is due to the time necessary to heat the interface, which prevents rapidly moving drops from being completely stopped. The temporal criterion that must be kept in mind is that the interface should not cross the laser waist faster than the time required to reach necessary temperature gradient, a few milliseconds in our experiments.

The actual values of these two limits can be pushed by intelligent design of the microchannel geometry. Indeed, drops that are longer are easier to stop, suggesting that squeezing a drop by reducing the channel width can be used to increase the blocking force. On the other hand, widening the microchannels reduces the linear velocity for a constant flow rate. These two apparently contradictory requirements can either be applied separately or can be combined by placing discrete pillars for guiding droplets in a wide channel, as shown recently [Niu *et al.*, 2008]. Furthermore, the value of the heating time can be manipulated by varying the volume of fluid that must be heated, for example by reducing the channel thickness.

An important question remains, however, concerning the precise mechanism responsible for the micelle migration and their subsequent local depletion near the hot spot. Several hypotheses can be emitted, for example through the effect of optical forces which act on the micelles or through thermophoresis which would radially displace them away from the hot spot [Bar-Ziv & Moses, 1994; Giglio & Vendramini, 1977; Rauch & Kohler, 2002; Vigolo *et al.*, 2007]. An observation in favor of this last hypothesis is the ring-shaped accumulation built up during the trapping period that partially remains adsorbed on the walls, a similar feature to what is obtained in [Braun & Libchaber, 2002], which was attributed to a thermophoretic effect coupled with a thermal convection. However, the details of the mechanism are probably best dealt with through numerical simulations of the coupled transport equations which can explore the unsteady flows, thermal, and concentration fields in detail.

Chapter 4

Thermocapillary manipulation of droplets using holographic beam shaping: Microfluidic pin-ball

Letter appeared in *Applied Physics Letters*, **93**, 034107, (2008).

4.1 Introduction

Microfluidics and optical manipulation are two independently maturing technologies that enable advanced complimentary studies of objects at the micron scale. In the case of optical manipulation, specifically optical tweezers, one of the major developments in recent years has been that of dynamic holographic optical trapping [Curtis *et al.*, 2002; McGloin, 2006]. These advances are currently providing increasingly complex possibilities in the control of droplets in the micrometer range [Burnham & McGloin, 2006; Lorenz *et al.*, 2007]. In parallel, microfluidics technology promises to provide automation through the miniaturization of biological and chemical systems. Many approaches are being explored towards this goal, of which the manipulation of droplets in microchannels is one of the most promising routes [Song *et al.*, 2003, 2006; Teh *et al.*, 2008]. In digital microfluidics, each droplet can be thought of as containing an independent reaction and one may want to perform either many copies of the same reaction, for example in the case of controlled chemical synthesis [Günther & Jensen, 2006], or, instead, vary the parameters between droplets in order to explore a large number of combinations [Laval *et al.*, 2007].

The success of the latter case depends crucially on the ability to actively manipulate droplets individually as they flow through the microchannel network. Two main technologies have sur-

faced recently that allow the manipulation of these droplets. The first is based upon application of an electric field to produce a force on the drop due to the dielectric contrast between the two liquids. This approach has been shown to work in sorting [Ahn *et al.*, 2006b] and merging droplets [Ahn *et al.*, 2006a; Priest *et al.*, 2006]. The second technique consists of varying the surface tension of the droplets locally, through the use of laser heating, thus creating a thermocapillary induced force on the drop. This forcing has also been shown to produce a net force that can be used to block the formation of drops, carry out simple routing [Baroud *et al.*, 2007a], fuse them, synchronize them, or control their division [Baroud *et al.*, 2007b].

Here, we demonstrate how the combination of microfluidics with optical holographic techniques can be used to extend the possibilities of droplet manipulation. By taking advantage of the contactless nature of optical manipulation, we show how the use of different laser patterns allows the implementation of complex operations, which are not possible using the current electrical forcing methods. Furthermore, the coupling between optical energy and thermocapillarity extends the possibilities of optical manipulation to drop sizes that are not accessible through optical forces alone. We begin by exploring the effect of the shape of the laser focus on the blockage of droplets. Indeed, the ability to vary the shape of the laser beyond a simple Gaussian beam provides an additional degree of freedom which can extend the limits of the technique. Further, we demonstrate three novel implementations which provide conceptually new operations.

4.2 Experimental setup

Holographic beam shaping was employed to generate the desired patterns of light [Burnham *et al.*, 2007]. The Gaussian beam from a 4 W Laser Quantum Finesse laser providing continuous wave 532 nm light was expanded using a Keplerian telescope to entirely fill the short axis (768 pixels) of a Holoeye LCR-2500 spatial light modulator (SLM). Power was controlled with a polarizing beam cube and half wave plate, whilst a second half wave plate rotated the polarization to achieve optimal diffraction efficiency from the SLM. Two 4f imaging systems demagnified the reflected beam such that the SLM was conjugate with the microscope objectives back aperture whilst slightly under-filling the pupil. Two objectives were used over the course of the experiments; the first was a Nikon 10x (NA = 0.25) and the second a Mitutoyo 10x (NA = 0.26) both of which focus the beam into the prefabricated microfluidic channels positioned on a three axis translation stage above the objective. The two objectives, in conjunction with custom built Köhler illumination and appropriate tube lenses, were also used to image the channels onto a Basler A602f firewire camera.

The phase of the beam incident upon the SLM was modified by displaying phase-only holograms whose optical Fourier transform gives the desired intensity pattern in the plane of the microfluidic channel. To produce the holograms we implemented an adaptive-additive algorithm [Soifer *et al.*, 1997], in custom written LabVIEW software, allowing the user to input an arbitrary 8-bit greyscale image of the desired intensity pattern. In addition, aberration correction was combined with the hologram to remove the large amount of astigmatism generated by the SLM.

The microfluidic chips, shown in Fig. 3.1 were fabricated with molded PDMS (Sylgard 184, Dow Corning) using standard soft lithography techniques (SU-8, Microchem) and sealed against a glass microscope slide. The dimensions of the channels ranged from 75 to 200 μm in width and 50 μm in height. Oil (Hexadecane + span80, 2% w/w) and an aqueous solution (water + ink 2% v/v) are pumped into the channel using syringe pumps. Dark blue Parker pen ink was added to the water in order to absorb the 532 nm light. Other absorbing dyes could be used depending on absorption requirements and the laser wavelength used [Baroud *et al.*, 2007a].

4.3 Results

4.3.1 Spatial laser patterns

In order to investigate the effect of different light patterns on drops, we focused on the minimum optical power P_{\min} required to block the advance of a drop, for three different shapes: a Gaussian spot with a 1 μm waist, a straight line aligned with the flow direction, and a straight line perpendicular to the flow direction. Both lines were 2 μm in width and 200 μm in length. In these experiments, the chips had two oil inlets and one of aqueous solution. Droplets size is controlled by the ratio between the first oil flow rate $Q_{\text{oil}}^{(1)}$ and the water flow rate Q_{water} , which are both kept constant. The second oil flow rate $Q_{\text{oil}}^{(2)}$ is used to tune the total flow rate $Q_{\text{tot}} = Q_{\text{oil}}^{(1)} + Q_{\text{oil}}^{(2)} + Q_{\text{water}}$, this way the size of the droplets is kept constant while their velocity varies with Q_{tot} .

The channel geometry forces the drops to reach the patterned laser beam. The first observation is that the water-oil interface adapts to the laser forcing, as seen in Fig. 4.1(a) and (b). When the line is parallel with the direction of flow, the front interface is flattened and the drop stops after advancing through a significant portion of the line. In the case of a line perpendicular to the flow direction, the surface of the drop is even flatter than in the previous case, taking on the shape of the line.

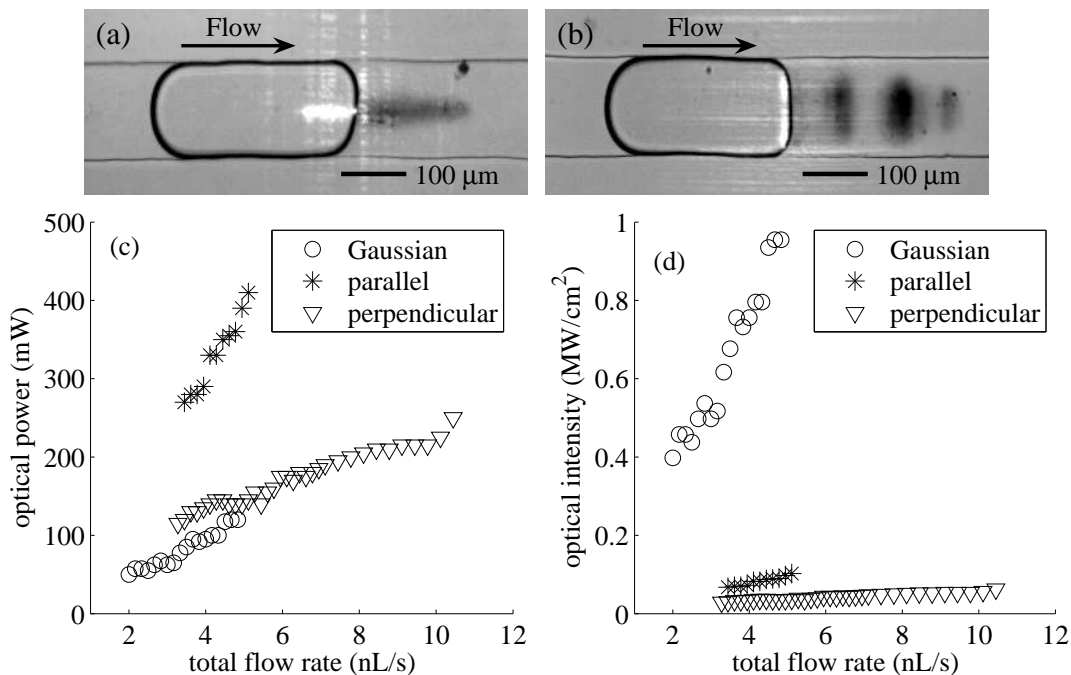


Figure 4.1: Blocking a drop with different laser patterns: (a) Drop blocked by a line parallel to the flow, or (b) a line perpendicular to flow. (c) Minimum laser power required for blocking a drop, as a function of flow rate. (d) Minimum laser intensity required to block droplets.

For each optical pattern used the oil flow rate was varied from $Q_{\text{tot}} \sim 1$ to 11 nL/s in increments of 0.17 nL/s. For each flow rate, we started from a high laser power and reduced it for successive drops, until the minimum power P_{min} that still held the drops was reached. The maximum flow rate studied for each pattern was not limited by the laser no longer blocking the droplets, but rather, boiling of the water.

The minimum laser power for each of the laser distributions is plotted as a function of the total flow rate in Fig. 4.1(c). It scales approximately linearly with the total flowrate but the slopes of the curves and the values of P_{min} differ for the three cases. The use of a line perpendicular to the flow allows the blocking of drops at higher flowrates, up to more than 10 nL/s. Conversely, even though a lower laser power is necessary to hold the droplets in the case of a Gaussian spot, it was not possible to hold droplets for flow rates higher than about 5 nL/s. This was also the case for the line parallel to the flow, where no droplets could be held at flowrates higher than 5 nL/s.

Moreover, if the pattern intensity is studied instead of the total laser power, the minimum intensity I_{min} necessary to block a drop is found to be several times higher for a Gaussian spot than for a line distribution [Fig. 4.1(d)]. The perpendicular line is found to block the drop for the lowest value of I_{min} . Note that in the case of line patterns, the image is only fully formed in the

focal plane of the microscope objective, meaning that it is not a sheet of light. For the Gaussian spot however, the pattern propagates through the whole sample.

4.3.2 Applications

We now consider the applications of such holographic beam shaping and how single spot applications [Baroud *et al.*, 2007a] can be extended. The first application is droplet routing, actively sending droplets into different directions at a trifurcation. This is a precursor of sorting, one of the major applications in microfluidics. Sorting, however, requires some form of active decision making based on fluorescence, size or other observable parameters. Here our droplets are all similar and monodisperse so sorting is not practical. Making use of the ability to both dynamically switch the optical patterns projected into the microfluidic channel and the ability to create extended patterns (in this case four spots) we can deflect droplets through large angles and send them into preferred channels. This is shown using a four way cross channel in Fig. 4.2. Figures 4.2(a)–(c) show the droplets being moved to the left, straight, or to the right, respectively. The switching time of the droplets into a given channel is limited only by the update speed of the SLM, which ranges from 30 to 60 Hz. It would be relatively straightforward to extend this technique to active sorting, by including some video processing and combining it with the hologram switching (the holograms are precalculated and are merely changed based on which direction the droplets need to move in). One could imagine the sorting being based on droplet size, chemical composition, fluorescence measurements or simply the contents of a drop.

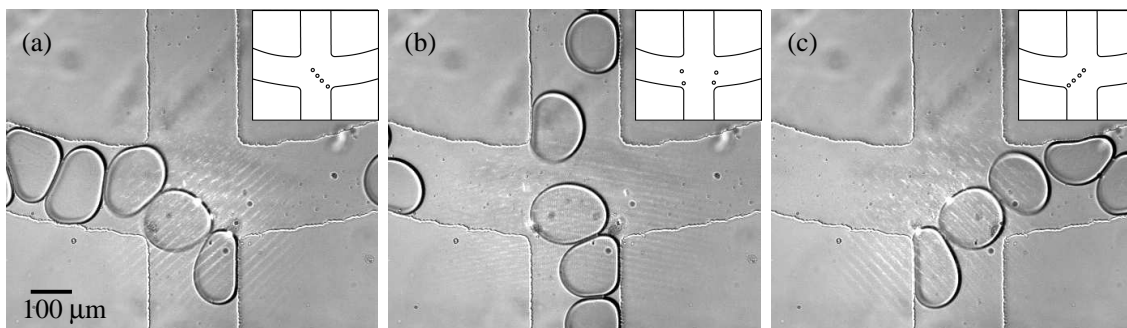


Figure 4.2: Four light spots are aligned to sort droplets into either (a) the left-hand channel, (b) the center channel, or (c) the right channel. The insets show the positions of the holographically generated multiple Gaussian foci within the channel.

The second example uses line patterns to store droplets at a given point in the channel while rerouting other droplets to move past the stored droplet, as shown in Fig. 4.3. The first line

upstream is set to move a droplet into one side of the larger channel. The droplet is then stored by the downstream line further along the channel. The first line is then changed so as to move subsequent droplets in the flow past the first droplet. Thus we can store and could interrogate the first droplet without the need to stop the flow, which is important in order to obtain longer interrogation times. Again, this could be combined with active techniques to choose a droplet based on its characteristics or to facilitate controlled reactions (i.e. fusion [Baroud *et al.*, 2007b]) between droplets.

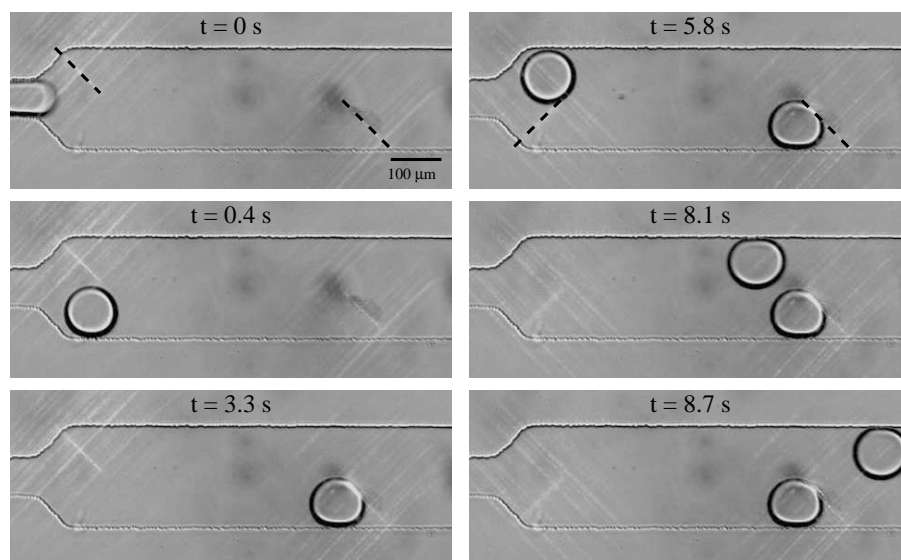


Figure 4.3: Image sequence (left column followed by right column) showing how the drop order can be changed: The initial drop is sent right and held stationary, then successive droplets are sent left. Dashed lines overlay the position of the laser patterns.

The third example, shown in Fig. 4.4, is an extension of the second. Here we are able to trap several droplets at once, first one, then two and finally three using three lines of light. Again this is in the presence of droplets flowing through the channel. We are then able to shuttle the droplets through the pattern, by turning the whole pattern on and off, so the first droplet is lost and the second droplet takes its place and so on. This allows large scale storage and controlled movement of many droplets simultaneously which may be useful for offline analysis of many droplets, droplet re-ordering or droplet “memory” applications.

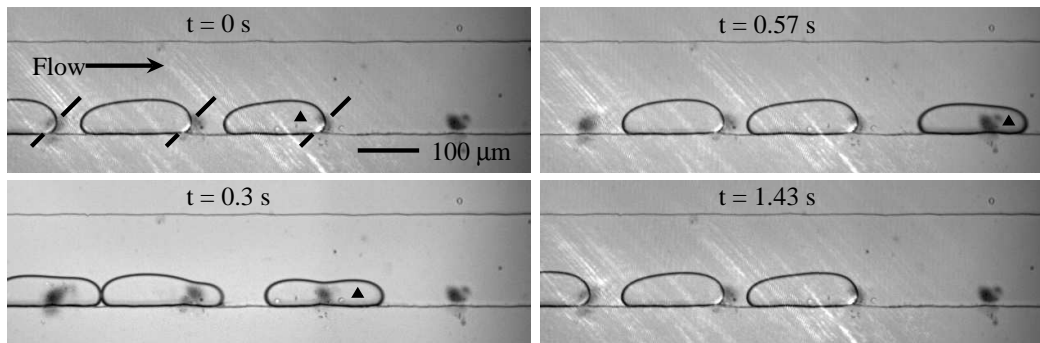


Figure 4.4: A drop treadmill holds up to three droplets and can function as a first-in-first-out buffer memory. The triangle marks the same droplet in the different images (sequenced left column followed by right column), indicating its movement. Dashed lines overlay the position of the laser patterns.

4.4 Conclusions

In conclusion we have shown that making use of holographic beam shaping techniques has a number of advantages over conventional methods of inducing thermocapillary forces in droplets. In addition extended patterns of light allow significant additional functionality over techniques using a single spot. We believe this can lead to enhanced optical control in droplet microfluidics devices. Future extensions of our techniques include droplet sorting and droplet reordering, as well as more advanced studies into the role that extended optical patterns play in the forces induced.

Chapter 5

Mixing via thermocapillary generation of flow patterns inside a microfluidic drop

Article appeared in *New Journal of Physics*, **11**, 075033, (2009).

5.1 Introduction

The use of droplets was shown, early on, to solve two major problems encountered in microfluidic devices: that of controlling the dispersion of the species, by forcing the chemicals to remain in the drop, and the problem of mixing in the absence of turbulence [Song *et al.*, 2003]. Another important advantage of using droplets lies in the ability to readily integrate external manipulation schemes to directly manipulate the liquid, something difficult to achieve with bulk fluid flow. Along these lines, several manipulation tools have been developed whose action is based on using the physical contrasts between the droplet fluid and the surrounding carrier fluid. These techniques have been used to implement fundamental operations on the drops, such as sorting or merging them, either through the contrast of dielectric constant (dielectrophoresis) [Chabert *et al.*, 2005; Ahn *et al.*, 2006b], refractive index [Lorenz *et al.*, 2007] or through the manipulation of surface tension by local heating [Baroud *et al.*, 2007a,b].

While most of the above techniques induce recirculation flows within the drop that is being manipulated, previous work has been limited to the study of the net effect on the drop as a whole, rather than on the control of the flow within it. This contrasts with the attention given to mixing in drops as they travel in specially designed channels [Song *et al.*, 2003; Stone & Stone, 2005; Liao *et al.*, 2005], in suspension outside a microchannel [Ward & Homsy, 2001; Grigoriev *et al.*, 2006], or on a solid substrate [Darhuber & Troian, 2005]. In all of the above cases, chaotic

trajectories are obtained inside the drop by combining periodic variations in the recirculation pattern with a mean motion of the drop as a whole. This mean motion was shown to play a major role in breaking the time reversal symmetry for a particle path, making sure that particles do not return to their initial position at the end of each cycle of the periodic forcing.

Indeed, the main approach to mixing in the absence of turbulence has been to flow fluid particles through chaotic trajectories which are highly sensitive to their initial position [Aref, 1984]. In this way, two particles that are initially close together will separate exponentially, leading to the mixing of particles from different regions of the fluid. This mixing method is not limited to microfluidics; it has been developed in the general case of viscous flows and can be produced through a range of forcing methods and in different geometries [Ottino, 1989]. In this approach, the aim is to produce a “stretching and folding” flow, first using the laminar shear flow produced in a viscous fluid (e.g. recirculation rolls inside the translating drops or Poiseuille flow) to separate adjacent particles through a stretching field, then modifying the direction of the flow to reduce the distance over which diffusion takes place (“folding”). In practical situations, the mixing obtained by these mechanisms is enhanced by molecular diffusion and by Taylor-Aris dispersion.

Here we demonstrate that such chaotic flows may be produced in a drop that is held stationary by a focused laser. The mixing properties of the flows created by two different laser configurations are compared: The first configuration uses galvanometric mirrors to produce a time varying laser pattern that produces a non stationary flow field. The second configuration uses holographic techniques like those used in Chapter 4 to produce a stationary laser pattern consisting of two Gaussian spots. In this way, the stationary flow obtained is due to the superposition of the velocity fields associated with each of the hot regions. The mean value of the non stationary flow is similar to the holographically obtained flow. In both cases, the thermocapillary forcing produces the necessary hyperbolic fixed points that lead to the stretching of fluid particles [Solomon & Gollub, 1988; Voth *et al.*, 2002]. However, efficient mixing is only obtained in the time dependent case which breaks the left-right symmetry inside the drop, while the mean recirculation, which does not change sign, breaks the time reversal symmetry. By contrast, the use of stationary patterns is not sufficient to break the barriers to transport and therefore leads to poor mixing, even though the mean flow given by the switching pattern is the same as the flow given by the stationary pattern.

The two experimental setups used in this study are described in Section 5.2. Section 5.3 presents the important temporal and spatial scales that must be considered for the problem. The flow fields obtained with each of the laser setups are shown in Section 5.4, followed by the

experimental results on mixing which are explained and discussed in Section 5.5.

5.2 Experimental Setups

Two different optical setups are used in this work. The first one, sketched in Fig. 5.1(a), is mounted on an inverted microscope (Nikon TE2000) which is equipped with epi-fluorescent illumination (Exfo X-Cite 120). An infrared laser beam (Fitel Furukawa FOL1425) of wavelength 1480 nm is reflected by a pair of galvanometric mirrors (Cambridge Technologies 6210H) which control the laser position inside the microchannel. The angular position of each mirror can be controlled in real time with custom made LabVIEW software (National Instruments), allowing us to create non stationary laser patterns by letting the laser beam alternate between two positions separated by a distance D . The distance between the spots can be controlled with sub-micron resolution and the shifting frequency can be up to 1 kHz. After the galvanometric mirrors, the beam passes through a telescope which consist of an achromatic doublet (Thorlabs, 150 mm focal length) and a convex lens (Thorlabs, 150 mm focal length), both adequate for infrared optics. Then, the laser beam is reflected into the rear aperture of the microscope objective (Nikon Plan Fluor 20X/0.5NA) through a dichroic mirror (OCTAX) and focused inside the microchannel to a $5.3 \mu\text{m}$ waist. To ensure that the laser is focused at the same plane as visible light, the distance of the telescope is adjusted by moving the achromatic doublet to obtain a slightly diverging beam. Images are recorded with a fast camera (Photron Fastcam 1024 PCI) at frame rates ranging from 250 to 3000 fps.

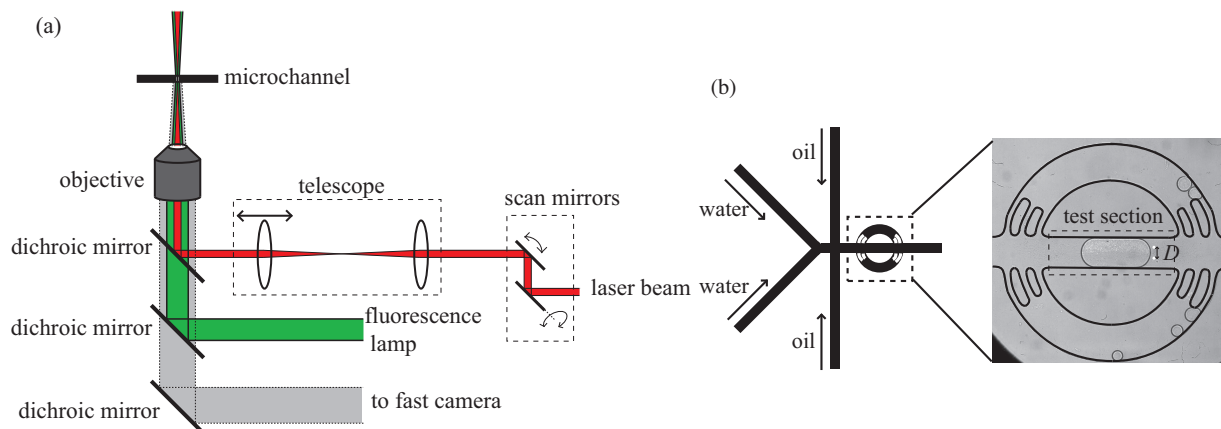


Figure 5.1: (a) Optical setup with galvanometric mirrors. (b) Microchannel geometry.

In the second setup, detailed in Chapter 4, a 532 nm laser beam is expanded using a telescope to entirely fill the short axis of a spatial light modulator (SLM) (Holoeye LCR-2500) which

allows us to holographically shape the laser beam into two stationary Gaussian spots separated by a distance D . Power is controlled using a polarizing beam cube and $\lambda/2$ plate. Two 4f imaging systems demagnify the reflected beam into the back aperture of the objective (Nikon 10X/0.25NA), which focus the beam into the microchannel. Images of the channel are obtained with a firewire camera (Basler A602f) at 240 fps. Kinofoms are generated using a weighted Gerchberg-Saxton algorithm [DiLeonardo *et al.*, 2007], implemented in LabVIEW, to optimise the power uniformity of the spots.

The microfluidic devices are fabricated on PDMS following standard procedures [Xia & Whitesides, 1998] and sealed against a glass slide. The microchannels [Fig. 5.1(b)] are $50\ \mu\text{m}$ in height and $200\ \mu\text{m}$ wide. Two independent water inlets merge before the intersection with two oil inlets, where water drops are formed by flow focusing. Liquids are injected using syringe pumps at constant flow rates of $0.04\ \mu\text{L}/\text{min}$ for water and $0.125\ \mu\text{L}/\text{min}$ for oil. Part of the channel is designed to force the drops into a straight test section where they are blocked by the laser, while allowing the oil to bypass the test section through two symmetric secondary channels. At high enough laser power, one drop is blocked until the next drop enters the test section. Therefore, the time duration of the experiments is determined by the frequency of drop formation, which is approximately 1 Hz.

A 50% w/w paraffin oil-hexadecane mixture is used as the outer phase. A surfactant, Span 80 (Sigma-Aldrich), is added to the oil phase at a concentration of 2% w/w. When the holographic setup is used, 2% w/w ink (Dark blue Parker ink) is mixed with the water to increase the absorption of the 532 nm laser beam and therefore heat the water. With the infrared laser this is not necessary due to the higher absorption coefficient of the water at the 1480 nm wavelength.

Micrometer sized particles are added to the water to be used as tracers. For the first optical setup, green-yellow fluorescent beads (Molecular Probes, $1\ \mu\text{m}$ diameter), at a concentration of 1500 beads per μL , were used to perform PIV measurements with the use of a commercial software (DaVis, LaVision). These beads yielded images with bright particles in a dark background. For the holographic setup, $4\ \mu\text{m}$ diameter nylon beads were suspended in water, with the aid of surfactant [TX100 (Sigma-Aldrich) at a concentration of $5 \cdot 10^{-3}\%$ w/w, ie. about 0.5 times the critical micelle concentration], to visualize the flows in the absence of fluorescence equipment. These beads appear as dark spots on a light background. In both cases the images correspond to an average over the vertical dimension because the depth of field of the optics used here are comparable to the channel depth. The nature of the flow is three-dimensional, but the large width to height ratio allows us to assume a parabolic profile, to leading order, in the vertical direction.

In order to quantify mixing efficiency tracers are added to only one of the water inlets and

then detected using image analysis. Alternatively, china ink was added to one of the water inlets, in the absence of tracer particles, to visualize the mixing of the droplet contents, using the first optical setup.

5.3 Temporal and spatial characteristic dimensions

The physics of thermocapillary manipulation and transport involves several spatial and temporal scales and it is useful to recall their values in the case of the present experiments. The efficiency of the mixing will depend on a comparison between the frequency at which the forcing is alternated and the distance between the laser spots with the characteristic scales of the problem.

5.3.1 Spatial scales

We recall here the main features of the thermocapillary flow field inside a drop that is held by the laser heating (see Fig. 5.2). A pair of steady counter rotating recirculation rolls appears inside the drop, as shown in Chapter 3. The flow at the interface is directed towards the laser position, thus indicating an increase of the surface tension at that location. A separatrix surface separates the rolls and defines two main regions inside the drop on either side of the stagnation points, which remain unmixed, since no streamlines cross the separatrix.

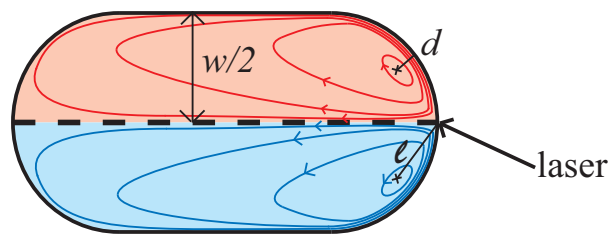


Figure 5.2: Sketch of the thermocapillary flow pattern inside a drop held by a laser centered in the test channel. The separatrix (dashed line) divides the drop into two regions, corresponding to two counter rotating rolls.

The two inherent spatial scales in the experiments are given by the channel depth and width. The depth can be considered as determining the distance between the edge of the drop and the center of the recirculation rolls (d), while the channel width provides the distance $w/2$ over which a particle must travel to cross from one region of the drop to another.

In the case of opto-thermal forcing, a thermal length scale around each of the spots must be taken into account. Indeed, it was measured in Chapter 2 that the width of the thermal gradient,

$\sigma \simeq 20 \mu\text{m}$, is larger than the laser waist. As a consequence, the distance D between the two laser spots must be larger than 2σ in order to obtain two well defined temperature peaks in the case of a stationary pattern. If this is the case, the resulting flow is the superposition of the flows due to each of the temperature fields, owing to the linearity of the Stokes flow. Conversely, if $D < 2\sigma$, the temperature field resembles a single wider hot spot at the front of the drop and the flow field will be similar to the field obtained with a single centered spot.

5.3.2 Time scales

The first time scale to consider is due to the viscous diffusion which determines the time necessary for the motion of the interface to be felt at a distance ℓ away. Using the distance between the laser position and the center of the recirculation rolls $\ell \simeq 20 \mu\text{m}$ (see Chapter 3) as the characteristic length and taking the kinematic viscosity of water $\nu = 10^{-6} \text{ m}^2/\text{s}$, we find $\tau_{\text{visc}} = \ell^2/\nu = 0.4 \text{ ms}$. This is the time to propagate the information about the interface motion into the droplet, which will instantaneously lead to recirculating motion by continuity of flow inside the drop, owing to the incompressibility of water.

The second temporal scale is related to the heating of the fluid by the laser. If we assume that the surface tension adjusts immediately to the local value of temperature, the important time scale for creating the thermocapillary motion is due to the time required to produce the thermal gradient, as explained in Chapter 3. This time is determined by the channel depth and by the thermal properties of the fluids and the channel walls but is independent of the laser power. For the current geometry and fluids, we estimate the heating time scale at $\tau_{\text{th}} \simeq 6 \text{ ms}$.

A third time scale is associated with the transport of fluid particles by the thermocapillary flow. It can be extracted from the characteristic velocity of the interface $v_{\text{int}} \simeq 1 \text{ mm/s}$ and from the half width of the drop $w/2 = 100 \mu\text{m}$. This advection time $\tau_{\text{adv}} = 100 \text{ ms}$ represents the time required for a fluid particle to cross between the two regions inside the drop.

The above time scales are well separated with $\tau_{\text{visc}} \ll \tau_{\text{th}} \ll \tau_{\text{adv}}$. Comparing the first two suggests that the limiting time for the fluid to react to the laser is determined by the heating time, i.e. that the thermocapillary flow is established simultaneously with the thermal gradient. Moreover, if the forcing half-period $\tau_{\text{laser}} \ll \tau_{\text{th}}$, the fluid does not have time to cool down between two heating cycles and one expects a stationary convection pattern inside the drop. If on the other hand $\tau_{\text{laser}} \gg \tau_{\text{th}}$, then two independent flow fields are established in an alternating manner simultaneously with the laser switching. In the intermediate range, where $\tau_{\text{laser}} \sim \tau_{\text{th}}$, peaks of temperature periodically occur at the laser positions, forcing the flow in one direction or the other, depending on the strength of the surface tension gradient in each laser position. Finally,

τ_{laser} must be larger than τ_{adv} for the mixing to be efficient. If $\tau_{\text{laser}} \ll \tau_{\text{adv}}$, one expects that the flow is too slow to transport particles across the median line and mix them.

5.4 Flow Fields

When a drop is blocked by a single centered laser beam, the flow inside the drop presents a mirror symmetry. The symmetry of this flow is broken when the laser beam is placed at an off-center position, in which case the two recirculation rolls are twisted with respect to the center plane, as shown in Fig. 5.3(a) with the aid of fluorescent beads. Towards the rear of the drop the rolls tend to realign parallel to the microchannel, due to the confinement caused by the presence of the channel walls. The velocity field (obtained by PIV) associated with this flow is shown in Fig. 5.4(a).

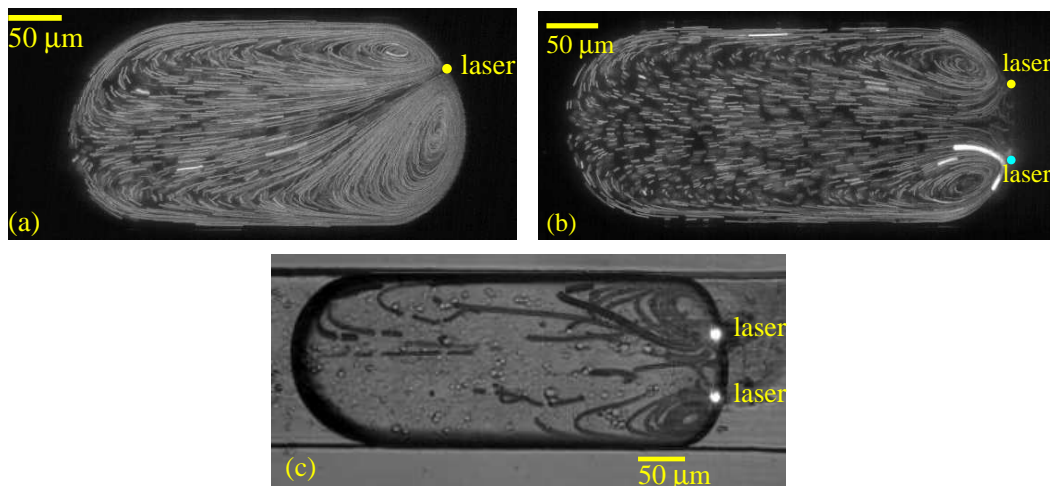


Figure 5.3: Visualization of the flow fields with tracers in three cases: (a) One off-center laser spot, (b) one rapidly alternating off-center spot (1000 Hz) and (c) two stationary off-center spots.

The flow field obtained with a laser spot that alternates between two symmetric off-center positions, depends on the shifting frequency. If the time during which the laser remains in each position $\tau_{\text{laser}} > \tau_{\text{th}}$, a thermal gradient is created alternatively at each of the laser positions, therefore inducing two alternating, asymmetric pairs of recirculation rolls. Neglecting transient effects, whose duration is of the order of the viscous timescale τ_{visc} , the flow switches between the one shown in Fig. 5.3(a) and its mirror image with respect to the mid-plane of the drop with half period τ_{laser} .

If $\tau_{\text{laser}} \ll \tau_{\text{th}}$, a steady thermal gradient is induced by the laser at both positions and a steady

thermocapillary flow is created. This flow is shown in Fig. 5.3(b) with the aid of fluorescent tracers. Its corresponding velocity field is shown in Fig. 5.4(b). The same flow pattern is obtained when a holographically obtained pair of symmetric stationary laser spots is used, as shown in Fig. 5.3(c). The flow in these cases recalls the pattern obtained in the presence of one centered laser beam which consists of two large symmetric recirculation rolls that fill the drop. An important difference, however, consists in the presence of two small counter rotating inner rolls between the laser spots near the front interface, which appear because the thermocapillary flow is directed towards each one of the hot spots.

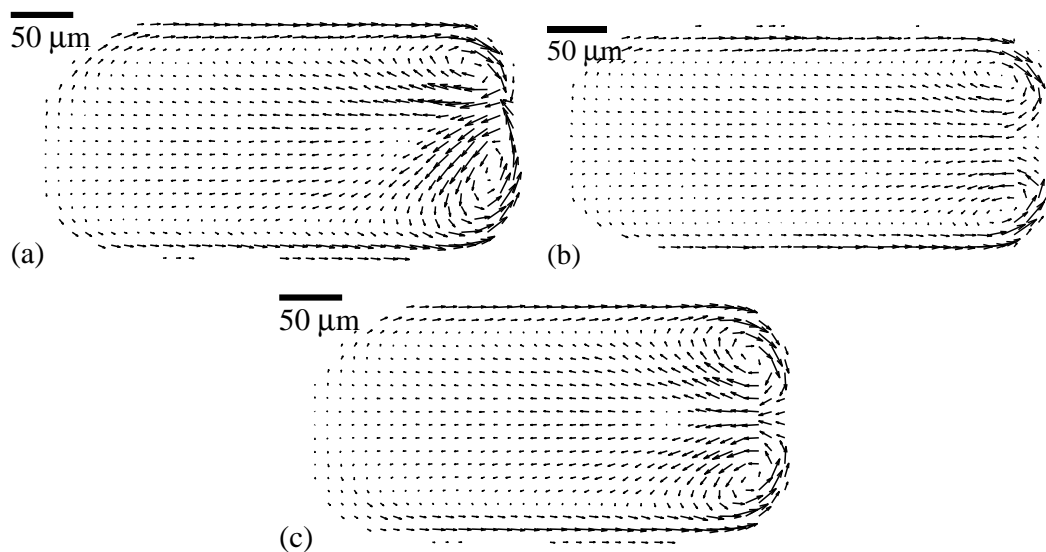


Figure 5.4: Velocity fields obtained with (a) one off-center laser beam, (b) two rapidly alternating laser spots and (c) the superimposition of the first velocity field and its mirror image with respect to the center plane of the drop.

The Stokes nature of the flows allows us to reproduce the velocity field in the presence of two stationary symmetric (or rapidly alternating) laser spots by superimposing the velocity field obtained with one off-center laser spot and its horizontal reflection. The resulting velocity field is shown in Fig. 5.4(c), showing good qualitative agreement with the observed pattern [Fig. 5.4(b)]. The small inner rolls, however, cannot be reproduced because the spatial resolution of the PIV measurements is comparable with the size of these small rolls.

5.5 Mixing

5.5.1 Mixing measurements

When tracer particles are added to one of the water inlets two well separated regions can be distinguished within drops arriving to the test section: one region containing the beads and the other almost without any (some beads are present in the other half of the drop due to fluctuations during the drop formation). As expected, no mixing occurs when the drop is blocked by a single, centered laser beam, and beads remain in the upper half of the drop [Fig. 5.5(a)].

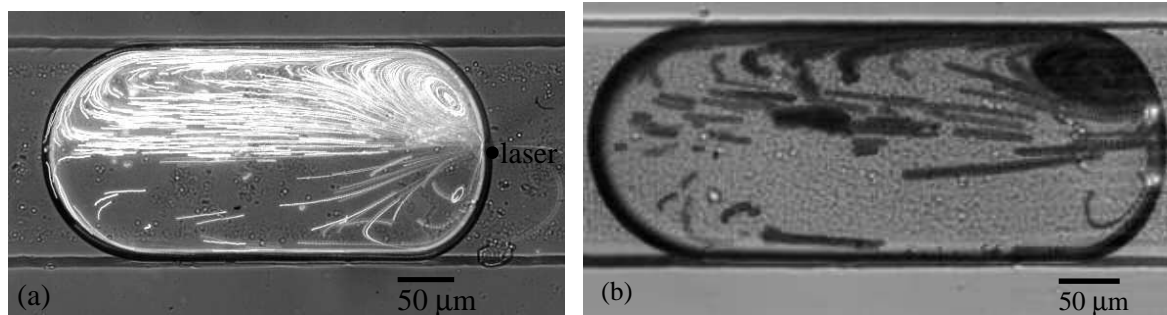


Figure 5.5: No mixing situation, shown by tracers contained in the upper half of a drop blocked by a centered laser beam (a) or by a pair of two symmetric stationary laser spots (b).

In order to measure the mixing efficiency of the flows induced inside the drop by the different laser patterns, the number of beads in each region, $N_{\text{top,bottom}}$, is found as a function of time while the drop is held in the test section. Figures 5.6(a) and (b) show the cases of two stationary laser spots separated by a distance $D = 16 \mu\text{m}$ and $D = 86 \mu\text{m}$, respectively. N_{top} and N_{bottom} remain constant, showing that no mixing occurs. In the first case, the laser spots are close together, so the flow field is similar to the one produced by a single, centered laser beam, as in Fig. 5.5(a). For the case of two separated, symmetric laser beams, no mixing occurs either. In fact, the symmetry of the flow field is maintained here, for any value of D , and a symmetry plane divides the drop in two, keeping the two halves of the drop well separated. This can be observed with the aid of tracers, as shown in Fig. 5.5(b).

We repeat the experiment using two alternating laser spots separated by $D = 17 \mu\text{m}$ and $D = 89 \mu\text{m}$ and with forcing time $\tau_{\text{laser}} = 200 \text{ ms}$. The number of particles in each half of the drop is shown in Figs. 5.7(a) and (b). Again, poor mixing occurs in the first case due to the proximity of the two laser spots, which induce a flow field similar to the one obtained with only one centered laser spot. The use of two beams separated by a larger distance [Fig. 5.7(b)], on the contrary, forces particles to cross the mid plane of the drop, and N_{bottom} decreases progressively

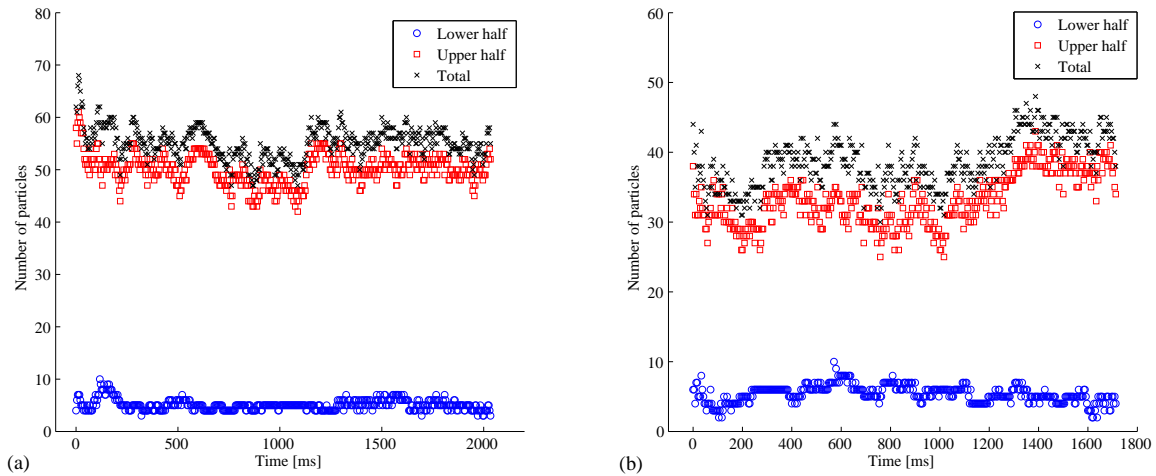


Figure 5.6: Number of tracers in the upper and lower half of the drop as a function of time, while the drop is blocked by two stationary laser beams separated by a distance of $16 \mu\text{m}$ (a) or $86 \mu\text{m}$ (b).

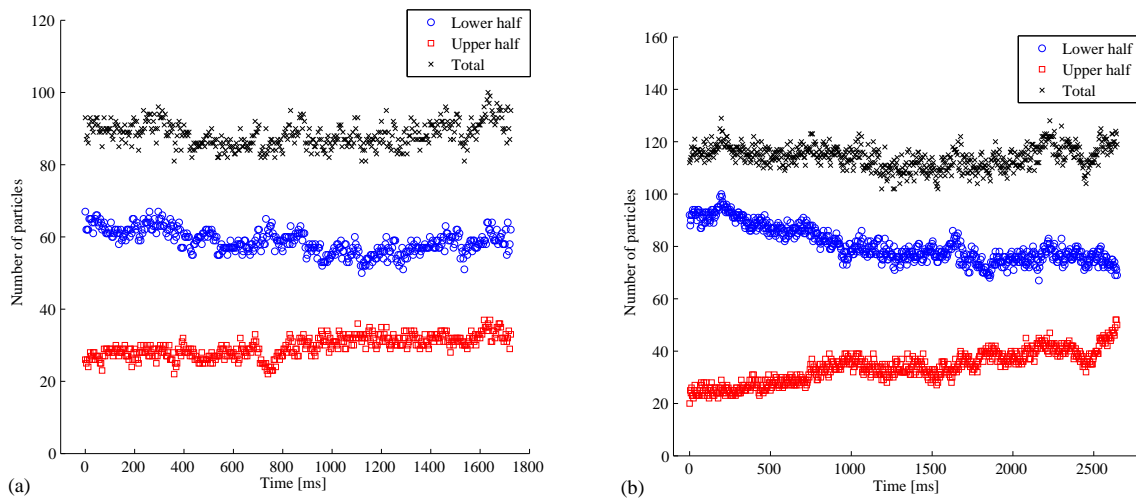


Figure 5.7: Number of tracers in the upper and lower half of the drop as a function of time, while the drop is blocked by two alternating laser beams separated by a distance of $17 \mu\text{m}$ (a) or $89 \mu\text{m}$ (b). In both cases $\tau_{\text{laser}} = 200 \text{ ms}$.

as a function of time, while N_{top} increases. After 2.5 s the fraction of particles in each region becomes similar, showing the existence of mixing in this case. Indeed, a necessary condition for mixing is that the number of tracers become equal in both halves of the drop. This is not a sufficient statement of mixing, since it does not ensure the homogeneity within the drop, but once the drop is released from the laser, the recirculation flow associated with the mean motion of the drop can act to mix each of the two halves in the longitudinal direction.

5.5.2 Mixing efficiency extracted from PIV measurements

From the last section we observe that the flow field obtained with non stationary laser patterns can be used to mix the contents of a microdroplet. In fact, divergent trajectories can appear due to the non stationary flow field, as shown in Fig. 5.8. Here, the velocity field is measured for the case of a laser beam located at a distance $D/2 = 51 \mu\text{m}$ with respect to the center of the channel. This is then used to numerically simulate the transport of five imaginary passive tracers. The velocity field is periodically reflected to simulate the switching between the two laser positions, with half period $\tau_{\text{laser}} = 100 \text{ ms}$.

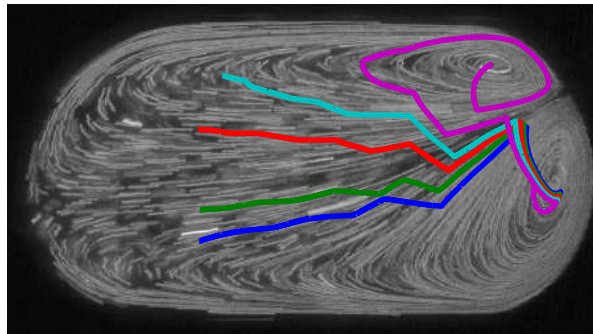


Figure 5.8: Divergent particle trajectories numerically obtained from PIV measurements.

At $t = 0$ the five particles start aligned within a $5 \mu\text{m}$ region in the lower part of the drop, near the center of the lower recirculation roll. If the laser position was stationary, one would expect the five particles to remain circulating around the roll center. When the laser alternates between two positions, the switching of the flow field advects the particles far towards the rear of the drop. Moreover, after five periods they finish at distant positions, three of them in the upper half and two in the lower half of the drop. This flow is reminiscent of the “blinking vortex” flow which has been shown to produce chaotic mixing [Aref, 1984].

Next, the mixing efficiency is studied as a function of the two parameters of the problem: the distance between the laser spots D and the forcing time τ_{laser} . For this, the trajectory of a few

thousand of passive tracers is calculated as a function of time $T = t/\tau_{\text{laser}}$ between $T = 0$ and $T = 10$, for different values of D and τ_{laser} . Figure 5.9 shows the position of the tracers after different multiples of the half period T for $D = 102 \mu\text{m}$ and $\tau_{\text{laser}} = 100 \text{ ms}$. Particles starting in the lower half of the drop at $T = 0$ are shown in blue, and particles starting in the upper half are represented in red. As the laser alternates between both positions, “fingers” of particles cross the mid-plane, penetrating into the opposite half of the drop. These fingers are stretched and advected towards the rear of the drop.

Mixing is quantified by measuring the fraction of particles that cross the mid-plane of the drop, ϕ , as a function of time. $\phi(T)$ is shown in Fig. 5.10(a) for $D = 102 \mu\text{m}$ and different values of τ_{laser} . The first half period shows a transient behavior during which many particles cross the mid-plane. This is followed by a linear trend of particle crossings which exhibits periodic peaks of ϕ at the end of each half cycle.

A mixing rate is extracted from the linear trend as the slope of $\phi(t)$ for $t > \tau_{\text{laser}}$, as shown in Fig. 5.10(b) as a function of D and τ_{laser} . For low values of τ_{laser} the mixing is slow, regardless of D , since τ_{laser} is small compared with τ_{adv} and particles do not have time to cross the mid-plane. As τ_{laser} increases, the mixing rate increases, reaching a maximum and then decreasing again slightly. This recalls previous observations of resonant behaviour where the forcing time must match an inherent time scale of the system. A global maximum is found for $D = 85 \mu\text{m}$ and $\tau_{\text{laser}} = 200 \text{ ms}$.

5.5.3 Mixing of dye

The above results show the mixing of discrete particles within a droplet. Next, we focus on the mixing of dye molecules by adding ink to the lower water inlet. In this way the drops contain two well separated regions: a dark half and a clear half, as shown by the first image of Fig. 5.11, which shows a drop being blocked by two laser spots separated by a distance $D = 85 \mu\text{m}$ that alternate with half period $\tau_{\text{laser}} = 100 \text{ ms}$. A similar behaviour to what is shown in Fig. 5.9 can be observed, with waves of clear and dark liquid being stretched and ejected away from the laser positions.

Figure 5.11 shows the gray scale difference between the $T = 0$ image and snapshots of the drop after each half-period. Red (bright) regions represent clear water waves entering the darker region and blue, or dark, areas correspond to dark fluid that enters into the clear water. At later T the upper half of the drop becomes darker and the lower half becomes brighter. Similarly to Fig. 5.9, the mixed zone is situated next to the laser spots and expands towards the rear of the drop.

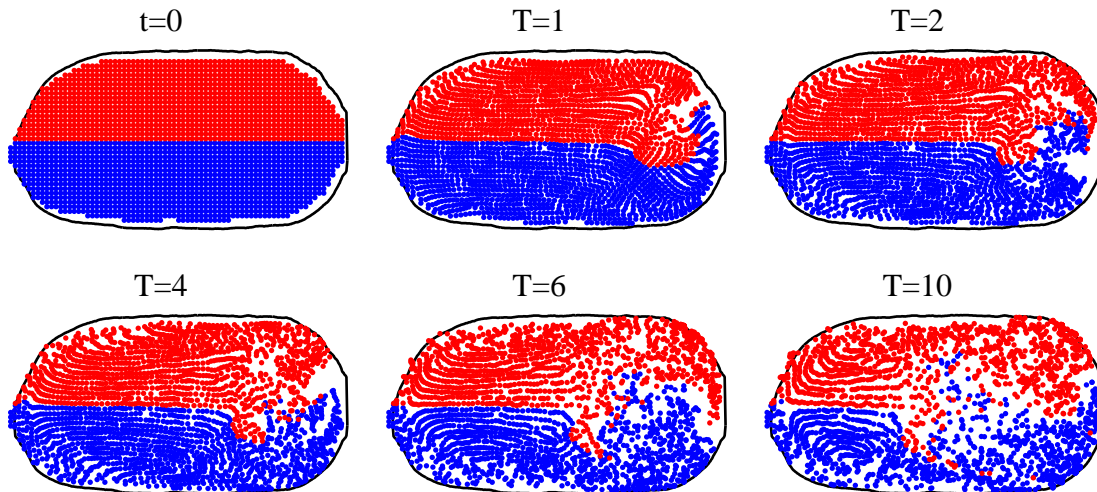


Figure 5.9: Snapshots of the position of passive tracers as a function of time. Blue (red) spots represent particles placed in the lower (upper) part of the drop at $t = 0$. $D = 102 \mu\text{m}$ and $\tau_{\text{laser}} = 100 \text{ ms}$.

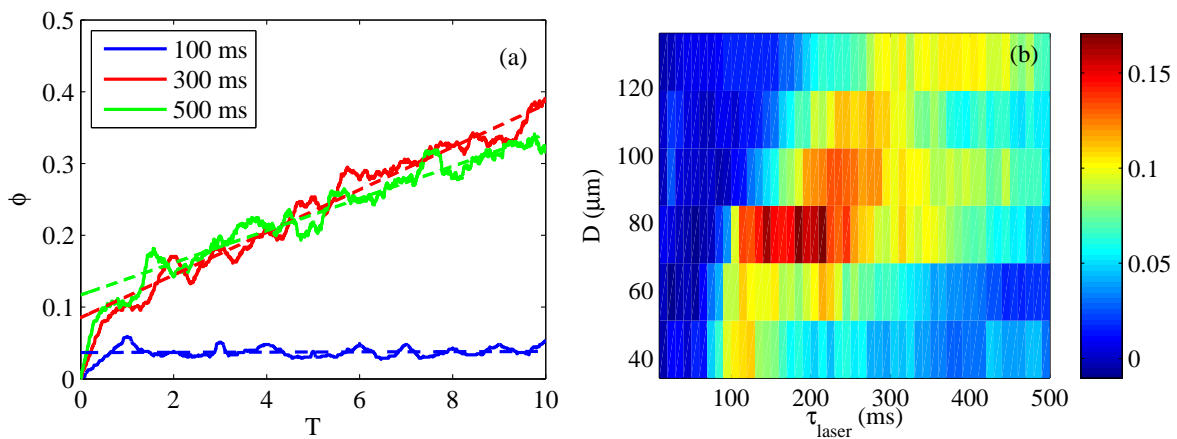


Figure 5.10: (a) Fraction of particles that cross the mid-plane of the drop as a function of time (solid line), and linear fit (dashed line), for $D = 105 \mu\text{m}$ and different values of τ_{laser} . (b) Mixing rate as a function of the distance between the laser spots D and the forcing time τ_{laser} . The scale bar is in units of s^{-1} .

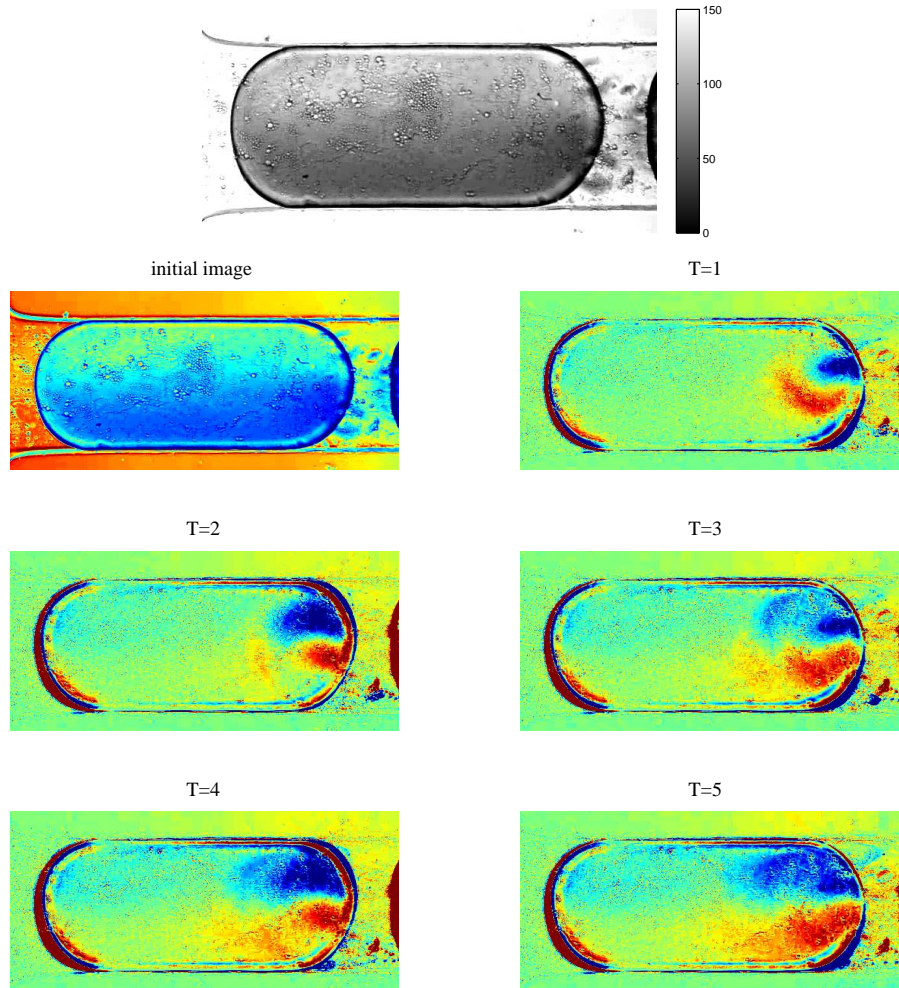


Figure 5.11: Mixing of ink which is initially present in the lower half of the drop. The first image corresponds to $t = 0$. The consecutive images represent the difference between instantaneous measurements of light intensity and the initial image. Blue means darker while red means a brighter gray level. After each half cycle, ink is transported from the lower to upper half while clear water is transported from the top half to lower half. The values of the parameters are $\tau_{\text{laser}} = 100$ ms and $D = 85$ μm .

5.6 Discussion

The mixing inside microdrops hinges on the concurrent breaking of several symmetries in the flow field [Grigoriev *et al.*, 2006]. In the particular case of the confined microchannel geometry, previous work has achieved this by periodically rotating the direction of recirculation rolls with respect to the drop contents, namely by flowing the droplets through a serpentine microchannel [Song *et al.*, 2003; Stone & Stone, 2005]. By the same token, the time reversal symmetry is also broken by the mean motion of the drop. In the case of a drop that is held stationary by thermocapillary action, the time reversal symmetry is broken by the recirculation rolls that are produced by the laser heating.

Moreover, we show above that mixing does not occur if the forcing is symmetric with respect to the channel width, for example by using holographic patterns that produce a symmetric flow. Even an asymmetric stationary heating pattern would produce poor mixing because of the presence of a separatrix plane, connecting the two stagnation points, and separating the two regions within the drop. This curved surface, which lies between the two recirculation rolls, forms a barrier to transport that cannot be crossed by fluid particles. Good mixing is therefore only achieved when this separatrix is modulated, for example by switching between a given forcing pattern and its mirror image to imitate the rotation that has been explored in previous studies.

The mixing efficiency is a complicated function of the forcing parameters, with maximum efficiency occurring for a range of switching frequencies and separations between the forcing points. The presence of this maximum is in agreement with previous results that find resonance conditions for which the mixing is either improved or worsened [Okkels & Tabeling, 2004; Chabreyrie *et al.*, 2008]. Although we do not quantify the total quality of the mixing in our drops, the dye experiments show a quasi-total homogenization of the gray levels between the moment that the drop enters and when it exits. Indeed, the dye experiments show that the mixing is further aided by three-dimensional effects and molecular diffusion which are not accounted for in the numerical study, meaning that the results obtained from Figs. 5.9 and 5.10 are conservative estimates of the true mixing inside the droplets. Three-dimensional effects enhance the mixing in two ways: First, the streamlines in the calculations cannot cross since the calculated field is two dimensional. This is not true in a three-dimensional flow field where flow lines do cross at a given projected location but at different heights in the channel. This enhances the mixing by the diffusion of species across flow lines. Second, Taylor-Aris dispersion further acts to enhance the mixing, as seen in the dye mixing experiment. These three-dimensional effects depend on the diffusion coefficients of the species and should be included in further studies of the mixing.

In the context of droplet microfluidics, the results obtained above are slow when compared

with the rates obtained by flowing drops in serpentine channels. For this reason, this approach is not a replacement for passive control of droplets but should be considered as a complementary tool which offers additional modularity. It can be applied at any channel location, which makes it useful for multiple step mixing in order to re-homogenize flowing droplets. Furthermore, the ability to modify the forcing frequency and amplitude can lead to optimized control taking into account the drop size, the fluid viscosities, or the diffusion coefficients. Most importantly, these results demonstrate that the laser manipulation tool can serve not only to provide control of the droplet as a whole but also to implement fine control of the flow within it. As such, it forecasts new possibilities in droplet microfluidics and their applications. For example, this approach can provide a way to combine controlled mixing with thermal control, for instance in situations where a chemical reaction is inhibited or enhanced by the heating.

5.6.1 Heating of the drop contents

The heating is inherently present in the laser manipulation and may constitute an advantage in applications where heat can be used as a catalyst. However, it may also be a disadvantage in situations where high temperatures can damage the drop contents. In any case, heating is a key point to be taken into account for practical applications involving laser manipulation. For that reason, it is important to estimate and characterize the heating to which the fluid inside the drop is subjected. Indeed, the laser heating is highly localized at the front of the drop, but through the recirculation flow inside the drop a large volume of fluid may be exposed to the heating.

Here, we estimate this heating by using the measured flow field inside the drops presented here and the measured thermal field presented in Chapter 2. The velocity field of the Marangoni flow produced by a single, centered laser beam is used to simulate the trajectory of four imaginary passive tracers inside the drop, which travel in closed paths around the center of the recirculation rolls [Fig. 5.12(a)].

The steady temperature field presented in Chapter 2, which corresponds to a Lorentzian profile centered at the laser position, is used to calculate the temperature increase experienced by the fluid particles during their trajectory. As shown in Fig. 5.12(b), particles that travel in the outermost trajectories are exposed to a larger temperature increase, in a cycle with long associated period due to the slow velocities of the flow far from the front of the drop. On the contrary, fluid particles that travel in trajectories near the center of the roll experience a significantly lower temperature increase, but with shorter associated period.

These results show that most of the fluid inside the drop remains unheated. Statistically, only a small fraction of the fluid is exposed to high temperatures, which is encouraging for

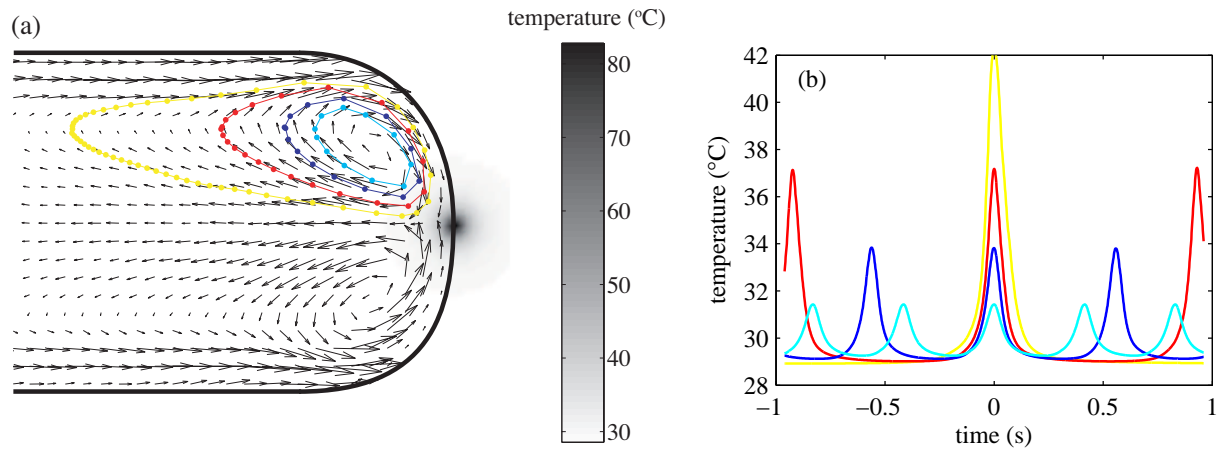


Figure 5.12: (a) Trajectory of four different fluid particles inside a drop held by a single, centered laser beam. The underlying gray scale field represents the temperature field. (b) Evolution of the temperature of the fluid particles during their trajectories.

applications of the laser forcing with drops that carry sensitive material such as cells. The picture, however, may be complicated in the mixing experiments through the utilization of an alternating laser forcing, since in that case the possibilities for a bulk fluid particle to pass near the laser position are increased. This can be exploited in applications where heating the drop contents is convenient and the heating of the drop material can be estimated again by considering both the alternating flow due to a switching of the laser position and an alternating temperature field centered at each laser position

Chapter 6

Formation of drops by laser forcing in a co-flowing geometry

6.1 Introduction

Active control of drops in microfluidics concerns not only their trajectory, but also, and not less importantly, their formation. Although there exist a few examples on microfluidic components to produce drops on demand based on application of high voltage [He *et al.*, 2005] or temperature [Prakash & Gershenfeld, 2007] pulses, most methods are based on hydrodynamic forcing to produce droplets in a passive way. The most common devices used in microfluidics for drop production are the T-junction [Thorsen *et al.*, 2001], flow focusing [Anna *et al.*, 2003] and co-flowing devices [Gañán-Calvo & Gordillo, 2001].

The dynamics of drop formation has been studied in more or less detail for the three geometries mentioned above. Generally speaking, drop breakup mechanisms are ruled by the competition between viscous, capillary and inertial forces [Garstecki *et al.*, 2005*b*], and exhibit different behaviour depending on the value of the Reynolds (Re), capillary (Ca) and Weber (We) numbers.

While drop break up processes lead to highly monodisperse emulsions in the capillary (low Re and low Ca) and in the inertia (high Re and high We) dominated regimes, non steady drop formation and even chaotic and non linear behaviour are observed when capillary and viscous effects are in competition [Garstecki *et al.*, 2005*a*]. In fact, drop formation process in this case seems to be related to Rayleigh-Plateau like instability, and polydispersity reflects the existence of a broad range of unstable perturbations.

Recently, drop formation in this regime has been object of big attention in a co-flowing geometry [Gañán-Calvo & Gordillo, 2001; Guillot *et al.*, 2007; Utada *et al.*, 2007]. In this

geometry, the regime at intermediate and high Ca is characterized by the formation of a long thread of fluid that oscillates and breaks up into droplets. This state is known as jetting and greatly differs from dripping, the state at low Ca where drops are formed right after the nozzle.

Dripping and jetting have been claimed to relate to the different kind of instability of a long viscous fluid thread immersed on another viscous fluid [Utada *et al.*, 2007; Herrada *et al.*, 2008]: absolute instability would correspond to dripping, while convective instability would lead to jetting. Recently, good agreement has been found between the absolute to convective instability transition predicted by the linear stability analysis and the dripping to jetting transition observed in experiments [Guillot *et al.*, 2007; Herrada *et al.*, 2008]. However, little of this proves that effectively the dripping and jetting regimes correspond to an absolutely and convectively unstable flow, respectively. In particular one may wonder about the pertinence of the linear stability analysis in the dripping regime, where no parallel flow gets any chance to develop. Moreover, no quantitative measurements on both regimes exist which could be related to the theory.

Here, we provide experimental analysis of the base flow in the dripping and jetting regimes which further confirms the relation of jetting with a convective instability. In particular, we study the frequency response of the jet, both in absence of an external forcing and in presence of a sinusoidal perturbation of variable frequency. First, we analyze the frequency spectrum of both regimes, finding a marked dominant frequency in the dripping regime, and a broad peak in a first region of the jetting regime, in agreement with the theory of convectively unstable flows respectively. However, a second region of the jetting regime also exhibits a sharp peak, which is in contradiction with the theory. This peak, however, is found to be the result of a perturbation induced by the syringe pump which is amplified by the flow.

Then, we study the response of the flow to an external perturbation in the first jetting regime. For that, we locally perturb the jet with a modulated laser at a given frequency. While no reaction is observed in the dripping regime, a strong synchronization occurs in the jetting regime. Drop formation becomes steady and monodisperse on some frequency ranges. Moreover, the size of the drops can be precisely tuned as a function of the frequency laser.

6.2 Spatiotemporal stability theory of a fluid jet

We focus our study on the co-flowing geometry, where one fluid is injected through a nozzle inside another fluid, both fluids flowing in parallel in the same direction. Two different flow behaviours may occur depending, at low Reynolds number, on the competition between viscous and capillary forces, which is described by the capillary number Ca [Guillot *et al.*, 2007]. Briefly,

for Ca below a critical value, surface tension forces the inner fluid to break up right after the nozzle, a behaviour named dripping. For Ca higher than the critical value, the viscous effects overcome surface tension allowing the inner fluid to penetrate into the outer one in the form of a long jet. This jet is not stable, thus eventually breaking up into drops a considerable distance after the nozzle. This state is known as jetting.

Theoretical characterization of these regimes passes through the comprehension of the linear stability of a fluid column, which has been largely studied since the seminal work of Rayleigh [Rayleigh, 1879] and Plateau [Plateau, 1873] in the late 1800s. They considered a long column of a perfect fluid that breaks up under the effect of the capillary force in the absence of an external fluid. Since then, the effect of numerous external and internal parameters, such as the viscosity and density of the internal fluid and of the surrounding medium, fluid velocity and geometrical confinement, have been taken into account [Tomotika, 1935; Lin & Lian, 1992; Subramaniam & Parthasarathy, 2000; Funada *et al.*, 2004].

Recent work has focused on the spatiotemporal stability of a fluid jet [Huerre & Monkewitz, 1990; Leib & Goldstein, 1986; Gañán-Calvo, 2007; Guillot *et al.*, 2008]. Under this framework, deviations from the base flow are written as exponential functions of space and time $e^{i(kz-\omega t)}$, where z is the axial direction, t is the time and k and ω are respectively the wave number and wave frequency of the perturbation. Both k and ω are complex numbers related by a dispersion relation $\omega = \omega(k)$. Instability can be absolute or convective depending on whether the perturbations with zero group velocity are unstable or not. Intuitively, convective instability occurs for flows that are fast enough so they can advect all the perturbations downstream, while absolute instability occurs in the opposite case.

Guillot *et al.* [Guillot *et al.*, 2007] solved the instability problem for a parallel, infinitely long thread of fluid of radius R_i and viscosity η_i that flows in another fluid of viscosity η_e . The two fluids are confined to flow in an axially symmetric geometry of external radius R_e . Inner and outer fluids are injected at flow rates Q_i and Q_e respectively. Guillot *et al.* find for the dispersion relation the following relation:

$$\tilde{\omega} = \frac{\text{Ka}x^3 E(x, \lambda) \tilde{k} + iF(x, \lambda)(\tilde{k}^2 - \tilde{k}^4)}{D(x, \lambda)}, \quad (6.1)$$

where $x = R_i/R_e$ corresponds to the jet's confinement, $\lambda = \eta_i/\eta_e$ is the viscosity ratio, $E(x, \lambda)$, $F(x, \lambda)$ and $D(x, \lambda)$ are positive functions of x and λ and k and ω have been made nondimensional as $\tilde{k} = R_i k$ and $\tilde{\omega} = 16\eta_e R_e \omega / \gamma$. Ka is a capillary number defined in the outer fluid from the velocity at the jet surface v_{jet} :

$$\text{Ka} = \frac{4\eta_e v_{\text{jet}}}{\gamma(1-x^2)}. \quad (6.2)$$

Note that eq. (6.1) states that propagation of perturbations occurs in a nearly non dispersive way. In a temporal analysis, ie. considering $k \in \Re$, eq. (6.1) reads $\omega = v_0 k + i\sigma(k)$, where v_0 is the first order phase velocity of perturbations, which does not depends on k , and $\sigma(k)$ their temporal growth rate.

The transition from absolute to convective instability is predicted by this dispersion relation to occur, for a given value of the confinement x at critical $\text{Ka}^*(x, \lambda)$. Figure 6.1(a) shows Ka^* as a function of x for $\lambda = 0.6$. Alternatively, this relation can be inverted to obtain the transition curve in the (Q_i, Q_e) space, as shown in Fig. 6.1(b).

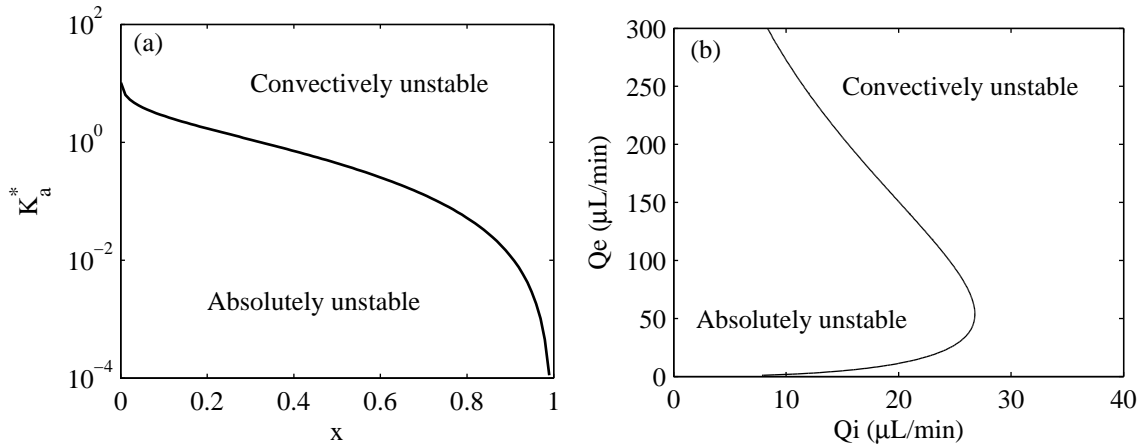


Figure 6.1: Absolute to convective transition curve in the (x, Ka) space (a) and in the (Q_i, Q_e) space (b) for $\lambda = 0.6$.

The dominant frequency f_0 is shown in Fig. 6.2(a) as a function of the inner flow rate for a fixed outer flow rate. In the absolute region, f_0 exhibits a sharp decrease for small Q_i and starts to grow slightly near the transition. In the convective region instead, f_0 decreases slowly.

Figure 6.2(b) shows the phase velocity calculated from the dominant frequency and the associated wavelength λ_0 . The phase velocity is found to grow with Q_i , presenting a discontinuity in its derivative at the transition. The first order phase velocity v_0 is also shown, and it is found to predict fairly the phase velocity everywhere except near the transition.

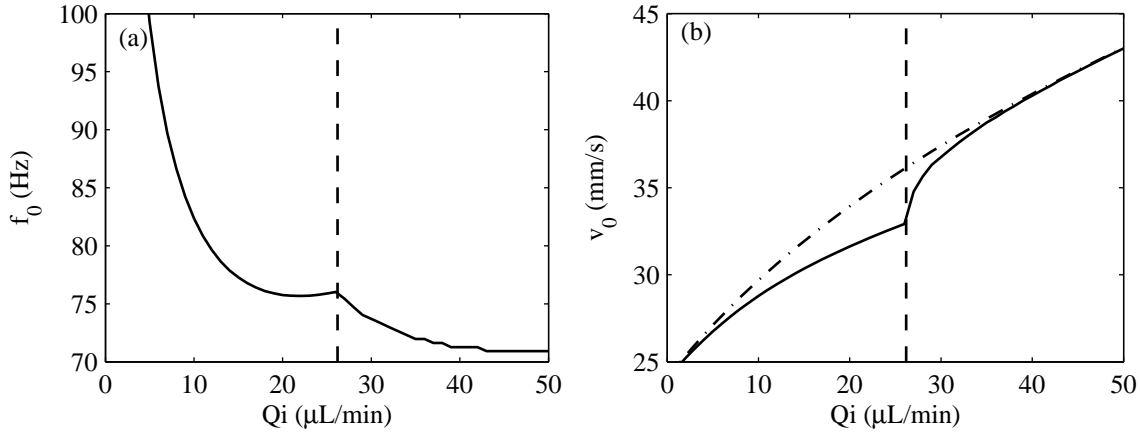


Figure 6.2: (a) Frequency of the dominant perturbation as a function of the inner flow rate. (b) Phase velocity of the perturbations ω_0/k_0 (solid line) and its first order approximation v_0 (dash-dotted line) as a function of the inner flow rate. The dashed line in both figures marks the transition from absolute to convective instability. In these calculations, $Q_e = 30 \mu\text{L}/\text{min}$, $\eta_i = 60 \text{ mPas}$, $\eta_e = 100 \text{ mPas}$, $R_e = 113 \mu\text{m}$ and $\gamma = 40 \text{ mN}/\text{m}$

6.3 Experimental setup

Experiments are performed inside a straight 5 cm length microchannel of square cross section. The microchannel mold is produced by lithography using four layers of a photoresist of thickness $50 \mu\text{m}$ (Etertec XP-800-20) on a glass slide. The channel is then replicated in PDMS prepared in a 10:1.5 ratio of PDMS base with curing agent. Three inlets and one outlet are drilled on the block (see Fig. 6.3). A glass capillary of external diameter $200 \mu\text{m}$ and internal diameter $100 \mu\text{m}$ is placed between the first inlet and pass the third one to form the co-flowing geometry. The alignment of the glass capillary inside the channel is ensured by the matching between the size of the channel and the external diameter of the capillary. After bonding the channel to a glass slide, a drop of PDMS prepared in a 10:0.5 ratio of PDMS base with curing agent is allowed to enter the channel through the second inlet. After flowing by capillarity through the space between the PDMS walls and the glass capillary in both directions, PDMS reaches a wider section of the channel where it stops flowing due to the change of Laplace pressure. This way, sealing of the glass capillary to the external channel forces the inner fluid to flow inside the glass capillary.

Fluids are injected at constant flow rates using syringe pumps (Kd Scientific 101, Harvard Apparatus PHD2000W). The inner fluid is a 80% w/w mixture of glycerol and water, whose viscosity at 20°C is $\eta_i = 60.1 \text{ mPas}$. The outer fluid is silicone oil (Rhodorsil 47 V 100) of viscosity $\eta_e = 100 \text{ mPas}$. Surface tension between both fluids is measured as a function of temperature at $\gamma(T) = 47 - 0.3 T \text{ mN}/\text{m}$, where T is the temperature, in degrees Celsius.

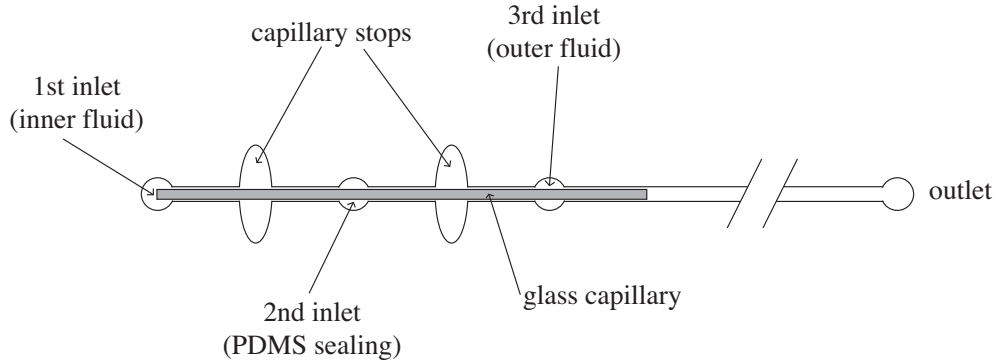


Figure 6.3: Schematic representation of the channel geometry (not to scale).

The channel is mounted on an inverted microscope (Nikon ECLIPSE TE2000-U) and observed through the microscope objective (Nikon, 4x/0.1 NA). Films of 500 frames are recorded at 1000 fps with a fast camera (Photron Fastcam1024 PCI). An infrared laser of wavelength 1480 nm (Fitel Furukawa FOL1425) is focused inside the channel through the same objective, a distance 215 μm from the nozzle. The power of the laser beam is modulated with a signal generator (Wavetek model 80) to a sinusoidal signal of amplitude up to 55 mW and frequency f_{laser} ranging between 10 and 150 Hz.

6.4 Laser forcing

Laser radiation is used to heat the inner fluid by absorption and to produce this way a periodic forcing of the flow by locally changing its parameters. The temperature increase reduces both the surface tension due to its temperature dependence and the inner viscosity due to the large temperature dependence of the viscosity of water/glycerol mixtures [Lide, 2003]. Both effects have contradictory results in the capillary number. To compare both effects, we compute the capillary number Ka , defined earlier in Eq. (6.2), as a function of the temperature increase above room temperature (25°C), as shown in Fig. 6.4. We find that Ka decreases when temperature increases, which means that the effect of the viscosity reduction is more important than that of the surface tension, and therefore the laser acts by locally destabilizing the flow.

The temperature increase depends on the laser power. For the power range used here we expect heating to range between 5°C to 30°C based on our previous results of Chapter 2, which corresponds to a decrease of Ka between 5% and 20%.

The spatial extent of the perturbing forcing is given by the size of the heated region. In absence of flow, we would estimate the heated zone to have a radial extension of approximately

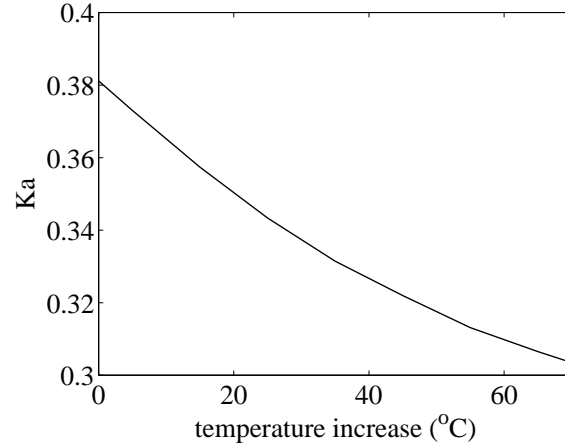


Figure 6.4: Typical capillary number as a function of temperature increase above room temperature.

25 μm . However, large velocities are required to generate the jetting state and in this case heat convection cannot be neglected. The relative importance of heat convection with respect to heat diffusion is quantified by the thermal Peclet number $\text{Pe} = UL/\chi \sim 5$, where $U \sim 20$ mm/s is the mean flow velocity, $\chi \sim 10^{-7}$ m²/s the heat diffusivity of the fluids and $L \sim 25$ μm the radius of the liquid jet. An expansion of the hot zone is to be expected in the direction of the flow, and it can be quantified by taking into account the advection-diffusion equation

$$\chi \nabla^2 T = \mathbf{v} \cdot \nabla T. \quad (6.3)$$

We assume that in the direction perpendicular to the flow the size of the hot zone is of the order of L , while in the direction of the flow the hot zone is of size $L' > L$. Then, the dominant term in the laplacian of the right hand side of Eq. (6.3) is $\sim T/L^2$, while the right hand side can be written as $\sim UT/L'$. Dividing both sides by χ/L we obtain:

$$\frac{T}{L} = \frac{UL}{\chi} \frac{T}{L'} = \text{Pe} \frac{T}{L'}, \quad (6.4)$$

or $L' = \text{Pe}L$. This means that an expansion of the hot zone in a factor Pe is to be expected in the direction of the flow. Therefore, we expect the hot zone to have a size similar to the jet radius in the direction perpendicular to the flow and about 5 times larger in the direction of the flow.

From the size of the heated zone and the mean flow velocity, a frequency can be calculated as $f_{\text{th}} = 200$ Hz. This frequency describes the rate at which the fluid passes through the heated zone. To produce a significative forcing of the jet, the laser frequency should remain smaller or at most similar to f_{th} , which is the case here.

6.5 Experimental results

6.5.1 Unperturbed state

First, we study the flow behaviour in the absence of laser beam. For a fixed external flow rate $Q_e = 30 \mu\text{L}/\text{min}$, the inner flow rate Q_i is increased gradually from $5 \mu\text{L}/\text{min}$ to $32 \mu\text{L}/\text{min}$ and a transition from dripping [Fig. 6.5(a)] to jetting [Fig. 6.5(b)] is observed, as has been observed elsewhere [Cubaud & Mason, 2008; Guillot *et al.*, 2008].

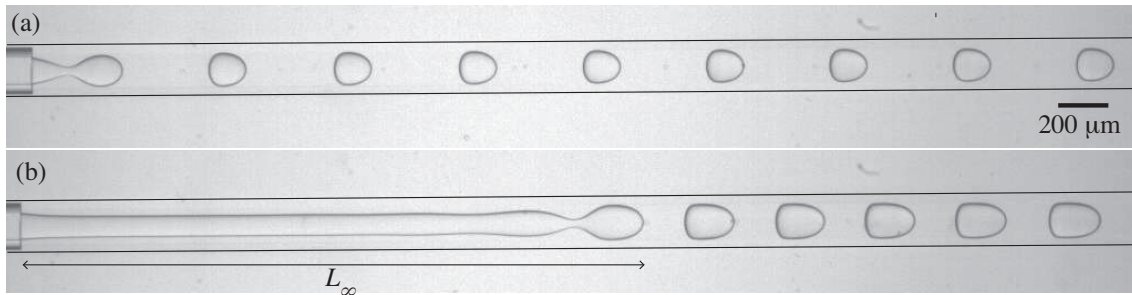


Figure 6.5: Snapshots of the system in the dripping (a) and in the jetting (b) regimes.

The length of the inner fluid column, L_∞ , is measured as a function of Q_i and is shown in Fig. 6.6. Error bars are calculated considering the minimum and maximum values measured for L_∞ during the drop formation process. For low Q_i , L_∞ is small and grows only slightly with Q_i . This corresponds to the dripping regime. Error bars are small because drop formation occurs at a steady position. At $Q_i = 14 \mu\text{L}/\text{min}$, the jet starts to grow, showing that the jetting regime has been attained. Dispersion also grows, reflecting the fact that the position of drop pinch off is not as well defined as in the dripping regime.

We measure the jet's radius as a function of space and time, and perform a temporal discrete Fourier transform to obtain the frequency spectrum of oscillations of the jet's radius. The natural frequency f_0 is defined from these measurements as the position of the maximum of the density spectrum for each Q_i . Density spectra amplitude for the different inner flow rates are shown in Fig. 6.7(a). In the dripping region ($Q_i < 14 \mu\text{L}/\text{min}$) a sharp peak is observed. Its position f_0 increases linearly with Q_i . In the jetting regime, instead, two regions can be distinguished. First, for $14 < Q_i < 24 \mu\text{L}/\text{min}$, a broadening of the peak can be observed. We call this region "first jetting regime". Here, the position of the peak decreases with Q_i . Then, for $Q_i > 24 \mu\text{L}/\text{min}$, a sharp peak whose position increases linearly with Q_i can be observed again. This region is called "second jetting regime".

The wavelength of oscillations λ_0 could not be accurately obtained from discrete spatial

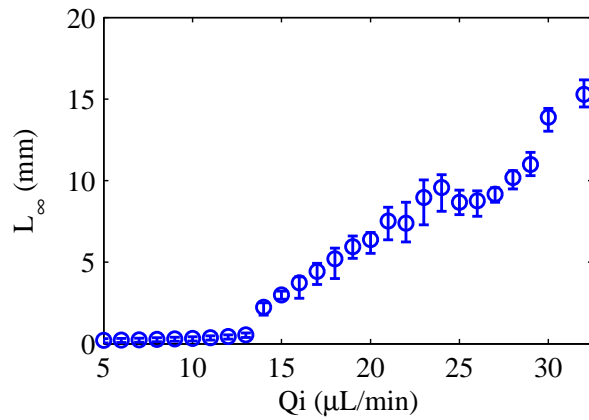


Figure 6.6: Length of the inner fluid column as a function of the inner flow rate for a fixed value of the external flow rate.

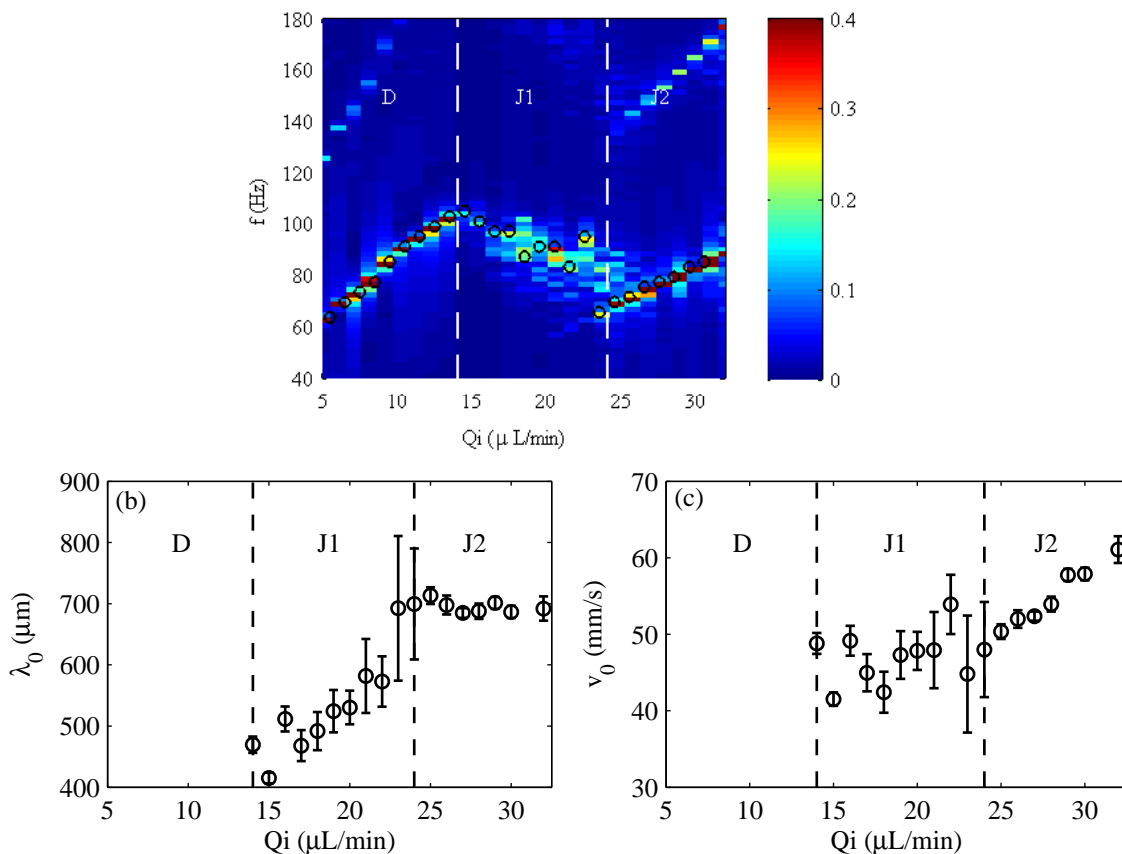


Figure 6.7: (a) Frequency spectrum of the jet as a function of Q_i . The scale is in arbitrary units. Circles show the maximum of each spectrum f_0 . (b) and (c) Wavelength and phase velocity of the jet respectively as a function of Q_i . Dashed lines are used to separate the different behaviours: Dripping (D), first jetting regime (J1) and second jetting regime (J2).

Fourier transform due to the poor spatial resolution of the optical setup. Instead, in the jetting region, it was deduced from the drop size and the jet thickness, obtained by image analysis, and assuming volume conservation. Figure 6.7(b) shows λ_0 as a function of the inner flow rate. Error bars are calculated from the dispersion of the drop size distribution. In the first jetting regime, λ_0 increases with Q_i and dispersion is important. In the second jetting regime, λ_0 remains constant, with little dispersion.

Finally, the phase velocity is calculated from the frequency and wavelength of oscillations as $v_0 = \lambda_0 f_0$ and is plotted on Fig. 6.7(c). Within the first jetting regime, v_0 remains constant at around 45 mm/s with big dispersion, due to the big error bars of λ_0 . In the second jetting regime, v_0 increases linearly, with low dispersion.

6.5.2 Perturbed state

When the laser is turned on, different behaviours are observed. In the dripping regime, no noticeable effect is detected on the flow, even at highest laser power. Indeed, frequency spectra show the dominance of the natural frequency f_0 and only at high laser power, the peak corresponding to f_{laser} is present, but its amplitude is much smaller than the dominant one (Fig. 6.8), thus not changing noticeably the flow.

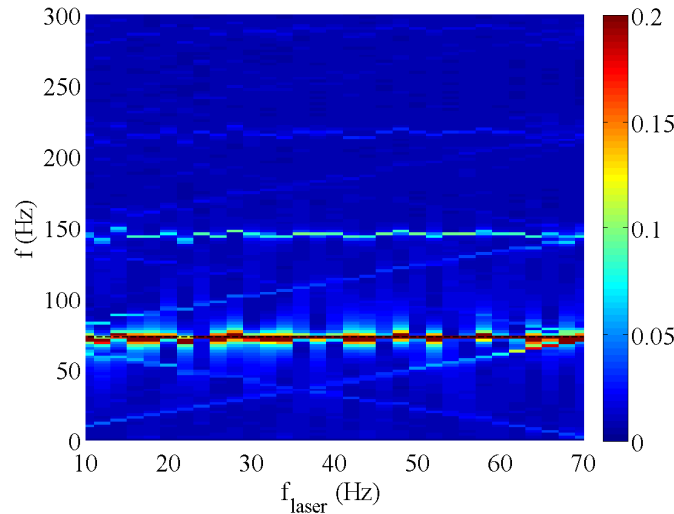


Figure 6.8: Spectral density amplitude as a function of f_{laser} for a dripping flow forced with a laser beam. The solid line corresponds to the natural frequency f_0 . In this case $Q_i = 10 \mu\text{L}/\text{min}$ and $Q_e = 20 \mu\text{L}/\text{min}$.

In the first jetting regime, no or little response of the jet is observed for low laser power. When the laser power is increased, the jet's oscillations synchronize to the laser frequency on some

frequency ranges. Two main effects are observed in the frequency ranges where synchronization occurs: the length of the jet decreases as the laser power increases and the drop size changes.

Figure 6.9 shows snapshots of the jet forced by the laser with a frequency $f_{\text{laser}} = 70$ Hz at different laser powers. For the lowest power used no changes of the drop size occur and only a slight decrease of the jet length is observed. As the laser power increases, the drops are bigger and the jet becomes shorter.

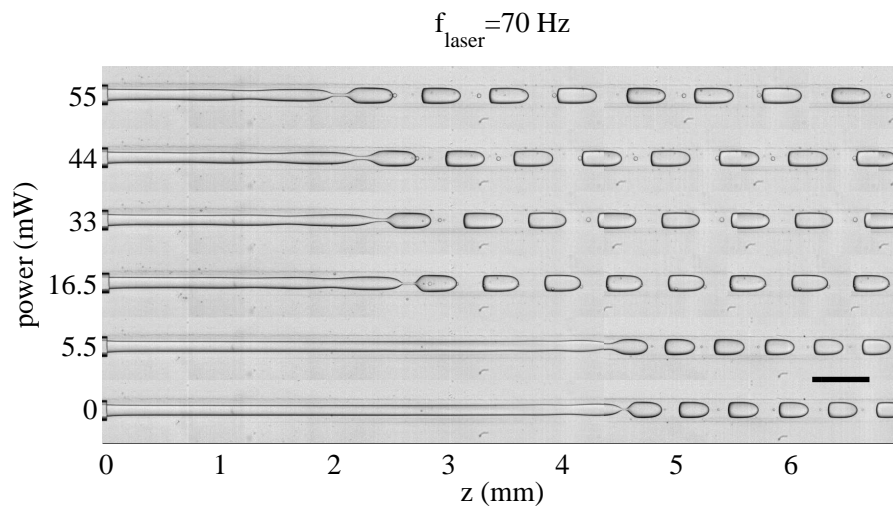


Figure 6.9: Images of the jet perturbed with a laser beam at a constant frequency $f_{\text{laser}} = 70$ Hz and different laser powers. Here $Q_i = 20 \mu\text{L}/\text{min}$ and $Q_e = 30 \mu\text{L}/\text{min}$. The scale bar represents $500 \mu\text{m}$.

The frequency spectrum of the jet was measured in the presence of the laser forcing for a fixed flow rate configuration ($Q_e = 30 \mu\text{L}/\text{min}$ and $Q_i = 20 \mu\text{L}/\text{min}$). Figure 6.10(a) shows the spectral density amplitude of the jet's radius oscillations as a function of f_{laser} for a laser power of 55 mW (similar results were obtained for laser power higher than 11 mW). A strong dominance of the laser frequency can be observed in the range $f_{\text{laser}} = 55 - 120$ Hz. Note that harmonics of f_{laser} are also present in the spectrum of Fig. 6.10. In the range $f_{\text{laser}} < 55$ Hz the dominant peak correspond to the second harmonic $2f_{\text{laser}}$, and therefore in this region the jet's oscillations are also controlled by the laser induced perturbations.

By analysis of the drop size distribution and considering the mean radius of the unperturbed jet, the wavelength of the jet oscillations is computed. Figure 6.10(b) shows the jet's radius oscillations wavelength λ , as a function of the laser frequency. In the range $f_{\text{laser}} = 55 - 120$ Hz, λ is found to decrease with f_{laser} , following the relation $f_{\text{laser}} \lambda = v_0$. Here, v_0 is the phase velocity calculated in the unperturbed state from f_0 and λ_0 . Note that for $f_{\text{laser}} < 55$ Hz, although

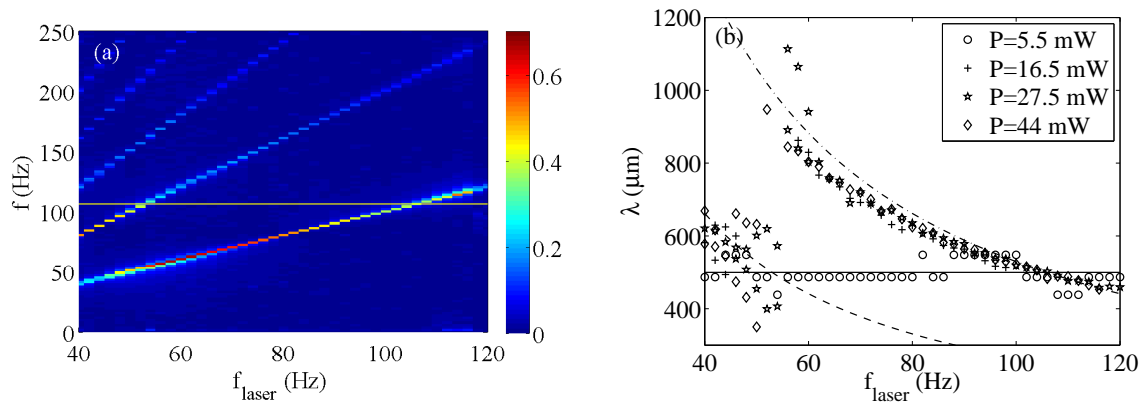


Figure 6.10: (a) Spectral density of the oscillations of the jet's radius as a function of the laser frequency f_{laser} . The solid line shows the value of the dominant frequency in the absence of laser f_0 for this flow rate configuration. (b) Wavelength of the jet's radius oscillations as a function of the laser frequency f_{laser} for different laser power. The solid line corresponds to the wavelength of the unperturbed jet's oscillations. The dot dashed line corresponds to the curve $f_{\text{laser}}\lambda = v_0$, while the dashed line corresponds to $2f_{\text{laser}}\lambda = v_0$

the wavelength is much more dispersed, it is coherent with the relation $2f_{\text{laser}}\lambda = v_0$, as suggest the dominance of the second harmonic of f_{laser} in the frequency spectrum.

Finally, Fig. 6.11 shows the dispersion percentage of the drop size population, calculated as the standard deviation of the drop sizes divided by the average drop size, as a function of f_{laser} . Remarkably, the dispersion in the drop size, which is high in the jetting regime, decreases by a factor of about 5 in the presence of the laser forcing.

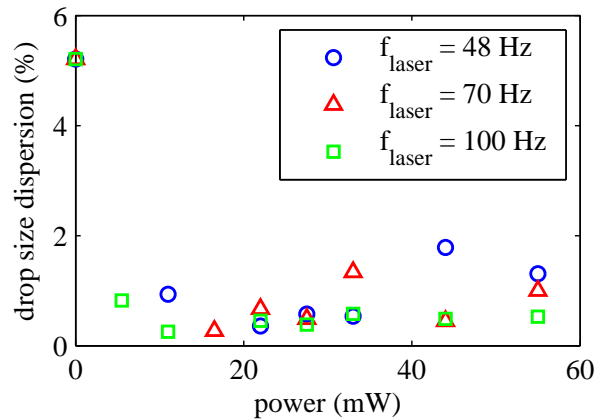


Figure 6.11: Dispersion of the drop size distribution as a function of the laser frequency.

Similar measurements were performed in the first jetting regime close to the dripping to

jetting transition. For low and intermediate laser power the behaviour is qualitatively the same as the one shown above. At high laser power, however, a strong decrease in the jet's length L_∞ was observed, as shown in Fig. 6.12. In this case, we observe the formation of small, mono disperse drops whose size no longer depends on f_{laser} , as shown in Fig. 6.12(b).

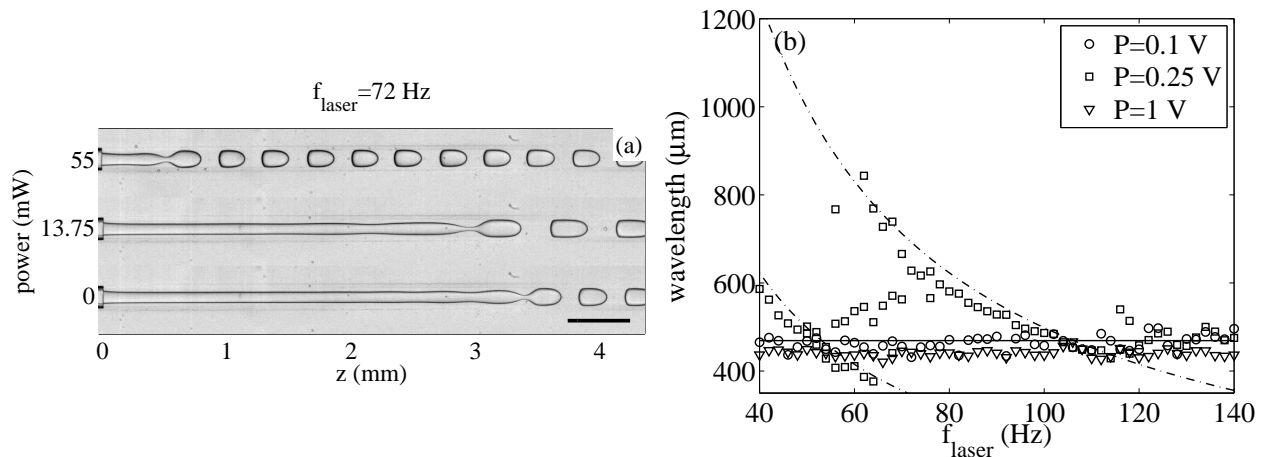


Figure 6.12: (a) Images of the jet near the dripping to jetting transition perturbed with a laser beam at $f_{\text{laser}} = 72$ Hz and different power. The scale bar represents $500 \mu\text{m}$. (b) Wavelength of the jet's oscillations as a function of the laser frequency for different laser power. The solid line represents the dominant wavelength of the unperturbed state. The dash-dotted line represent the curves $\lambda = v_0/m f_{\text{laser}}$ with $m = 1, 2$

6.6 Discussion

Convectively unstable flows are known to act as noise amplifiers. In the absence of any disturbance perturbations are advected downstream and the flow goes back rapidly to the base state. Usually, however, noise is present, so the flow is not in its base state. Although the most amplified frequency in this case corresponds to that with the highest growth rate, convectively unstable flows amplify a broad range of unstable frequencies.

Conversely, a single, well defined perturbation dominates the behaviour of absolutely unstable flows. This is because in absolutely unstable flows the perturbation with zero group velocity is unstable, and while all other perturbations are advected, this one is not and grows in a fixed place. The absolute frequency corresponds, therefore, to the perturbation with zero group velocity. Absolutely unstable flows do not respond to external noise and always deviate exponentially from the base state.

Our measurements of the flow in absence of laser forcing finds this latter characteristic on the dripping regime, where one well defined frequency peak dominates the frequency spectrum. However, when the position of the peak as a function of Q_i is compared to the theoretical predictions, a strong qualitative disagreement is found. The theory predicts f_0 to decrease steeply as a function of Q_i for small Q_i , which would result in the formation of larger drops at a smaller rate. On the contrary, we measure a linear increase in f_0 with Q_i , that is, the formation of drops of constant volume at a higher rate. These results suggest that drop formation in the dripping regime is ruled by a mechanism different from an absolute instability.

In the jetting regime, two regions were observed. In the first jetting regime, a broad range of frequencies are noise-amplified. On the contrary, a single, well defined peak dominates the frequency spectrum of the jet oscillations in the second jetting regime. The first jetting regime exhibits a decrease of f_0 with the inner flow rate, which is coherent with the theory predictions in the convective regime. On the contrary, f_0 increases linearly in the second jetting regime, in contradiction with the theoretical results. However, this behaviour suggests the presence of an externally imposed perturbation associated with the syringe pump that controls the inner flow rate which is amplified by the flow. In fact, the pumping rate of the syringe pump increases linearly with Q_i as

$$f_{\text{pump}} = \frac{4Q_i}{\pi D^2 dx}, \quad (6.5)$$

where $D = 4.61$ mm is the syringe diameter and $dx = 0.088$ μm the syringe pump step. While f_{pump} is too high compared to f_0 in the second jetting regime, its fourth sub-harmonic ($f_{\text{pump}}/4$) matches it precisely, as shown in Fig. 6.13. Moreover, note that the second sub-harmonic ($f_{\text{pump}}/2$) is also present in the frequency spectrum of Fig. 6.7(a). This result shows that in the second jetting regime there is also a broad range of unstable frequencies, but the dominant one relates to the frequency imposed by the pumping rate of the inner fluid.

Figure 6.13 summarizes the frequency response of the system. Red zones represent the frequencies that are present in the density spectrum of the flow. In the dripping regime there is only one, well defined frequency, while a broad range of frequencies are present in the jetting regimes. When the frequency imposed by a perturbation lies in the unstable range of the jetting regime, the external frequency is amplified, dominating the system. These results are coherent with a convective nature of the flow instability in the jetting regime.

This hypothesis is confirmed by our experiments with the external forcing imposed by the laser in the jetting regime. These experiments show the synchronization of the jet's oscillations with the laser frequency, demonstrating the ability of the jet to amplify externally induced per-

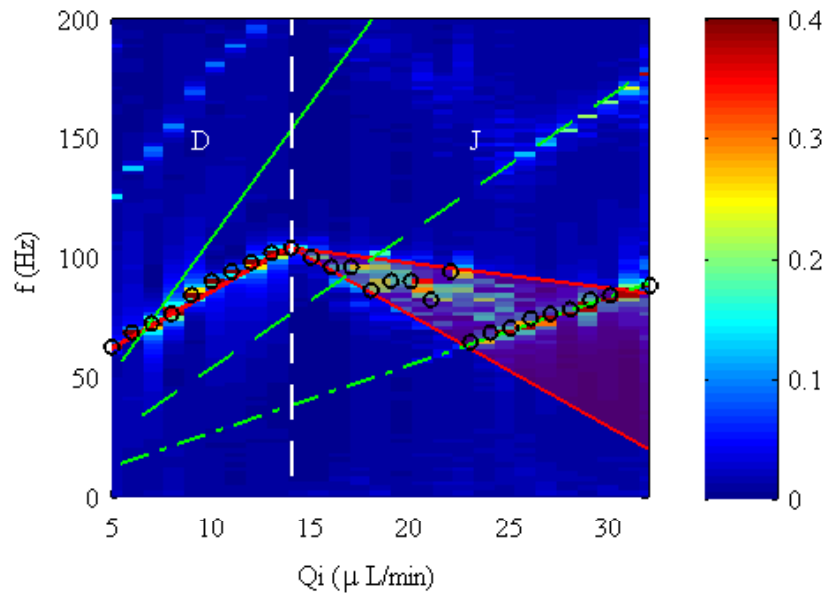


Figure 6.13: Frequency response of the jet as a function of Q_i for fixed Q_e . Circles correspond to the dominant frequency for each Q_i . Red zones represent the amplified frequencies. Green lines correspond to the pumping rate (solid line) and its second (dashed line) and fourth (dot dashed line) sub-harmonics. J now stands for the jetting regime.

turbations. The amplified perturbations are found to follow qualitatively the dispersion relation, which states that, at first order, the frequency and wavelength are related through a constant phase velocity.

It was observed that when the flow was in the jetting regime but near the transition to dripping, laser could cause a strong destabilization if the laser power was too high. This can be explained by remembering that the heating reduces the inner viscosity, and thus can decrease the capillary number below its critical value in the zone heated by the laser. This would lead to the creation of a locally absolutely unstable region, where the perturbation with zero group velocity is locally amplified. Generation of monodisperse drops a small distance after the laser position confirms this picture.

In conclusion, we have given experimental evidence to confirm that the jetting regime in a co-flowing system relates to a convective instability. Conversely, we argue that the mechanisms involved in drop formation in the dripping regime does not correspond to an absolute instability.

Confirmation of the instability nature of the flow in the jetting regime is important to understand the mechanisms that control drop formation when capillary and viscous effects are in competition. In particular, spatiotemporal stability analysis predicts high inherent dispersion

in drop sizes in the jetting regime. This is because noise sources, such as micrometer sized fabrication defects of the channel walls or fluctuations in the pressure and flow rates, are unavoidably present. While this kind of perturbations are rapidly damped and usually negligible in microfluidics, they are exponentially amplified by a convectively unstable flow. At the same time, comprehension of the flow nature provides a way to control this polydispersity by inducing the amplification of a preferred single frequency with a controlled forcing. Here, we do so with periodic, localized laser heating, demonstrating the possibility of externally tuning the frequency of drop formation and the drop size with a low dispersion.

Chapter 7

Conclusions

Digital microfluidics promises to revolutionize the way that biological and chemical analyses are done by implementing the full set of laboratory processes inside drops that flow in microchannel networks. Drops in microfluidics contain a volume on the pico- to nanoliter scale and can be used as individual reaction chambers, allowing to encapsulate and isolate reagents and to parallelize a large number of reactions in a single microfluidic chip, thus reducing the material used for an analysis and the time necessary to carry it out. At the same time, the implementation of digital microfluidics opens new technological challenges, particularly to achieve a precise control of microdrops. The development of a droplet-based lab-on-a-chip requires the implementation of functions that allow steady drop production, controlled drop transport, precise manipulation of the drop contents, reproducible drop fusion and drop division and sensitive detection of their contents.

In this sense, this thesis work gives an answer to the need of mechanisms to actively manipulate drops in microfluidics. Specifically, the objective of this thesis is the development of an optical toolkit able to exert control over microfluidic drops by the use of a laser beam. This objective has been addressed, first, by a characterization of the thermal, physicochemical and hydrodynamical aspects of the laser-based technique, which has allowed us to understand the physical mechanisms involved in the laser manipulation and its limitations. Then, based on this characterization and taking into account the limitations, the laser tool was developed for achieving the control of drops in three different functions, namely the routing of drops inside a microchannel, mixing the contents of a drop and control of the size of drops during the drop formation process.

The thermal aspects of the laser-based technique of this thesis are shown in Chapter 2 and concern the evolution of the temperature and the amplitude and extent of the temperature increase

in the steady state due to the absorption of the laser radiation by the aqueous drops. It was found that the time for reaching a steady state in the temperature field is of a few milliseconds, while in the steady state the temperature increase is of a few tens of degrees Celsius within a region of $25\ \mu\text{m}$ radius. These experimental results are accompanied by simulations of the laser heating, which agree with the experimental measurements for low laser powers and can be used to predict the laser heating in different geometries.

The physicochemical and hydrodynamical aspects of the laser forcing are shown in Chapter 3. In summary, it was found that the heating of the drop surface with the laser radiation triggers a series of physicochemical and hydrodynamical processes which cause the apparition of a net force on the drop as follows: Product of the heating, the concentration of surfactant molecules adsorbed on the interface is reduced in the heated zone, which increases locally the surface tension. The creation of a gradient of surface tension induces a Marangoni flow that consists of a pair of symmetric recirculation rolls inside the drop that approach the laser position along the drop surface and go away through the center of the drop, with its equivalent in the external fluid phase. This flow shears the drop interface, specially in the thin films of fluid that exist between the drop surface and the channel walls. The integrated shear in the drop surface is responsible for the apparition of a repulsive net force on the drop. This force was measured on the order of 100 nN, increasing with the temperature gradient.

A first important limitation of the laser forcing is revealed in Chapter 3 by the measurements of the velocity field inside the drops, which indicate that the apparition of the Marangoni flow, and therefore the development of the force, is simultaneous to the increase of temperature. This limits the time for setting the force on the drops to the heating time.

In Chapter 4 we show that the use of spatially extended laser patterns produced with holographic techniques can be used to overcome the limitation imposed by the heating time scale by increasing the region where the laser force is applied. Moreover, we present sophisticated applications of the laser force to sort and store drops in a microchannel by using dynamical laser patterns obtained with holographic techniques. In particular, we show that these laser patterns can act like walls to steer the drops in a sorting device and can multiply the control on the drops trajectory to several drops in different places of the microchannel simultaneously.

The laser forcing is also used to induce mixing of the drop contents by manipulating the Marangoni flow inside a drop stopped by the laser force, as shown in Chapter 5. In this sense, mixing is limited by the spatial symmetry of the Marangoni flow. This symmetry prevents the total mixing of the drop contents due to the presence of a virtual surface separating the two recirculation rolls which is not crossed by any streamlines. To achieve mixing, the symmetry of

the Marangoni flow is broken by alternating the laser between two positions at the front of the drop. The switching of the laser position modulates the surface that divides the rolls, allowing the communication between the two zones of the drop and therefore allowing mixing.

The utility of the laser tool is expanded in Chapter 6, where we show that the laser beam can be used as a tool to tune the frequency of drop formation and the drop size in a co-flowing device. In a co-flowing geometry two regimes can exist depending on the capillary number. For low capillary numbers a dripping regime is observed, characterized by a steady drop formation. Instead, for high capillary number a jetting regime appears, which does not present steady drop formation. We show that, in the latter case, the system responds to the periodic forcing imposed by a laser beam whose power has been sinusoidally modulated. This forcing is not driven by solutocapillarity like the laser-induced force on the drops, but by a localized decrease of the viscosity of the inner fluid in the heated zone, which reduces locally the capillary number. In the presence of such a periodic forcing, the system is induced to produce drops at the frequency imposed by the laser. In this way, drops of a fixed size can be produced and the size can be tuned by adjusting the frequency of the laser modulation.

The perspectives opened for applications of this work are multiple. As mentioned before, the development of microfluidics requires the implementation of functions to control the drops behaviour at various stages. This work, therefore, offers a laser technique to achieve this control. The heating involved in the use of the laser technique makes it specially suited for applications that require heating the components. In this sense, it would be particularly interesting to use the laser forcing with drops that contain the reagents for an endothermic reaction. In this case, heat acts as a catalyst for the reaction and therefore the laser beam can be used simultaneously to stop a drop for observation while mixing its components and triggering the chemical reaction.

In such a case the laser heating is an advantage, since it favors the analysis that one wants to study. In some other cases, on the contrary, laser heating may be seen as a disadvantage since it may damage the drop contents, as for example in the case of cells. For applications where heating may be dangerous, using the laser technique to mix the drop contents may be unsuitable. In fact, as shown in Chapter 5, the Marangoni flow imposes little heating to most of the drop contents, while the fluid particles that experiment the highest temperature increase are heated for short times and with long periods at ambient temperature. By mixing the drop contents, the possibility of exposing the sensitive samples to significant heating increases. However, for purposes of routing and tuning the drop formation, the laser tool keeps its utility in cases where heating is not advisable.

Holographic techniques can be used to parallelize the use of the laser beam in microfluidic applications, as already shown in Chapter 4. In this sense, one can imagine applications where several laser spots are used to simultaneously tune the size of drops in a co-flowing device, store them in an array and mix their contents. Holographic techniques, however, are not widely spread and introduce large complexity to the system. Moreover, the frequency of switching between holograms is limited to a few Hertz and therefore cannot achieve the high throughputs required for series LOC applications. Instead, other simpler techniques may be used, as the utilization of galvanometric mirrors that displace the laser beam across the microchannel geometry. Galvanometric mirrors can tilt at frequencies up to some megahertz with precision of a fraction of a millisecond of arc, thus rendering a single laser beam ubiquitous, emulating the function of the holograms but with higher performance.

Concerning the more fundamental aspects of the thesis, an open question remains regarding the mechanism involved in the redistribution of surfactant due to the laser heating. One hypothesis has been invoked, which is the thermal migration of surfactant micelles, lowering the local concentration of surfactant and therefore promoting the desorption of surfactant from the drop interface. However, other mechanisms may be present. This question, lying beyond the objective of this thesis, constitutes an interesting fundamental physicochemical problem.

Furthermore, the three dimensional nature of the flows was ignored within most part of this thesis. In fact, the shallow approximation was used, which consists in averaging the flow over the depth of the microchannel, supposing a parabolic profile in that direction. This approximation is valid for high aspect ratio w/h , with w and h the width and depth of the microchannel, respectively. However, it is probable that the Marangoni flow has a component in the third direction and this component may have an important influence on both the laser-induced force created on the drops and the mixing using the Marangoni flow. An approach to deal with this three dimensional flow could include numerical simulations, confocal microscopy in order to obtain three dimensional velocity fields or the construction of microchannels with low aspect ratio w/h .

Bibliography

- ABATE, A. R., ROMANOWSKY, M. B., AGRESTI, J. J. & WEITZ, D. A. 2009 Valve-based flow focusing for drop formation. *Appl. Phys. Lett.* **94**, 023503.
- ADZIMA, B. J. & VELANKAR, S. S. 2006 Pressure drops for droplet flows in microfluidic channels. *J. Micromech. Microeng.* **16**, 1504–1510.
- AHN, K., AGRESTI, J., CHONG, H., MARQUEZ, M. & WEITZ, D. A. 2006a Electrocoalescence of drops synchronized by size-dependent flow in microfluidic channels. *Appl. Phys. Lett.* **88**, 264105.
- AHN, K., KERBAGE, C., HUNT, T. P., WESTERVELT, R. M., LINK, D.R. & WEITZ, D. A. 2006b Dielectrophoretic manipulation of drops for high-speed microfluidic sorting devices. *Appl. Phys. Lett.* **88** (2), 024104.
- ANNA, S. L., BONToux, N. & STONE, H. A. 2003 Formation of dispersions using “flow focusing” in microchannels. *Appl. Phys. Lett.* **82** (3), 364–366.
- AREF, H. 1984 Stirring by chaotic advection. *J. Fluid Mech.* **143**, 1–21.
- ASHKIN, A., DZIEDZIC, J. M., BJORKHOLM, J. E. & CHU, S. 1986 Observation of a single-beam gradient force optical trap for dielectric particles. *Opt. Lett.* **11** (5), 288–290.
- BAR-ZIV, R. & MOSES, E. 1994 Instability and “pearling” states produced in tubular membranes by competition of curvature and tension. *Phys. Rev. Lett.* **73** (10), 1392.
- BAROUD, C. N., DELVILLE, J. P., GALLAIRE, F. & WUNENBURGER, R. 2007a Thermocapillary valve for droplet production and sorting. *Phys. Rev. E* **75** (4), 046302.
- BAROUD, C. N., DE SAINT VINCENT, M. R. & DELVILLE, J. P. 2007b An optical toolbox for total control of droplet microfluidics. *Lab Chip* **7**, 1029–1033.

- BARTOLO, D., BOUAMRIRENE, F., VERNEUIL, E., BUGUIN, A., SILBERZAN, P. & MOULINET, S. 2006 Bouncing or sticky droplets: Impalement transitions on superhydrophobic micropatterned surfaces. *Europhys. Lett.* **74** (2), 299–305.
- BAU, H. H., ZHONG, J. & YI, M. 2001 A minute magneto hydro dynamic (MHD) mixer. *Sens. Actuators B* **79**, 207–215.
- BRAUN, D. & LIBCHABER, A. 2002 Trapping of DNA by thermophoretic depletion and convection. *Phys. Rev. Lett.* **89** (18), 188103.
- BRZOSKA, J. B., BROCHARD-WYART, F. & RONDELEZ, F. 1993 Motion of droplets on hydrophobic model surfaces induced by thermal gradients. *Langmuir* **9**, 2220–2224.
- BURNHAM, D. R. & MCGLOIN, D. 2006 Optical guiding of aerosol droplets. *Optics Express* **14** (9), 4176–4182.
- BURNHAM, D. R., WRIGHT, G. D., READ, N. D. & MCGLOIN, D. 2007 Holographic and single beam optical manipulation of hyphal growth in filamentous fungi. *J. Opt. A* **9**, S172–S179.
- BUSH, J. 1997 The anomalous wake accompanying bubbles rising in a thin gap: mechanically forced Marangoni flow. *J. Fluid Mech* **352**, 283–303.
- CAMPANELLI, J. R. & WANG, X. 1999 Dynamical interfacial tension of surfactant mixtures at liquid-liquid interfaces. *J. Coll. Inter. Sc.* **213**, 340–351.
- CARROLL, N. J., RATHOD, S. B., DERBINS, E., MENDEZ, S., WEITZ, D. A. & PETSEV, D. N. 2008 Droplet-based microfluidics for emulsion and solvent evaporation synthesis of monodisperse mesoporous silica microspheres. *Langmuir* **24** (3), 658–661.
- CARSLAW, H. S & JAEGER, J. C. 1959 *Conduction of Heat in Solids*. Oxford at the Clarendon Press.
- CASEY, K. G. & QUITEVIS, E. L. 1988 Effect of solvent polarity on nonradiative processes in xantene dyes: Rhodamine B in normal alcohols. *J. Phys. Chem* **92**, 6590–6594.
- CASTRO-HERNÁNDEZ, E., GUNDABALA, V., FERNÁNDEZ-NIEVES, A. & GORDILLO, J. M. 2009 Scaling the drop size in coflow experiments. *New Journal of Physics* **11**, 075021.

- CHABERT, M., DORFMAN, KEVIN D. & VIOVY, J. L. 2005 Droplet fusion by alternating current (AC) field electrocoalescence in microchannels. *Electrophoresis* **26**, 3706–3715.
- CHABERT, M & VIOVY, J. L. 2008 Microfluidic high-throughput encapsulation and hydrodynamic self-sorting of single cells. *PNAS* **105** (9), 3191–3196.
- CHABREYRIE, R., VAINCHTEIN, D., CHANDRE, C., SINGH, P. & AUBRY, N. 2008 Tailored mixing inside a translating droplet. *Phys. Rev. E* **77**, 036314.
- CHEN, J. & STEBE, K. J. 1997 Surfactant-induced retardation of the thermocapillary migration of a droplet. *J. Fluid Mech.* **340**, 35–59.
- CORTESE, B., D'AMONE, S., MANCA, M., VIOLA, I., CINGOLANI, R. & GIGLI, G. 2008 Superhydrophobicity due to the hierarchical scale roughness of PDMS surfaces. *Langmuir* **24**, 2712–2718.
- CRISTOBAL, G., BENOIT, J. P., JOANICOT, M. & AJDARI, A. 2006 Microfluidic bypass for efficient passive regulation of droplet traffic at a junction. *Appl. Phys. Lett.* **89** (3), 034104.
- CUBAUD, T. & MASON, T. G. 2008 Capillary threads and viscous droplets in square microchannels. *Phys. Fluids* **20**, 053302.
- CURTIS, J. E., KOSS, B. A. & GRIER, D. G. 2002 Dynamic holographic optical tweezers. *Opt. Comm.* **207** (1-6), 169–175.
- DA COSTA, G. 1993 Optical visualization of the velocity distribution in a laser-induced thermocapillary liquid flow. *Appl. Opt.* **32** (12), 2143.
- DARHUBER, A. A. & TROIAN, S. M. 2005 Principles of microfluidic actuation by modulation of surface stresses. *Annu. Rev. Fluid Mech.* **37**, 425–455.
- DENDUKURI, D., TSOI, K., HATTON, T. A. & DOYLE, P. S. 2005 Controlled synthesis of nonspherical microparticles using microfluidics. *Langmuir* **21** (6), 2113–2116.
- DILEONARDO, R., IANNI, F. & RUOCCO, G. 2007 Computer generation of optimal holograms for optical trap arrays. *Optics Express* **15**, 1913.
- DUHR, S. & BRAUN, D. 2004 Thermophoresis of DNA determined by microfluidic fluorescence. *Eur. Phys. J. E* **15**, 277–286.

- DUHR, S. & BRAUN, D. 2006a Optothermal molecule trapping by opposing fluid flow with thermophoretic drift. *Phys. Rev. Lett.* **97** (3), 038103.
- DUHR, S. & BRAUN, D. 2006b Thermophoretic depletion follows Boltzmann distribution. *Phys. Rev. Lett.* **96** (16), 168301.
- EASTOE, J. & DALTON, J. S. 2000 Dynamic surface tension and adsorption mechanisms of surfactants at the air-water interface. *Adv. Coll. Int. Sci.* **85**, 103–144.
- EGGERS, J. 1993 Universal pinching of 3D axisymmetric free-surface flow. *Phys. Rev. Lett.* **71** (21), 3458–3460.
- EL MOCTAR, A. O., AUBRY, N. & BATTON, J. 2003 Electro-hydrodynamic micro-fluidic mixer. *Lab Chip* **3**, 273–280.
- ENGL, W., ROCHE, M., COLIN, A & PANIZZA, P. 2005 Droplet traffic at a simple junction at low capillary numbers. *Phys. Rev. Lett.* **95**, 208304.
- ESPEAU, P. & CEOLIN, R. 2006 A simple method to determine the specific volumes of liquids and melts as a function of the temperature - application to four n-alkanes (C16H34, C18H38, C19H40 and C21H44) under saturating vapour pressure in the 298-573°K range. *Thermochimica Acta* **445**, 32–35.
- FRANKE, T., ABATE, A. R., WEITZ, D. A. & WIXFORTH, A. 2009 Surface acoustic wave (SAW) directed droplet flow in microfluidics for PDMS devices. *Lab Chip* **9**, 2625–2627.
- FROMMELT, T., KOSUR, M., WENZEL-SCHAFFER, M., TALKNER, P., HANGGI, P. & WIXFORTH, A. 2008 Microfluidic mixing via acoustically driven chaotic advection. *Phys. Rev. Lett.* **100**, 034502.
- FUERSTMAN, M. J., GARSTECKI, P. & WHITESIDES, G. M. 2007a Coding/decoding and reversibility of droplet trains in microfluidic networks. *Science* **315**, 828.
- FUERSTMAN, M. J., LAI, A., THURLOW, M. E., SHEVKOPLYAS, S. S., STONE, H. A. & WHITESIDES, G. M. 2007b The pressure drop along rectangular microchannels containing bubbles. *Lab Chip* **7**, 1479–1489.
- FUNADA, T., JOSEPH, D. D. & YAMASHITA, S. 2004 Stability of a liquid jet into incompressible gases and liquids. *Intl. J. Multiphase Flow* **30**, 1279–1310.

- FUNFSCHILLING, D., DEBAS, H., LI, H. Z. & MASON, T. G. 2009 Flow-field dynamics during droplet formation by dripping in hydrodynamic-focusing microfluidics. *Phys. Rev. E* **80**, 015301(R).
- FUSHINOBU, K., PHINNEY, L. M. & TIEN, N. C. 1996 Ultrashort-pulse laser heating of silicon to reduce microstructure adhesion. *Int. J. Heat Mass Transfer* **39**, 3181–3186.
- GAÑÁN-CALVO, A. M. 2007 Absolute instability of a viscous hollow jet. *Phys. Rev. E* **75** (2), 027301.
- GAÑÁN-CALVO, A. M. & GORDILLO, J. M. 2001 Perfectly monodisperse microbubbling by capillary flow focusing. *Phys. Rev. Lett.* **87** (27), 274501.
- GARNIER, N., GRIGORIEV, R. O. & SCHATZ, M. F. 2003 Optical manipulation of microscale fluid flow. *Phys. Rev. Lett.* **91** (5), 054501.
- GARSTECKI, P., FUERSTMAN, M. J., STONE, H. A. & WHITESIDES, G. M. 2006 Formation of droplets and bubbles in a microfluidic T-junction—scaling and mechanism of break-up. *Lab Chip* **6**, 437–446.
- GARSTECKI, P., FUERSTMAN, M. J. & WHITESIDES, G. M. 2005a Nonlinear dynamics of a flow-focusing bubble generator: An inverted dripping faucet. *Phys. Rev. Lett.* **94**, 234502.
- GARSTECKI, P., GAÑÁN-CALVO, A. M. & WHITESIDES, G. M. 2005b Formation of bubbles and droplets in microfluidic systems. *Bull. Pol. Ac.: Tech* **53** (4), 361–372.
- GARSTECKI, P., GITLIN, I., DILUZIO, W., WHITESIDES, G. M., KUMACHEVA, E. & STONE, H. A. 2004 Formation of monodisperse bubbles in a microfluidic flow-focusing device. *Appl. Phys. Lett.* **85** (13), 2649–2651.
- GARSTECKI, P., STONE, H. A. & WHITESIDES, G. M. 2005c Mechanism for flow-rate controlled breakup in confined geometries: A route to monodisperse emulsions. *Phys. Rev. Lett.* **94** (16), 164501.
- GAST, A. 1997 *Physical chemistry of surfaces*. Wiley.
- GIGLIO, M. & VENDRAMINI, A. 1977 Soret-type motion of macromolecules in solution. *Phys. Rev. Lett.* **38**, 26–30.

- GLASGOW, I, BATTON, J. & AUBRY, N. 2004 Electroosmotic mixing in microchannels. *Lab Chip* **4**, 558–562.
- GORDON, J. P., LEITE, R. C. C., MOORE, R. S., PORTO, S. P. S. & WHINNERY, J. R. 1965 Long-transient effects in lasers with inserted liquid samples. *J. App. Phys.* **36** (1), 3–8.
- GRIGORIEV, R. O. 2005 Chaotic mixing in thermocapillary-driven microdroplets. *Phys. Fluids* **17** (3), 033601.
- GRIGORIEV, R. O., SCHATZ, M F. & SHARMA, V. 2006 Chaotic mixing in microdroplets. *Lab Chip* **6**, 1369–1372.
- GUGLIOTTI, M., BAPTISTA, M. S. & POLITI, M. J. 2002 Laser-induced Marangoni convection in the presence of surfactant monolayers. *Langmuir* **18**, 9792–9798.
- GUILLOT, P., COLIN, A. & AJDARI, A. 2008 Stability of a jet in confined pressure-driven biphasic flows at low Reynolds number in various geometries. *Phys. Rev. E* **78**, 016307.
- GUILLOT, P., COLIN, A., UTADA, A. S. & AJDARI, A. 2007 Stability of a jet in confined pressure-driven biphasic flows at low Reynolds numbers. *Phys. Rev. Lett.* **99**, 204502.
- GÜNTHER, A. & JENSEN, K. F. 2006 Multiphase microfluidics: From flow characteristics to chemical and materials synthesis. *Lab Chip* **6**, 1487–1503.
- HARRISON, D. J., MANZ, A., FAN, Z., LÜDI, H & WIDMER, H. M. 1992 Capillary electrophoresis and sample injection systems integrated on a planar glass chip. *Anal. Chem.* **64**, 1926–1932.
- HE, M., KUO, J. S. & CHIU, D. T. 2005 Electro-generation of single femtoliter- and picoliter-volume aqueous droplets in microfluidic systems. *Appl. Phys. Lett.* **87**, 031916.
- HERRADA, M. A., GAÑÁN-CALVO, A. M. & GUILLOT, P. 2008 Spatiotemporal instability of a confined capillary jet. *Phys. Rev. E* **78**, 046312.
- HUEBNER, A., SRISA-ART, M., HOLT, D., ABELL, C., HOLLFELDER, F., DE MELLO, A. J. & EDEL, J. B. 2007 Quantitative detection of protein expression in single cells using droplet microfluidics. *Chem. Comm.* **12**, 1218–1220.
- HUERRE, P. & MONKEWITZ, P. A. 1990 Local and global instabilities in spatially developing flows. *Ann. Rev. Fluid Mech.* **22**, 473–537.

- INCROPERA, F. P. & DE WITT, D. P. 1985 *Fundamentals of Heat and Mass Transfer*, 2nd edn. John Wiley & Sons.
- JIAO, Z., HUANG, X., NGUYEN, N. T. & ABGRALL, P. 2008 Thermocapillary actuation of droplet in a planar microchannel. *Microfluid. Nanofluid.* **5**, 205–214.
- JOHNER, A. & JOANNY, J. F. 1990 Block copolymer adsorption in a selective solvent - a kinetic-study. *Macromolecules* **23**, 5299–5311.
- JOUSSE, F., FARR, R., LINK, D. R., FUERSTMAN, M. J. & GARSTECKI, P. 2006 Bifurcation of droplet flows within capillaries. *Phys. Rev. E* **74**, 036311.
- JOUSSE, F., LIAN, G., JANES, R. & MELROSE, J. 2005 Compact model for multi-phase liquid-liquid flows in micro-fluidic devices. *Lab Chip* **5**, 646–656.
- KARSTENS, T. & KOBBS, K. 1980 Rhodamine B and Rhodamine 101 as reference substances for fluorescence quantum yield measurements. *J. Phys. Chem.* **84** (14), 1871–1872.
- LABROT, V., SCHINDLER, M., GUILLOT, P., COLIN, A. & JOANICOT, M. 2009 Extracting the hydrodynamic resistance of droplets from their behavior in microchannel networks. *Biomicrofluidics* **3** (1), 012804.
- LAJEUNESSE, E. & HOMSY, G. M. 2003 Thermocapillary migration of long bubbles in polygonal tubes. ii. experiments. *Phys. Fluids* **15**, 308–314.
- LAVAL, P., LISAI, N., SALMON, J. B. & JOANICOT, M. 2007 A microfluidic device based on droplet storage for screening solubility diagrams. *Lab Chip* **7** (7), 829–834.
- LEIB, S J & GOLDSTEIN, M E 1986 Convective and absolute instability of a viscous liquid jet. *Phys. Fluids* **29** (4), 952–954.
- LEVICH, V. G. 1962 *Physicochemical hydrodynamics*. N. J.: Prentice Hall, Englewoof Clifs.
- LEVICH, V. G. & KRYLOV, V. S. 1969 Surface tension-driven phenomena. *Annu. Rev. Fluid Mech.* **1**, 293–316.
- LIAU, A., KARNIK, R., MAJUMDAR, A. & CATE, J. H. D. 2005 Mixing crowded biological solutions in milliseconds. *Anal. Chem.* **77** (23), 7618–7625.
- LIDE, DAVID R., ed. 2003 *CRC Handbook of chemistry and physics*. CRC Press LLC.

- LIN, S. P. & LIAN, Z. W. 1992 Absolute and convective instability of a viscous liquid jet surrounded by a viscous gas in a vertical pipe. *Phys. Fluids A* **5** (3), 771–773.
- LINK, D. R., GRASLAND-MONGRAIN, E., DURI, A., SARRAZIN, F., CHENG, Z., CRISTOBAL, G., MARQUEZ, M. & WEITZ, D. A. 2006 Electric control of droplets in microfluidic devices. *Angew. Chem. Int. Ed.* **45**, 2556–2560.
- LIU, Y., CHENG, D. K., SONEK, G. J., BERNS, M. W., CHAPMAN, C. F. & TROMBERG, B. J. 1995 Evidence for localized cell heating induced by infrared optical tweezers. *Biophys. J.* **68** (5), 2137–2144.
- LORENZ, R. M., EDGAR, J. S., JEFFRIES, G. D. M., ZHAO, Y. Q., MCGLOIN, D. & CHIU, D. T. 2007 Vortex-trap-induced fusion of femtoliter-volume aqueous droplets. *Anal. Chem.* **79** (1), 224–228.
- LUO, D., PULLELA, S. R., MÁRQUEZ, M. & CHENG, Z. 2007 Cell capsules with tunable transport and mechanical properties. *Biomicrofluidics* **1** (3), 034102.
- MAO, H., ARIAS-GONZÁLEZ, J. R., SMITH, S. B., TINOCO, I. JR. & BUSTAMANTE, C. 2005 Temperature control methods in a laser tweezers system. *Biophys. J.* **89** (2), 1308–1316.
- MARCANO, A. & URDANETA, O. 2001 Fluorescence quantum yield of Rhodamine 101 in the presence of absorption saturation. *Appl. Phys. B* **72**, 207–213.
- MAZOUCHI, A. & HOMSY, G. M. 2000 Thermocapillary migration of long bubbles in cylindrical capillary tubes. *Phys. Fluids* **12** (3), 542–549.
- MCDONALD, J. C., DUFFY, D. C., SANDERSON, J. R., CHIU, D. T., WU, H., SCHUELLER, O. J. A. & WHITESIDES, G. M. 2000 Fabrication of microfluidic systems in poly(dimethylsiloxane). *Electrophoresis* **21**, 27–40.
- MCGLOIN, D. 2006 Optical tweezers: 20 years on. *Phil. Trans. Roy. Soc. A* **364** (1849), 3521–3537.
- VAN DE MEENT, J. W., TUVAL, I. & GOLDSTEIN, R. E. 2008 Microfluidic transporter: rotational cytoplasmic streaming at high Péclet numbers. *Phys. Rev. Lett.* **101**, 178102.
- MING, L. C. & BASSETT, W. A. 1974 Laser heating in the diamond anvil press up to 2000°C sustained and 3000°C pulsed at pressures up to 260 kilobars. *Rev. Sci. Instrum.* **45** (9), 1115–1118.

- NIU, X., GULATI, S., EDEL, J. B. & DE MELLO, A. J. 2008 Pillar induced droplet merging in microfluidic circuits. *Lab Chip* **8**, 1837.
- NIU, XIZE, ZHANG, MENG Ying, PENG, SUILI, WEN, WEIJIA & SHENG, PING 2007 Real-time detection, control, and sorting of microfluidic droplets. *Biomicrofluidics* **1** (4), 044101.
- OKKELS, F. & TABELING, P. 2004 Spatiotemporal resonances in mixing of open viscous fluids. *Phys. Rev. Lett.* **92** (3), 038301.
- OTTINO, J. M. 1989 *The Kinematics of Mixing: Stretching, Chaos, and Transport*. Cambridge University Press.
- PELTONEN, L. & YLIRUUSI, J. 2000 Surface pressure, hysteresis, interfacial tension, and CMC of four sorbitan monoesters at water-air, water-hexane, and hexane-air interfaces. *J. Coll. Int. Sci.* **227**, 1–6.
- PETERMAN, E. J. G., GITTES, F. & SCHMIDT, C. F. 2003 Laser-induced heating in optical traps. *Biophys. J.* **84** (2), 1308–1316.
- PICKARD, W. F. 2003 The role of cytoplasmic streaming in symplastic transport. *Plant, Cell and Environment* **26**, 1–5.
- PLATEAU, J. 1873 *Statique experimentale et theorique des liquides soumis aux seules forces moleculaires*. Gauthier-Vilars.
- POUJADE, M., GRASLAND-MONGRAIN, E., HERTZOG, A., JOUANNEAU, J., CHAVRIER, P., LADOUX, B., BUGUIN, A. & SILBERZAN, P. 2007 Collective migration of an epithelial monolayer in response to a model wound. *PNAS* **104** (41), 15988–15993.
- PRAKASH, M. & GERSHENFELD, N. 2007 Microfluidic bubble logic. *Science* **315**, 832.
- PRIEST, C., HERMINGHAUS, S. & SEEMANN, R. 2006 Controlled electrocoalescence in microfluidics: Targeting a single lamella. *Appl. Phys. Lett.* **89**, 134101.
- PURCELL, E. M. 1997 Life at low Reynolds number. *Am. J. Physics* **45** (1), 3–11.
- RAUCH, J. & KOHLER, W. 2002 Diffusion and thermal diffusion of semidilute to concentrated solutions of polystyrene in toluene in the vicinity of the glass transition. *Phys. Rev. Lett.* **88** (18), 185901.

- RAYLEIGH, LORD 1879 On the stability, or instability, of certain fluid motion. *Proc. Lond. Math. Soc.* **10**, 4.
- REINHARDT, H., DITTRICH, P. S., MANZ, A. & FRANZKE, J. 2007 μ -Hotplate enhanced optical heating by infrared light for single cell treatment. *Lab Chip* **7**, 1509–1514.
- ROSS, D., GAITAN, M. & LOCASCIO, L.E. 2001 Temperature measurement in microfluidic systems using a temperature-dependent fluorescent dye. *Anal. Chem.* **73** (17), 4117–4123.
- RUSCONI, R., ISA, L. & PIAZZA, R. 2004 Thermal-lensing measurement of particle thermophoresis in aqueous dispersions. *J. Opt. Soc. Am. B* **21** (3), 605–616.
- DE SAINT VINCENT, M. R., WUNENBURGER, R. & DELVILLE, J. P. 2008 Laser switching and sorting for high speed digital microfluidics. *Appl. Phys. Lett.* **92** (15), 154105.
- SAKAKIBARA, J., HISHIDA, K. & MAEDA, M. 1997 Vortex structure and heat transfer in the stagnation region of an impinging plane jet (simultaneous measurements of velocity and temperature fields by digital particle image velocimetry and laser-induced fluorescence). *Int. J. Heat Mass Transfer.* **40** (13), 3163–3176.
- SAMMARCO, T. S. & BURNS, M. A. 1999 Thermocapillary pumping of discrete drops in microfabricated analysis devices. *AIChE J.* **45** (2), 350–366.
- SCHATZ, M. F. & NEITZEL, G. P. 2001 Experiments on thermocapillary instabilities. *Annu. Rev. Fluid Mech.* **33**, 93–127.
- SCHINDLER, M. & ADJARI, A. 2008 Droplet traffic in microfluidic networks: A simple model for understanding and designing. *Phys. Rev. Lett.* **100**, 044501.
- SOIFER, V. A., KOTLYAR, V. & DOSKOLOVICH, L. 1997 *Iterative Methods for Diffractive Optical Elements Computation*. Taylor & Francis, London.
- SOLOMON, T. H. & GOLLUB, J. P. 1988 Chaotic particle transport in time-dependent Rayleigh-Bénard convection. *Phys. Rev. A* **38** (12), 6280–6286.
- SONG, H., CHEN, D. L. & ISMAGILOV, R. F. 2006 Reactions in droplets in microfluidic channels. *Angew. Chemie. Int. Ed.* **45**, 7336–7356.
- SONG, H., TICE, J. D. & ISMAGILOV, R. F. 2003 A microfluidic system for controlling reaction networks in time. *Angew. Chem. Int. Ed.* **42** (7), 767–771.

- SRITHARAN, K., STROBL, C. J., SCHNEIDER, M. F., WIXFORTH, A. & GUTTENBERG, Z. 2006 Acoustic mixing at low Reynolds numbers. *Appl. Phys. Lett.* **88**, 054102.
- STONE, H. A., STROOCK, A. D. & ADJARI, A. 2004 Engineering flow in small devices: Microfluidics towards a lab-on-a-chip. *Annu. Rev. Fluid Mech.* **36**, 381–411.
- STONE, Z. B. & STONE, H. A. 2005 Imaging and quantifying mixing in a model droplet micromixer. *Phys. Fluids* **17**, 063103.
- STROOCK, A. D., DERTINGER, S. K. W., ADJARI, A., MEZIĆ, I., STONE, H. A. & WHITESIDES, G. M. 2002 Chaotic mixer for microchannels. *Science* **295**, 647–651.
- SUBRAMANIAM, K. & PARTHASARATHY, R. N. 2000 Effects of confinement on the temporal instability of gas jets injected in viscous liquids. *Phys. Fluids* **12** (1), 89–91.
- SUMINO, Y., MAGOME, N., HAMADA, T. & YOSHIKAWA, K. 2005 Self-running droplet: Emergence of regular motion from nonequilibrium noise. *Phys. Rev. Lett.* **94**, 068301.
- TABELING, P. 2003 *Introduction à la Microfluidique*. Editions Belin.
- TAN, Y. C., FISHER, J. S., LEE, A. I., CRISTINI, V. & LEE, A. P. 2004 Design of microfluidic channel geometries for the control of droplet volume, chemical concentration, and sorting. *Lab Chip* **4**, 292–298.
- TEH, S. Y., LIN, R., HUNG, L. H. & LEE, A. P. 2008 Droplet microfluidics. *Lab Chip* **8**, 198–220.
- THORSEN, T., ROBERTS, R. W., ARNOLD, F. H. & QUAKE, S. R. 2001 Dynamic pattern formation in a vesicle-generating microfluidic device. *Phys. Rev. Lett.* **86** (18), 4163–4166.
- TOMOTIKA, S. 1935 On the instability of a cylindrical thread of a viscous liquid surrounded by another viscous fluid. *Proc. R. Soc. Lond. A* **150**, 322–337.
- UTADA, A. S., FERNÁNDEZ-NIEVES, A., STONE, H. A. & WEITZ, D. A. 2007 Dripping to jetting transitions in coflowing liquid streams. *Phys. Rev. Lett.* **99** (9), 094502.
- VAINCHTEIN, D. L., WIDLOSKI, J. & GRIGORIEV, R. 2007 Mixing properties of steady flow in thermocapillary driven droplets. *Phys. Fluids* **19** (6), 067102.

- VANAPALLI, S. A., BANPURKAR, A. G., VAN DEN ENDE, D., DUIJS, M. H. G. & MUGELE, F. 2009 Hydrodynamic resistance of single confined moving drops in rectangular microchannels. *Lab Chip* **9**, 982–990.
- VIGOLO, D., BRAMBILLA, G. & PIAZZA, R. 2007 Thermophoresis of microemulsion droplets: Size dependence of the Soret effect. *Phys. Rev. E* **75**, 040401.
- VOTH, G. A., HALLER, G. & GOLLUB, J. P. 2002 Experimental measurements of stretching fields in fluid mixing. *Phys. Rev. Lett.* **88** (25), 254501.
- WARD, T. & HOMSY, G. M. 2001 Electrohydrodynamically driven chaotic mixing in a translating drop. *Phys. Fluids* **13** (12), 3521–3525.
- WONG, H., RADKE, C. J. & MORRIS, S. 2006 The motion of long bubbles in polygonal capillaries. Part 1. Thin films. *J. Fluid Mech.* **292**, 71–94.
- XIA, Y. & WHITESIDES, G. M. 1998 Soft lithography. *Angew. Chem. Int. Ed.* **37**, 550–575.
- XU, J. & ATTINGER, D. 2008 Drop on demand in a microfluidic chip. *J. Micromech. Microeng.* **18**, 065020.
- YOUNG, N. O., GOLDSTEIN, J. S. & BLOCK, M. J. 1959 The motion of bubbles in a vertical temperature gradient. *J. Fluid Mech.* **6** (3), 350–356.
- ZONDERVAN, R., KULZER, F., VAN DER MEER, H., DISSELHORST, J. A. J. M. & ORRIT, M. 2006 Laser-driven microsecond temperature cycles analyzed by fluorescence polarization microscopy. *Biophys. J.* **90** (8), 2958–2969.